



DOCTORAL SCHOOL
MEDITERRANEA UNIVERSITY OF REGGIO CALABRIA

DEPARTMENT OF INFORMATION ENGINEERING, INFRASTRUCTURES AND SUSTAINABLE
ENERGY (DIIES)

PHD IN
INFORMATION ENGINEERING

S.S.D. ING-INF/01
XXVII CYCLE

AUTONOMOUS AND ENERGY EFFICIENT WIRELESS SENSOR PLATFORMS

CANDIDATE
Corrado FELINI

ADVISOR
Prof. Francesco G. DELLA CORTE

COORDINATOR
Prof. Claudio DE CAPUA

REGGIO CALABRIA, FEBRUARY 2015

Finito di stampare nel mese di **Febbraio 2015**

Edizione  Centro
Stampa
d'Ateneo

Collana *Quaderni del Dottorato di Ricerca in Ingegneria dell'Informazione*
Curatore *Prof. Claudio De Capua*

Università degli Studi *Mediterranea* di Reggio Calabria
Salita Melissari, Feo di Vito, Reggio Calabria

CORRADO FELINI

**AUTONOMOUS AND ENERGY EFFICIENT WIRELESS
SENSOR PLATFORMS**

The Teaching Staff of the PhD course in
INFORMATION ENGINEERING
consists of:

Claudio DE CAPUA (coordinator)
Raffaele ALBANESE
Francesco BUCCAFURRI
Salvatore COCO
Francesco DELLA CORTE
Domenico GATTUSO
Giovanna IDONE
Antonio IERA
Tommaso ISERNIA
Andrea MORABITO
Lorenzo CROCCO
Giovanni LEONE
Massimiliano MATTEI
Roberta NIPOTI
Carlo MORABITO
Francesco RUSSO
Riccardo CAROTENUTO
Antonella MOLINARO
Maria Nadia POSTORINO
Francesco RICCIARDELLI
Domenico URSINO
Mario VERSACI
Giovanni ANGIULLI
Giuseppe ARANITI
Giacomo CAPIZZI
Rosario CARBONE
Mariantonia COTRONEI
Sofia GIUFFRÈ
Fabio LA FORESTA
Valerio SCORDAMAGLIA
Gianluca LAX
Fortunato PEZZIMENTI
Giuseppe MUSOLINO
Domenico ROSACI
Giuseppe RUGGERI
Giuseppe SARNÈ
Ivo RENDINA
Lubomir DOBOS

This work was supported by GELMINCAL project
PON 2007/2013: PONa3_00308

To Francesca and my Family

Contents

Contents	I
List of Figure	IV
List of Table	VIII
Introduction	1
1 Radio Frequency technologies for wireless sensor applications	5
1.1 Introduction	5
1.2 Radio Frequency Characteristics	6
1.3 Wireless Sensors	8
1.3.1 Applications	10
1.3.2 System evaluation metrics	13
1.4 Energy Harvesting	16
1.4.1 RF Energy Harvesting	18
1.5 Proposed Solution	21
2 UHF-RFID Sensor Platform	23
2.1 Introduction	23
2.2 UHF-RFID Sensor Platform Architecture	24
2.3 Rectenna	29
2.3.1 Antenna	29
2.3.2 Rectifier	32
2.4 Impedance Matching in RF Platform	34
2.4.1 Modified Friis's Equation	35
2.4.2 Impedance Matching Network	36
2.5 Energy Harvesting Performance	38
2.5.1 Antenna evaluation	38
2.5.2 Choice of diodes	41

2.5.3	Two stage Dickson Rectifier	42
2.5.4	Five stage Dickson Rectifier.....	44
2.6	Dynamic Impedance Matching.....	46
2.6.1	Conceptual approach	47
2.6.2	Algorithm.....	47
2.6.3	Measurements.....	49
2.7	Power Management and Digital Section	50
2.7.1	Voltage Regulator	50
2.7.2	Microcontroller	51
2.7.3	RFID Front End.....	52
2.8	Platform Performance Evaluation.....	52
2.8.1	Dynamic Impedance Matching Evaluation.....	53
2.8.2	Power Budget.....	54
2.9	Applications	55
2.9.1	Wireless temperature sensor.....	55
2.9.2	Performance for Long-run Sensing Applications and Wireless Sensors Networks.....	56
2.9.3	13.56MHz Platform.....	61
2.10	Remarks.....	66
3	CMOS Wireless Sensors ICs.....	67
3.1	Introduction.....	67
3.2	HCPV Monitoring.....	68
3.2.1	System architecture.....	69
3.3	Integrated sensors	70
3.3.1	Integrated Temperature Sensor	72
3.3.2	Integrated light sensor.....	75
3.3.3	Analog Front End.....	79
3.4	AMS CMOS 0.35 μ m Analog Sensors.....	82
3.4.1	AMS CMOS 0.35 μ m Temperature Sensor	83
3.4.2	AMS CMOS 0.35 μ m Light Sensor.....	87
3.5	Digital Section	89
3.5.1	Analog-to-digital conversion.....	89
3.5.2	Parallel Input Serial Output.....	90

3.5.3 Load generation.....	90
3.6 RF Section.....	91
3.6.1 LC Cross-Coupled Oscillator design	91
3.6.2 Power Amplifier.....	95
3.6.3 Power On.....	95
3.6.4 On Chip Dipole Antenna	96
3.7 Experimental results	100
3.7.1 Temperature Sensor.....	100
3.7.2 Light sensor.....	103
3.7.3 RF Transmitter performance	106
3.7.4 Code Transmission Measurements.....	108
3.7.5 Analysis of whole system	109
3.8 Remarks.....	110
Conclusions	112
Conclusions	112
Future works.....	114
Acknowledgements	115
References.....	116

List of Figure

Fig. 1.1 Block Diagram for wireless sensor node.....	8
Fig. 1.2 Example of a Body Area Network.....	11
Fig. 1.3 Typical application in industrial scenario.....	12
Fig. 1.4 Block diagram of a CMOS RFID tag for environmental monitoring	13
Fig. 1.5 Wearable Thermoelectric Energy Harvesting used for measurements of thermal properties of humans and power generation on people at different ambient conditions.....	17
Fig. 1.6 RF to DC converter.....	19
Fig. 1.7 Printed monopole solar antenna.....	19
Fig. 2.1 General block diagram of an energy-harvesting-enabled wireless sensor platform system.....	25
Fig. 2.2 Schematic diagram of α -Wisp battery-free one bit accelerometer (left); photograph of α -Wisp (right).....	25
Fig. 2.3 Wisp Platform.....	26
Fig. 2.4 Simplified scheme of the designed RFID S-tag	26
Fig. 2.5 RAMSES Platform.....	28
Fig. 2.6 Block diagram of the proposed RFID sensors platform.....	28
Fig. 2.7 Generic block diagram of a rectenna.....	29
Fig. 2.8 Antenna Field Regions.....	30
Fig. 2.9 Formation and detachment of electric field lines for a dipole.....	31
Fig. 2.10 Schematic of a conventional Dickson multi-stage rectifier.....	32
Fig. 2.11 Voltage Doubler.....	33
Fig. 2.12 Clamper Effect.....	34
Fig. 2.13 Impedance Matching Network.....	36
Fig. 2.14 Configurations of dual lumped elements matching network.....	37
Fig. 2.15 Monopole Meander.....	39
Fig. 2.16 Miniaturized antenna.....	39

Fig. 2.17 (a) $\lambda/2$ Dipole antenna; (b) Monopole meander antenna; (c) Miniaturized antenna.....	40
Fig. 2.18 Evaluation of antenna performances, considering the output voltage of a rectifier connected to the antenna's output.....	40
Fig. 2.19 Input power to rectifier, connected at dipole antenna, estimated through a dedicated power detector.....	41
Fig. 2.20 Output voltage of dual the stage Dickson rectifier Vs Input power with $1\text{M}\Omega$ (a), $100\text{k}\Omega$ (b), $10\text{k}\Omega$ (c) and $1\text{k}\Omega$ (d) RL	43
Fig. 2.21 Output voltage of the five stage Dickson rectifier Vs Input power..	45
Fig. 2.22 Efficiency of the five stage Dickson rectifier Vs Input power.....	45
Fig. 2.23 Conceptual approach for dynamic impedance matching.....	47
Fig. 2.24 Rectifier output voltage Vs Input power.....	48
Fig. 2.25: Input power Vs Rectifier output voltage. The experimental data is compared with the fitting curve.....	48
Fig. 2.26 Experimental prototype.....	49
Fig. 2.27 Real and Imaginary part of input impedance of the RF energy harvesting circuit at 868MHz.....	50
Fig. 2.28 A snapshot of the prototype connected with a SMA connector.....	53
Fig. 2.29 Energy harvesting efficiency of the realized prototype Vs Input Power. The dynamic matching strategy adopted in this study is compared to the static matching and to no matching options, tested on the same circuit.....	54
Fig. 2.30 A snapshot of the prototype connected with dipole antenna.....	55
Fig. 2.31 24-hour temperature monitoring performed in an indoor environment.....	56
Fig. 2.32 A sample scenario of the network model.....	59
Fig. 2.33 Harvested power varying the distance between the reader's antenna and the tag.....	59
Fig. 2.34 Number of required readers.....	61
Fig. 2.35 Picture of the 13.56 MHz platform prototype.....	62
Fig. 2.36 Square coil antenna.....	63
Fig. 2.37 Impedance of the smallest antenna on the PCB board.....	64

Fig. 2.38 Impedance of the smallest antenna on the PCB board with matching capacitor..... 64

Fig. 2.39 Impedance of the biggest antenna on the PCB board..... 65

Fig. 2.40 Impedance of the biggest antenna on the PCB board with matching capacitor..... 65

Fig. 3.1 Wireless HCPV sensor architecture..... 70

Fig. 3.2 Current driven diode..... 72

Fig. 3.3 Scheme of absolute temperature sensor with matched diode..... 74

Fig. 3.4 BJT biased a different current75

Fig. 3.5 Relationship between absorption length and wavelengths..... 76

Fig. 3.6 Cross section of photodiode..... 77

Fig. 3.7 Differential pair Amplifier..... 79

Fig. 3.8 Differential pair drain currents versus differential input voltage..... 80

Fig. 3.9 CMOS differential amplifier with PMOS active load..... 81

Fig. 3.10 Transimpedance amplifier configuration..... 81

Fig. 3.11 Wafer section for AMS 0.35 μ m CMOS Technology..... 82

Fig. 3.12 PTAT with MOS mirror current..... 83

Fig. 3.13 Emitter voltage of transistors Q1 and Q2 at various temperature... 85

Fig. 3.14 Differential output of the PTAT in a temperature range from 0 to 100°C..... 85

Fig. 3.15 Architecture of the integrated PTAT with differential amplifier..... 86

Fig. 3.16 Simulated characteristic of the PTAT Vs temperature..... 87

Fig. 3.17 Structure of realized micro solar cell (top view)..... 88

Fig. 3.18 Simulated Characteristic of the Transimpedance Amplifier vs photocurrent..... 88

Fig. 3.19 Block diagram of Digital Section..... 89

Fig. 3.20 Timing diagram of the start signal generation..... 91

Fig. 3.21 Block diagram of the LC cross coupled transmitter topology..... 91

Fig. 3.22 Schematic of the ‘cross-coupled’ LC MOS oscillator..... 92

Fig. 3.23 LC Equivalent circuit..... 92

Fig. 3.24 LC cross-coupled oscillator with CMOS technology..... 94

Fig. 3.25 Inverter-based differential amplifier configuration..... 95

Fig. 3.26 Structures dipole antennas: (a) linear, (b) zigzag, (c) meander, (d) loop AMS CMOS Transmitter	96
Fig. 3.27 Simulated frequency carrier of the designed LC oscillator.....	98
Fig. 3.28 Start-up time transient of the designed LC oscillator.....	98
Fig. 3.29 Circuit schematic of the implemented transmitter.....	99
Fig. 3.30 On chip Dipole Cross Section.....	99
Fig. 3.31 Microphotograph of the realized chip.....	100
Fig. 3.32 Experimental setup used to characterize the PTAT performances	100
Fig. 3.33 Characteristic of the PTAT sensor.....	101
Fig. 3.34 Characteristic of PTAT sensor Vs Supply voltage variations.....	102
Fig. 3.35 Characteristic of PTAT in both directions of operation.....	102
Fig. 3.36 Characteristic of the irradiation sensor under the sun.....	103
Fig. 3.37 Characteristic of the Transimpedance Amplifier output Vs photocurrent.....	104
Fig. 3.38 Characteristic of the Transimpedance Amplifier output Vs photocurrent at various temperatures.....	105
Fig. 3.39 Characteristic of the Transimpedance Amplifier output Vs photocurrent generated by the micro solar cell.....	105
Fig. 3.40 Carrier Frequency of the transmitter.....	106
Fig. 3.41 Phase noise of the proposed transmitter.....	107
Fig. 3.42 Figure Of Merit of the proposed transmitter.....	108
Fig. 3.43 Digital Code and demodulated signal as recorded at the audio output of the radio receiver.....	109
Fig. 3.44 Serialized output of 32-bit PISO.....	109
Fig. 3.45 Digital Code and demodulated signal of recorded at the audio output of the receiver. The data correspond at the light sensor and the PTAT.....	110

List of Table

Table 1.1 Characteristic of battery.....	10
Table 1.2 Power Density of Energy Harvesting source.....	16
Table 1.3 ISM frequency bands.....	21
Table 2.1 Synthesizing Reactance (X) and Susceptance (B) using lumped elements.....	38
Table 2.2 Measured efficiency of the dual stage Dickson rectifier.....	44
Table 2.3 Simulated efficiency of the dual stage Dickson rectifier.....	44
Table 2.4 Sensor platform power consumption under the three operation states.....	55
Table 2.5 Main parameters used in simulation.....	60
Table 3.1 Dimensions of current mirror transistors.....	84
Table 3.2 Transistor dimensions of differential amplifier.....	86
Table 3.3 Code Table.....	90
Table 3.4 Transistor dimensions of differential cross coupled LC oscillator	97
Table 3.5: Performance summary of proposed LC Oscillator.....	107
Table 3.6 Summary between expected value and experimental results.....	110

Introduction

In recent time, wireless technologies have been rapidly developing, paving the way to the spreading of mobile technologies. Indeed, several wireless applications grew up for short-range, point-to-point communications, long-distance cellular phone systems and internet applications.

Moreover, the peculiarity of wireless systems for contactless communications over distance has allowed the development of emerging applications, such as wireless sensor in order to monitor several physical parameters in applications where electro-mechanical systems must interact with the environment. These devices are typically low-cost, low-power and tiny devices, equipped with limited sensing, data processing and wireless communication capabilities, as well as power supply elements.

A far greater potential exists for the development and application of wireless sensors, starting from military or environmental monitoring, moving towards machine-to-machine communications (M2M), and eventually reaching all aspects of our lives.

Wireless sensors allow otherwise impossible sensor applications, such as monitoring dangerous, hazardous, unwired or remote areas and locations. This technology provides nearly unlimited installation flexibility for sensors and increased network robustness. Furthermore, wireless technology reduces maintenance complexity and costs.

The link with the RFID technology can be a practical and low-cost solution to associate Radio Frequency Identification, for tracking of products,

animals, or persons, with a dynamic variable data acquisition from on-board sensors, in order to realize a simple and compact wireless sensor device.

The first solution proposed in this study deals with the development of a wireless sensor platform in RFID technology supervised by a microcontroller (MCU). This approach brings many advantages, in particular the possibility to use the signal transmitted by the RFID reader for harvesting enough energy to make the system battery-less.

This platform, that can be remotely activated and powered, paves the way to a wide range of sensing and monitoring applications. RF fields can be generated on demand, thus providing a more stable and convenient power supply for harvesting system, despite the lower efficiency with respect to sunlight, thermal gradients, mechanical, convection flows or other forms of harvestable energy. Within this scenario, the need for standard battery replacement or maintenance is eliminated.

RF devices that act as sensing nodes can be mounted in positions that are difficult to be accessed by humans, or even embedded within the structure to be monitored during its construction or during the lifetime of artifacts subject to modification of their structure (structural monitoring). The usage of backscattering modulation methods enables the data transmission to be implemented using the same fields that power the nodes.

A simple way to maximize the use of wireless sensors is to reduce the dimensions of transducers and the need of power supply, moving to integrated systems that comprise transducers, logic circuits, an RF oscillator and a radiating element.

Compared to traditional sensors, integrated sensors have the advantage that signal conditioning and interface electronics can be integrated on the same chip. Furthermore, integrating traditional sensors into a chip requires extra fabrication steps and materials, while an integrated sensor can be made in a standard high volume IC process, so production costs can be minimized. In contrast to the classic wired configuration, a wireless communication channel might pave the way to new unexplored applications: the output signal can be transmitted using an antenna realized directly on chip, eliminating the

need for external transmission line connections and sophisticated packaging, which can radically reduce the cost of IC systems.

Exploiting this technology, the nodes can have sizes of the order of mm³ and be sufficiently inexpensive. Rapid scaling of low cost CMOS technology has enabled circuits and systems to operate into the micro/millimeter wave frequency band, where the required antenna size shrinks and makes the implementation of an on-chip antenna feasible. Thus the on-chip antenna concept is the actual trend in integrated wireless sensor systems because it could be a practical solution to obtain compact, small size and low cost devices for short-range wireless applications.

This thesis is organized in 3 chapters.

Chapter 1 introduces the RF technologies for wireless sensor applications, with a short review of its working principles. Particular attention is addressed at the energy harvesting systems to realize battery-less sensor platforms; finally, RF energy harvesting techniques are discussed.

Chapter 2 describes the RFID wireless sensor platform made with discrete components, that allows to reuse simple and affordable communication protocols and reader systems to acquire sensors data from a macroscopic system. The platform uses an energy harvesting system to supply itself through the RF signal transmitted by a standard reader. In addition the design, implementation and experimental characterization phases, are described. Finally, several applications are presented.

Chapter 3 outlines the wireless sensor in 0.35 μ m CMOS technology, specifically designed for the monitoring of High Concentration PhotoVoltaics (HCPV) modules. This microchip uses a LC cross-coupled oscillator as RF carrier generator working at frequency of 2.5 GHz, a temperature sensor and a light sensor as transducers. In addition the design, implementation and experimental characterization phases are described.

Conclusions summarize the thesis and conclude with a prediction of future related improvements.

1 Radio Frequency technologies for wireless sensor applications

Nowadays, Radio Frequency technologies are key aspects to many electronics fields. RF signals are used as carrier in many systems, as cellular and other wireless technologies including Wi-Fi, WiMAX, NFC, RFID. This chapter introduces the RF technologies for wireless sensor applications, with a short review of its working principles. Particularly attention is addressed at the energy harvesting systems to realize battery-less sensor platforms; finally RF energy harvesting technics are discussed.

1.1 Introduction

Wireless technologies have been growing at an explosive rate over the last few years and have had a significant impact on the information technology industry.

The variety of wireless technologies being developed range from simple IrDA that uses infrared light for short-range, point-to-point communications, to wireless personal area network (WPAN), point-to multi-point communications, such as Bluetooth and ZigBee, to mid-range, multi-hop wireless local area network (WLAN), to long-distance cellular phone systems, such as GSM/GPRS and CDMA . Nowadays, the majority of people are

aware of the strong impact that these wireless technology products have had mainly due to the astonishing growth of cell-phone market.

High frequency applications and better reliability of wireless connections are now possible, thanks to the progress of semiconductor technologies and accelerated wireless product development. The products achieved higher levels of efficiency because there is a continued miniaturization of circuitry, displays, user interfaces, the “building blocks” of portable devices, along with advances in low-power electronics and battery (life, weight). For this reason, affordable application solutions are the key ingredient in the rapid acceptance of wireless technologies[1].

Conversely, few people have realized that the demand of bandwidth for wireless, interpersonal communications, such as cellular phones, will soon become a minority share of the total available bandwidth. A far greater potential exists for development and applications of other types of wireless technologies, especially wireless sensors and sensor networks, starting from military and environmental monitoring, moving towards machine-to-machine communications (M2M), and eventually reaching all aspects of our lives.

Wireless sensors allow otherwise impossible sensor applications, such as monitoring dangerous, hazardous, unwired or remote areas and locations. This technology provides almost unlimited installation flexibility for sensors and increased network robustness. Furthermore, wireless technology reduces maintenance complexity and costs, although this technology is still in the early stages of development.

1.2 Radio Frequency Characteristics

Wireless technology includes RF (Radio Frequency) systems. The characteristics of radio waves in any frequency band govern how useful those frequencies are for the service necessary. The most significant characteristic, is how signals are transformed or distorted, by absorption and reflection, by the air and other physical objects before reaching the receiver. Some

properties of radio waves can be used to modify the information of the wave. These properties are: wavelength, frequency, amplitude and phase.

RF signals are RF waves that have been modulated to information contain. The behaviors of these signals can be detected and predicted. They propagate differently into different materials and they can interfere with other signals. RF signal behaviors and their implications depend on the following parameters:

- Gain
- Loss
- Reflection
- Refraction
- Diffraction
- Scattering
- Absorption
- VSWR
- Return Loss
- Amplification and Attenuation
- Wave Propagation
- Free Space Path Loss
- Delay Spread

Antenna is used to transmit and receive the RF signals. An antenna is a passive device, and cannot amplify a signal. It is designed to provide the most efficient method of radiating the signal. The antenna design depends on the signal frequency, the environment in which it is to be used, and the spread of the signal required.

The basic form of antenna is known as the half-wave dipole. It consists of a single element with the feed from the transmitter or receiver at its center. Its length is exactly equal to one half of the wavelength of the signal. Other commonly used types of antennas are: wire, aperture, microstrip, reflector, and arrays. Each antenna has some properties as a radiation pattern and design parameters. The radiation fields of the antenna can be divided into three regions:

- Reactive Near Field

- Radiating Near Field or Fresnel Region
- Far Field or Fraunhofer Region

1.3 Wireless Sensors

Recently wireless devices have been used for sensing applications due to a growing development of transmission and communications interface. Further technologies can be employed for wireless sensors, such as RFID (Radio Frequency Identification) for example. Indeed, a simple ID tag can be integrated with microprocessors, sensory systems, conditioning electronics for realizing a smart wireless device with sensing, computational and communication capabilities. In particular, the combination of RFID technology with sensing systems allows an extension of the application area of smart tags to environmental monitoring, food quality monitoring, home automation and many other applications. Moreover, this device can be employed in networks, named wireless sensor networks, where each smart tag represents a node (Fig. 1.1).

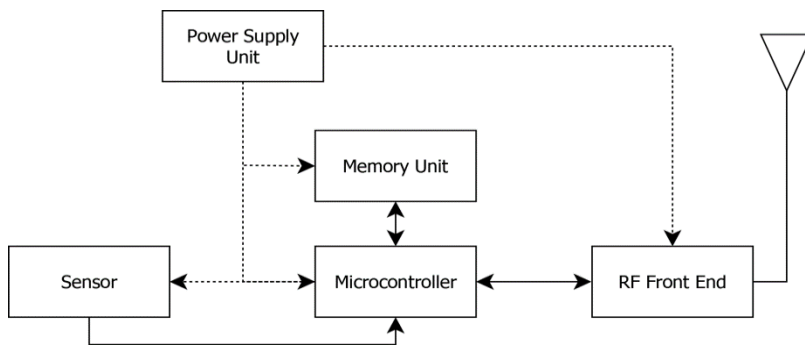


Fig. 1.1 Block Diagram for wireless sensor node

A Wireless Sensor Network (WSN) generally consists of a base station (or “gateway”) which is able to communicate with a number of wireless sensors via a radio link. Data is collected at the sensor node and transmitted to the gateway. The transmitted data are then processed by the system.

To satisfy the needs of different application, a modular design approach is usually adopted in order to provide a flexible and versatile system. A memory unit is inserted to allow the node to acquire data from the gateway or when an event happens. In addition, the node is also equipped with a microcontroller, whose flexibility is certainly one of the most important technical features of the device.

A WSN has the potential for many applications: e.g. for military purpose, it can be used for monitoring, tracking and surveillance of borders; in industry for factory instrumentation; in a large metropolis to monitor traffic density and road conditions; in engineering to monitor buildings structures; in outdoor environment to monitor forest, oceans, precision agriculture, etc. Others applications include managing complex physical systems like airplane wings and complex ecosystems [2].

Minimizing the power consumption of wireless sensor nodes is the fundamental problem concerning the design of these devices. Commonly, a large amount of power is required by radio subsystem. For this reason, it is favorable to transmit data only when it is needed. Consequently, a duty-cycled operation of the RF front-end is usually implemented.

Today, batteries represent the principal energy source as regard the node power supply. Thanks to the improvements in battery technology, their energy density with respect to volume and weight (volumetric and gravimetric energy density) has improved by a factor of three in the past 15 years[3]. Table 1.1 shows some typical values of energy densities and self-discharge values for commercial batteries.

A crucial issue is battery lifetime which has up to now limited the diffused adoption of WSNs, where there are a lot of small sensor nodes to power up. Solutions different from standard batteries have been examined, to overcome such restriction. One possibility is to implement energy storage systems that contain a larger energy density. For this reason miniaturized fuel cells represent one promising technology [4].

Table 1.1 Characteristic of battery

Battery Type	Vol. Energy Density Wh/dm ³	Grav. Energy Density Wh/Kg	Self-discharge % per year	Cycle Life n ^o
Alkaline	300	125	4%	1
Ni-Cd	100	30-35	15%-20%	300
Ni-MN	175	50	20%	300
Li-Ion	200	90	5%-10%	500

Fundamentally, a fuel cell is a power generator that use chemical fuels (i.e. hydrogen or methanol). The gravimetric energy density of these batteries is estimated to be three to five times larger than Li-ion systems. However, the problem of maintenance has not been resolved because these cells need to be refilled of chemical fuels.

Recently, the power supply issue has been limited by energy harvesting systems, which are able to accumulate the necessary power from the environment (e.g. thermal energy, vibrational energy, solar energy or RF radiation). This energy is stored usually in a capacitor and could be used to supply the whole system. However, such an approach enables battery-free operation allowing the deployment of potentially maintenance-free wireless sensor networks and theoretically an infinite lifetime.

1.3.1 Applications

RFID technology is typically and primarily used for identification and tracking purposes. In those application class many tags deployments can be addressed, such as anti-theft, parcel movements and public access areas. However, the increase of tags functionalities, and especially the feasibility of providing RFID systems with sensing capabilities, determines the using area of the smart tags to be enlarged to monitoring applications and their use in the development of wireless sensors. These sensors differ in autonomy, form factor and their configuration, but they all face the same technological objectives such as lifetime, functionality, sizing and costs.

For example, wireless sensor is an auspicious technology for health care applications. Recently, sensor network platforms have been used to monitoring the human activity, in order to find various biological and physiological signals. This approach can help solve the longstanding problem of how to infer human activity [5]. Smart tags can be employed for recording, body temperature, for example, in post-operation patients where contactless devices are preferable since they allow an hygienic and non-invasive measurement method (Fig. 1.2). Moreover, long-term monitoring plays an especially important role in improving diagnosis and therapy in modern medicine. Again, smart tags can be applied potentially for the healthcare of elderly people providing monitoring during their daily routines[6].

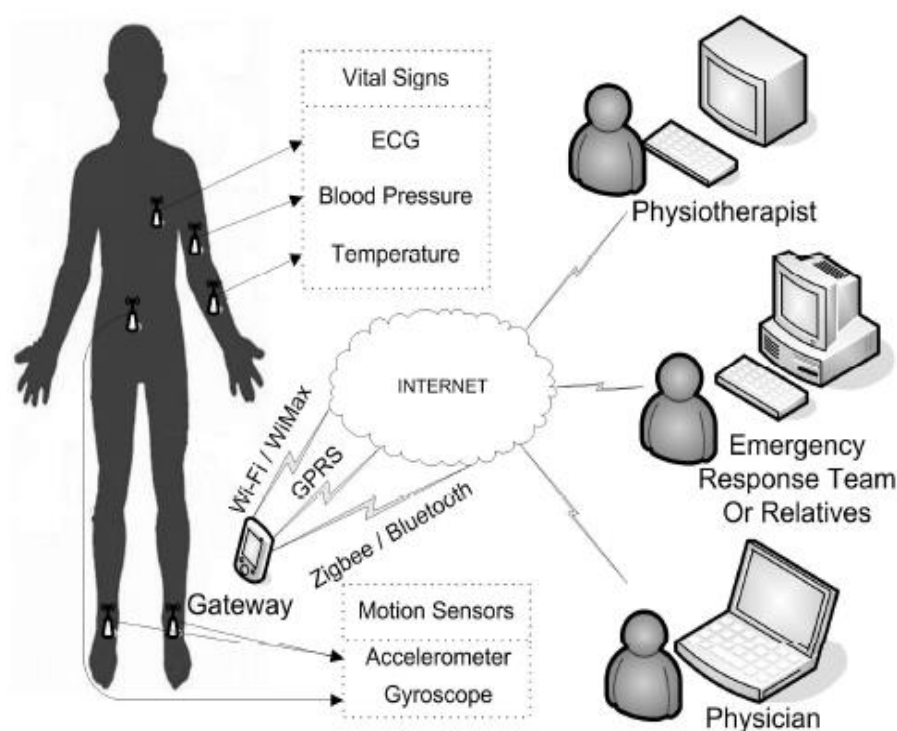


Fig. 1.2 Example of a Body Area Network[6]

Wireless sensors have been positively used in many industrial applications such as security, control, maintenance, monitoring. A typical usage consists of a collection of sensors, and actuators connected to the central control unit (workstation) using standard RF-links (Fig. 1.3). The sensors are directly connected to the workstation through a RF link.

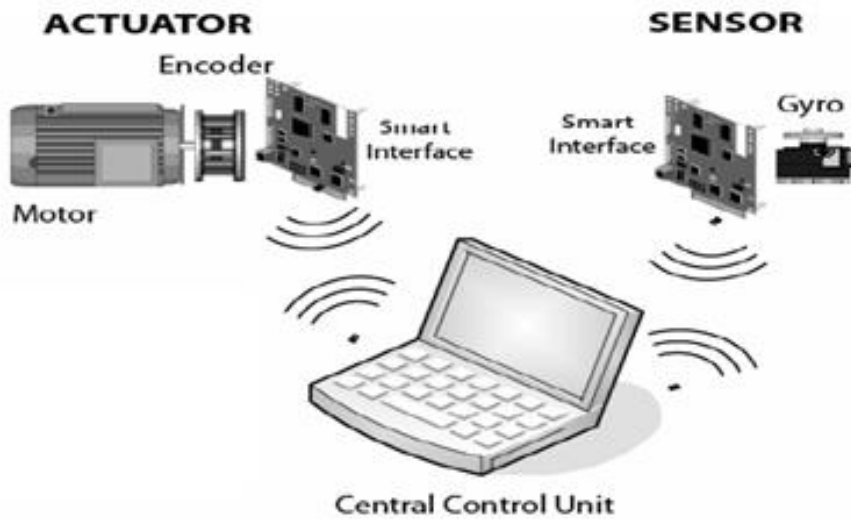


Fig. 1.3 Typical application in industrial scenario [7]

Each sensor or actuator has a reconfigurable wireless or smart sensor interface (SSI). The interface receives data from the sensors, transmits the command to the actuator, and provides a data communication interface to the workstation [7].

Also in the Agriculture-Food sector the development of wireless sensor is emerging. These technologies are very promising in several fields such as environmental monitoring, precision agriculture, cold chain control and traceability [8]. In this contest a demonstration of the system along an intercontinental fresh fish logistic chain have been developed. The usage of wireless sensors presents important advantages regarding conventional traceability tools[9].

Two main applications can be addressed into environmental monitoring: data collection and security monitoring. In both cases smart tags are usually employed over a long period of time at known locations. Therefore, extremely long lifetime devices are required.

In [10] an RF powered transponder with a temperature sensor and a photo sensor is used in environmental monitoring applications. A base station enables the tag that activates the collecting and transmitting of data. In Fig. 1.4 the layout of this system is shown.

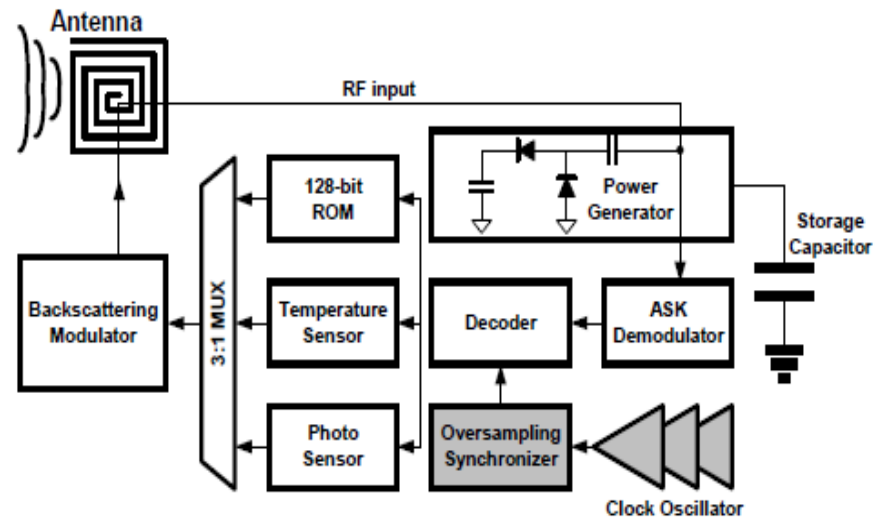


Fig. 1.4 Block diagram of a CMOS RFID tag for environmental monitoring [10]

Subsequently, in security monitoring applications smart tags continually monitor the environment, by mean of one or more sensors, to detect an anomaly. With respect to environmental data collecting, each transponder has to frequently check the status of its sensors but it only has to transmit a data report when there is a security violation. Once detected, a security violation must be communicated to the base station immediately. Therefore, in security monitoring applications reducing the latency of an alarm transmission is more important than reducing the energy of the transmissions. This is because alarms are expected to be rare. In a fire security system, for example, alarms would very seldom be signaled. In the event that one does occur, a significant amount of energy could be dedicated to the transmission.

1.3.2 System evaluation metrics

Wireless sensors must have appropriate characteristics in order to fully operate in each application. For example, smart tags should be equipped with transmitters, in data collected applications, that request minimum power in a certain range communication, since data transmission is required at regular intervals. On the contrary, in security applications, transmission section is

enabled only when an anomaly is detected, therefore a fast response device is essential.

A set of metrics can be established in order to evaluate the performance of a transponder. These metrics are often interrelated: as a result an improvement in one evaluation metric, e.g. communication range, often comes at the expense of another, e.g. power.

Lifetime

The expected lifetime of smart tags is the key parameter in most applications. Indeed, a long lasting device can be placed out in the field and autonomously work for months or years. The energy supply is the principal limiting factor for the lifetime of such a device.

In some conditions it may be possible to exploit external power. However, the ease of installation is one of the main benefits to wireless systems. Devices that required external power supply, negates this advantage.

Smart tags should be self-powered. They need to contain stored energy to function, or to have the ability to source energy from the environment through external supplies like solar cells or RF generator for example [11]-[12].

Therefore, the main objective of both of these possibilities is that the standard energy use is minimal. Radio power consumption is used to ascertain the lifetime of an energy supply.

When the transmission of output power or radio duty cycle is reduced, power consumption can fall.

Power Consumption

Smart tags need to operate on ultra-low power in order to comply with specific operating conditions. It is possible to achieve a very low power consumption through the combination of low- duty cycle operation methods and low- power hardware. Radio communication makes up a significant percentage of the total energy budget during active operation: therefore radio activity needs to be reduced. When this power is reduced it means that the

antenna receives less power and the communication distance is therefore reduced. Consequently, the transmission output power can be lowered.

Communication Range

Besides expected lifetime, coverage is the principle evaluation metric for a wireless system, due to greater communication benefits over a wider area. The distance covered relies on the working frequency and level of power delivered to the antenna. Increasing the power to be injected into the radiating element enhances the radiated power and communication range. When evaluating antenna performance, smart tags used in environmental monitoring applications commonly need an isotropic radiation pattern this is due to the fact that the relative orientation between transponder and base station are not fixed. The increase of the free space loss and, the decrease of the radiated power at given distance and power delivered into the antenna determine the reduction of antenna size at high frequency.

Robustness

It is of paramount importance that smart tags are suitably robust. Therefore devices must be physically robust and contain robust functionalities. This can be achieved by circuit design: for example, the robustness of wireless links to external interference can rise significantly through the use of multi-channel and spread spectrum radios[13]. Monolithic tags enhance robustness against mechanical stress and for smart tags to be utilized in outdoor applications they must be appropriately packaged to minimize atmospheric damage.

Size and Cost

The dimension and market price of a smart tag will obviously have a great impact on its exploitation. Smaller smart tags can be widely used in conventional systems and in various locations. Similarly, cheaper smart tags are more economically viable and accessible.

1.4 Energy Harvesting

Ambient energy harvesting is the process where energy is obtained from the environment. Energy harvesting, in general, is the conversion of ambient energy into usable electrical energy.

Energy Harvesting technologies differ in macro e micro scale. Macro-scale systems feed the energy network, typically adding kilowatts or megawatts to the power distribution system. On the contrary, micro-scale technologies scavenge milliwatts or microwatts to supply ultra-low power (ULP) devices. In this way is possible to create a perpetual devices with theoretically infinite lifetime.

A variety of techniques are available for micro energy scavenging, such as mechanical vibrations, electromagnetic sources, light, acoustic, airflow, heat, and temperature variations. The main differences in these power sources are the power density as shown in Table 1.2.

Table 1.2 Power Density of Energy Harvesting source

Power Source	Density Energy
Light	
Indoor	$10\mu\text{W}/\text{cm}^2$
Outdoor	$10\text{mW}/\text{cm}^2$
Thermal	
Human	$25\mu\text{W}/\text{cm}^2$
Industry	$1\text{-}10\text{mW}/\text{cm}^2$
Vibration	
Human	$4\mu\text{W}/\text{cm}^2$
Industry	$100\mu\text{W}/\text{cm}^2$
Radio Frequency	
GSM	$0.01\mu\text{W}/\text{cm}^2$
Wi-Fi	$0.001\text{mW}/\text{cm}^2$

Solar energy is one of the most commonly used source, featuring high power. The average power density during daytime is about 100 mW/cm^2 with about 20% of average conversion efficiency. In addition a solar panel can also operate in a hybrid mode in conjunction with other types of energy source [14]. The size of a solar panel determine the available amount of power and the values of voltage or current that can be generated. However, large area of solar panel is required to collect sufficient amounts of ambient solar power due to low conversion efficiency of 10%–40%, considering also that its orientation is critical to collect solar power. It is also inefficient on a cloudy day or at night due to the lack of the source.

Another power source commonly utilized is the thermal energy. The temperature difference in thermoelectric devices generates directly electrical power, taking advantage of thermoelectric effects, such as the Seebeck effect or the Thomson effect. As shown in **Fig. 1.1**Fig. 1.5, an energy density of about $20\text{--}60 \text{ }\mu\text{W/cm}^2$ is produced by a thermoelectric generator, when it utilizes the human body as the heat source at room temperature of $18^\circ\text{C}\text{--}25^\circ\text{C}$ [15]. Thermoelectric devices can operate continuously as far as there is a temperature difference or a heat flowing across them. The thermoelectric energy-harvesting devices typically need relatively large form factors in terms of volume to generate useful amounts of power.



Fig. 1.5 Wearable Thermoelectric Energy Harvesting used for measurements of thermal properties of humans and power generation on people at different ambient conditions[15]

The piezoelectric effect generates electrical voltages or currents from mechanical strains, such as vibration or deformation. Typical piezoelectric-based energy harvesters keep creating power when there is a continuous mechanical motion, such as acoustic noises and wind, or they sporadically generate power for intermittent strains, such as human motion (walking, clicking a button, etc.). Typical output power density values of usual piezoelectric materials are around $250 \mu\text{W}/\text{cm}^3$ but they can create more power when a motion or deformation is intense [16]. The piezoelectric energy harvesters or piezoelectric transducers are a well-developed technology, and numerous energy-harvesting modules of this type have been reported [17]. The volume of the piezoelectric power generators is relatively small and light compared to other energy harvesting devices, because a small crystalline structure is able to generate power in these configurations. However, the output power of piezoelectric effect-based power generators has a large dynamic range when irregular motions, such as human motions, are utilized as the driving force.

1.4.1 RF Energy Harvesting

RF energy harvesting involves the usage of external sources of radio frequency waves that are present in the environment, natural radiation, wireless communication, broadcasting etc.

In certain applications radio frequency is the preferred method to power the electronics. Indeed, the huge development of RF communications over the last decades makes RF energy available anytime and everywhere. This energy is virtually in the air, anytime day or night but at differing power levels. The growth wireless technology has brought to a growing interest in RF energy harvesting applications.

The RF energy harvesters system convert directly the RF signal in a DC power (as shown in Fig. 1.6) that can be used to supply ULP systems. RF energy is available in a wide array of frequency bands due to everyday technologies:

- Cell Phones
- Radio Towers

- WiFi Routers
- Laptops
- TV Signals
- Direct RF energy source, dedicated to providing RF energy for harvesting

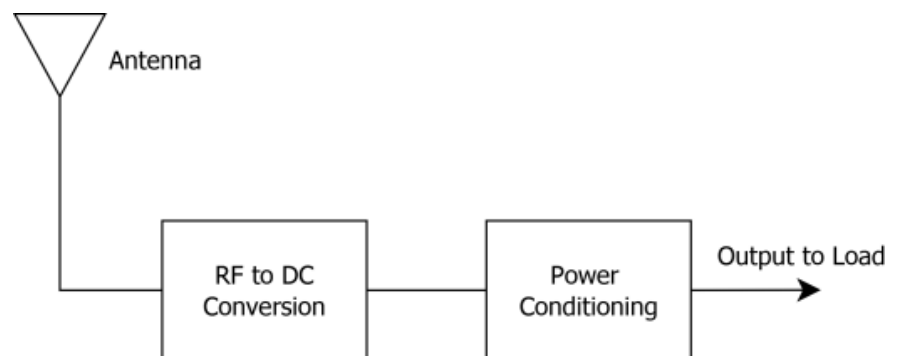


Fig. 1.6 RF to DC converter

The ambient RF power density is usually higher in downtown urban areas and in the proximity of the power sources (e.g., TV towers) [18].

Ambient RF energy-harvesting systems can be easily integrated with different types of antennas as well as with other harvesting technologies, such as the solar cells[19] Fig. 1.7.

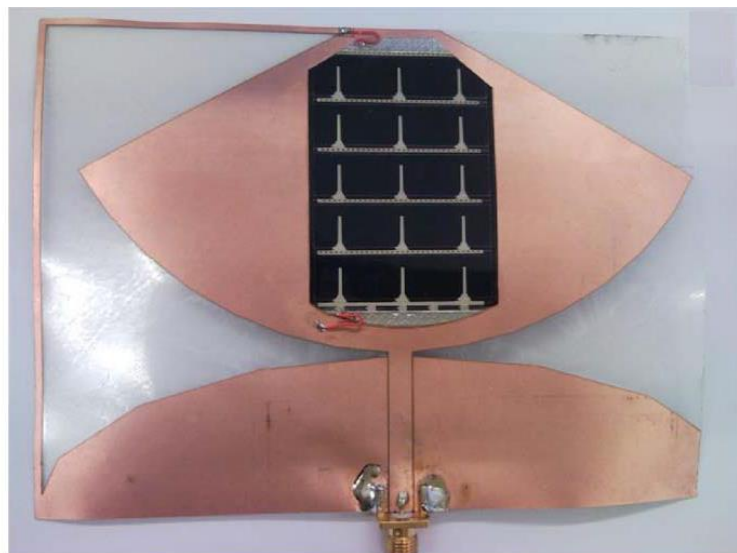


Fig. 1.7 Printed monopole solar antenna [19]

It is more challenging due to very low-power-density values and the low RF–dc diode conversion efficiency values to utilize ambient RF power when power harvesters are far away (more than 6 km) from the wireless sources but the harvested RF power can be still utilized by appropriately optimizing the duty cycle of the system (typically below 6%–8%) [20]. The conversion efficiency of RF–dc conversion circuits, such as a charge pump or a rectifier, is about 10%–30% due to low input power levels (from -30 to -20 dBm) but the harvested RF power can generate about 1.8–4.0 V with a total converted power of about 100 μ W. This power level is sufficient to operate battery-assisted sensors periodically for a long time (more than five years). The harvested RF power gets larger as the antenna gain and energy density of the ambient environment increase, since the RF–dc conversion efficiency is improved due to the increased input power to the rectifying circuit.

RF harvesting systems rely on a RFID-like approach, in which power is provided to passive tags through the radio waves emitted by a reader. The system realized using this technology is a solution with great flexibility. RF-powered devices can be positioned in inaccessible or dangerous areas, or positions where battery replacement is highly impossible. For this reason, a RF-powered approach was chosen as the best solution for the design of a battery-free wireless sensor.

Wireless sensor nodes, commonly work within unlicensed bands, which are defined as industrial, scientific and medical (ISM) radio bands. The telecommunication regulatory authorities states that an unlicensed product user doesn't need an individual license. However, this differs greatly from unregulated. Wireless devices must follow rigorous regulatory guidelines.

The International Telecommunication Union Radio communication Sector is accountable for radio-communication systems standards and defining ISM RF-powered transceivers for WSNs bands. Below is a Table 1.3 **Table 1.1** highlighting the frequency range and center of ISM bands [21].

The national radio regulations may produce different frequency bands in some countries.

Table 1.3 ISM frequency bands

Frequency range		Center frequency
6.765 MHz	6.795 MHz	6.780 MHz
13.553 MHz	13.567 MHz	13.560 MHz
26.957 MHz	27.283 MHz	27.120 MHz
40.660 MHz	40.700 MHz	40.680 MHz
433.050 MHz	434.790 MHz	433.920 MHz
902.000 MHz	928.000 MHz	915.000 MHz
2.400 GHz	2.500 GHz	2.450 GHz
5.725 GHz	5.875 GHz	5.800 GHz
24.000 GHz	24.250 GHz	24.125 GHz
61.000 GHz	61.500 GHz	61.250 GHz
122.000 GHz	123.000 GHz	122.500 GHz
244.000 GHz	246.000 GHz	245.000 GHz

1.5 Proposed Solution

In this thesis, two kinds of wireless sensors with different design strategies have been proposed.

In the first case an autonomous UHF-RFID sensor platform has been realized, using off-the-shelf discrete components. The main advantage of this system is that the communication interface is used for both data collection and energy transfer. In addition, the flexibility of the general purpose microcontroller is certainly one of the most important technical features of the device.

This solution presents several limitations as:

- the circuit size, making it a macroscopic object
- the need to use discrete components increasing the cost of the finished product

- over and above to require welding and machining of the PCB.

To overcome these obstacles, a second solution has been proposed by trying to achieve a compact, economical and sufficiently accurate system. Researches into related literature were made in order to discover the most advanced solutions. The ambitious objective has been to achieve a wireless sensor that integrates the transducer, the oscillator and the circuitry needed to operate the all in one chip. This microchip has been specifically designed for the monitoring of High concentration photovoltaics (HCPV) modules.

2 UHF-RFID Sensor Platform

In this chapter a Wireless Smart Sensor Platform, compatible with EPCglobal Class-1 Gen2 readers, is presented. The platform is comprised of a five stage Dickson voltage multiplier, a dynamic impedance matching network (DyIMN), an XLP microcontroller (MCU) and an RFID tag IC with an embedded temperature sensor. Device range operations have been assessed up to a distance of 1.5 m from the RF source, corresponding to a minimum RF input power of -10 dBm. Firmware optimization leads to a reduction of the power dissipation below 500nW in sleep mode, allowing an optimal energy harvesting and storage from the RF source. The harvested power enables logical operations to be completed from MCU, thus enabling sensing and storing of temperature measurements directly into the user memory of an RFID tag. Also the efficiency of the energy harvester is calculated from the MCU, hence tuning the DyIMN dynamically to respond over a wide range of input power and load impedance.

2.1 Introduction

Sensor platforms that can be activated and powered remotely, pave the way to a wide range of sensing and monitoring applications. RF fields can be generated on demand, thus providing a more stable and convenient power supply for harvesting system, despite the lower efficiency compared to sunlight, thermal gradients, mechanical, convection flows or other forms of

harvestable energy. Consequently, the need for standard battery replacement or maintenance is eliminated.

RF devices that act as sensing nodes can be mounted in positions that are difficult for humans to be accessed. They can even be embedded within the structure to be monitored during its construction or during the lifetime of the object subject to modification. The usage of backscattering modulation methods enables data transmission to be implemented using the same fields that power the nodes.

Batteryless powered devices are most often used in radio frequency identification (RFID) or passive RF tags [22]-[23] which works within a 1–3 meter range.

The main advantage of sensor platforms that work in the UHF – RFID band is that the communication interface is used for both data collection and energy transfer. Several state-of-the-art platforms [24]-[25] use the signal transmitted by the RFID reader for harvesting the energy, thus enabling a one-way communication from tag to reader.

2.2 UHF-RFID Sensor Platform Architecture

Ambient energy can be harvested from a converter or transducer and then stored inside a storage device, such as a battery or a supercapacitor. Fig. 2.1 shows the general structure of an energy-harvesting enabled wireless sensor platforms. An optimized power consumption can be obtained using a power management unit (PMU) through a desired duty cycle setting. The lifetime of “main” power sources can be improved through the introduction of energy-harvesting systems. Energy harvesting systems can periodically recharge the main power source or operate as an auxiliary source too. It is possible to remove supply power when the harvested energy is enough to supply the whole system. In this case a truly standalone (“battery-less”) self-powered system is obtained.

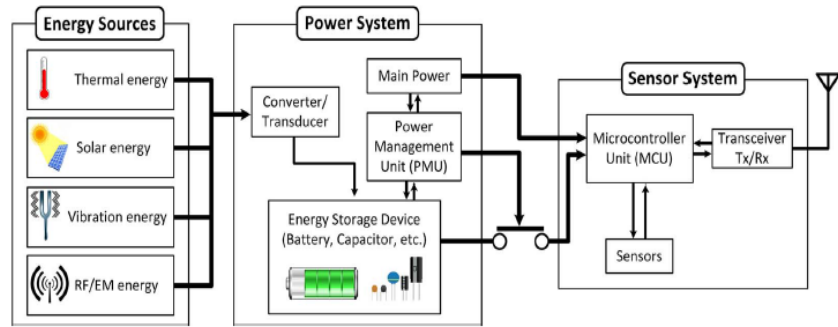


Fig. 2.1 General block diagram of an energy-harvesting-enabled wireless sensor platform system

In recent time, the growth of RFID technology has produced robust systems, capable of wirelessly powering and querying a tag. For this reason, RFID technology allows a new class of wireless, battery-free devices with communication, sensing, computation, and data storage capabilities. Without batteries, these devices can theoretically be operated for an infinite time.

The first developers of UHF RFID tags were Smith et al. in 2005 with their Wireless Identification and Sensing Platform (WISP) realizing the ID-modulation instrument for sensor data transmission [26].

In Fig. 2.2 α -WISP is depicted, it uses two mercury switches to mechanically toggle between two commercially available RFID integrated circuits. The mercury switches are mounted in a geometrically antiparallel configuration, so that when one is open, the other is closed. For this reason, two RFID are necessary to distinguish the different acceleration state.

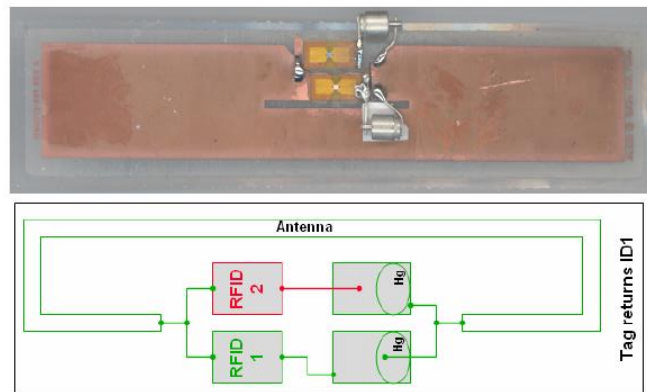


Fig. 2.2 Schematic diagram of α -Wisp battery-free one bit accelerometer (left); photograph of α -Wisp (right)[26]

The WISP potentialities have been enhanced by the same authors who, developed the first battery free programmable UHF RFID sensor platform in 2008 [25], as shown in Fig. 2.3.

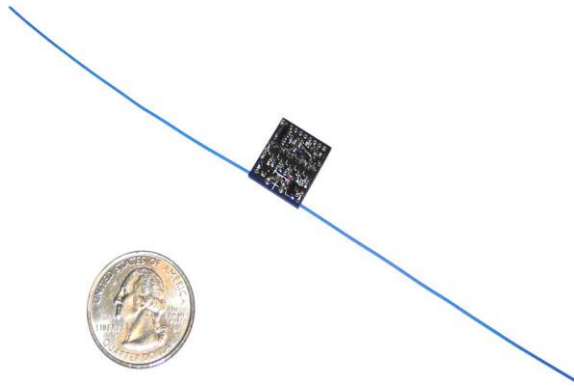


Fig. 2.3 Wisp Platform[25]

Another low cost general-purpose sensor tag is proposed in [27]. This device can be connected to generic sensors and when it is interrogated by a standard UHF reader, it sends the sensor value through a proper electronic code. In Fig. 2.4 a diagram of the sensor tag (S-TAG) is shown. Here, a generic sensor can be connected at the S-TAG and the measured parameters are transmitted toward the RFID reader by means of a proper set of IDs.

An enhanced UHF RFID tag, realized using inkjet-printing technology on a flexible organic substrate and equipped with a microcontroller and sensors, is proposed in [28].

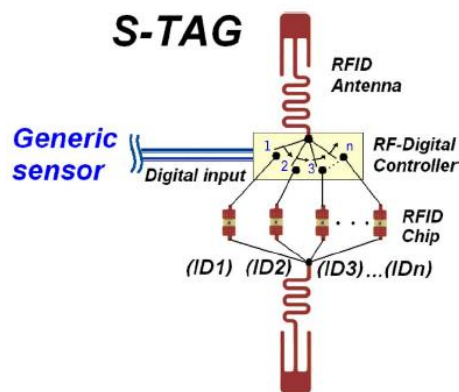


Fig. 2.4 Simplified scheme of the designed RFID S-tag [27]

In [29], one of the first passive UHF RFID humidity sensor tags fabricated using inkjet technology is presented. The sensor tag is based on a RFID integrated circuit (IC) and it operates solely in a passive operation mode.

In [30] a passive multi-standard RFID tag implemented in a 0.13 μ m bulk CMOS process and enhanced with sensing and localization functionalities is described.

An interesting design strategy for fully-passive RFID sensors is proposed in [31]. Here the change of antenna shape is used to monitor mechanical stress. This sensing mechanism, besides being extremely susceptible to radio propagation phenomena, is not compatible with existing RFID infrastructures. This is due to the fact that it requires expensive equipment, such as vector network analyzers or customized receivers, to reliably extract sensor dependent characteristics from backscattered radio signals.

UHF RFID tag ICs have been developed without internal memory to minimize the cost. UHF RFID tag ICs have been developed without internal memory to minimize the cost. However, the RFID system performances using tags with only unique IDs is restricted in term of transfer data time because of the data search sequence performed in the backend system and the data transfer time between the reader/writer and the backend system. On the other hand, in [32] the design optimization of UHF RFID tag IC with rewritable memory in terms of cost, communication range and transaction time is described.

De Donno et al., in [24] have recently presented the design and performance evaluation of a long-range, self-powered, Gen2-compliant, and programmable RFID sensor platform (RAMSES). The prototype of this platform is shown in Fig. 2.5.

In addition to recent academic research, there are several commercially available Gen2 tags that incorporate sensing, computation, and data-logging capabilities for unconventional RFID applications. For example proposes the SL900A sensor tag [33] available from Austria Micro System, Easy2Log tag by CAEN RFID [34] and the SensTAG by Phase IV [35].



Fig. 2.5 RAMSES Platform [24]

A block diagram of the UHF-RFID sensor platform, proposed in this thesis, is depicted in Fig. 2.6. The system is implemented using off-the-shelf discrete components and includes a dipole antenna, a voltage multiplier, a dynamic impedance matching network (DyIMN) [36] a supercapacitor to store the surplus power, an ultra-low power microcontroller (MCU), and a RFID tag IC with an embedded temperature sensor for the wireless communication with EPCglobal Class-1 Gen2 readers.

When the platform enters the RF field of a reader, the rectifier circuit is activated, thus harvesting the RF energy to provide a regulated DC supply voltage (1.8Vdc) to the microcontroller and the tag.

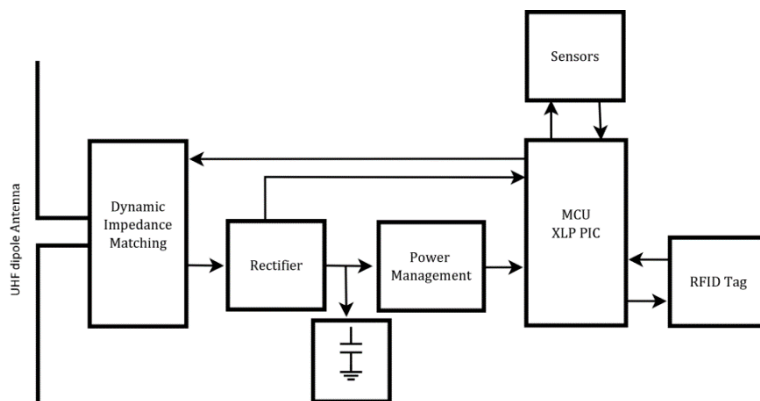


Fig. 2.6 Block diagram of the proposed RFID sensors platform

2.3 Rectenna

The term “rectenna” derives from the two words rectifier and antenna. It is a device that captures microwave power and instantly converts it into a DC power [37].

A rectenna is composed of an antenna and a diode rectifier circuit, as depicted in Fig. 2.7. The performance of the rectenna depends on its RF-DC conversion efficiency, input power and load values. The conversion efficiency is defined as the ratio of the rectifier DC output voltage and the RF power input on the antenna.

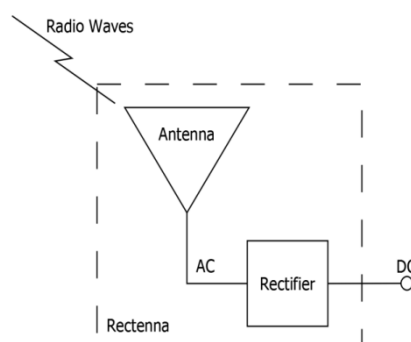


Fig. 2.7 Generic block diagram of a rectenna

Ideally, when using ideal diodes under these circumstances, conversion efficiency would not depend on RF input power. However in reality, it strongly does.

2.3.1 Antenna

An antenna is a metallic device capable of transmitting or receiving electromagnetic wave. The resonance frequency of an antenna is determined by its geometrical characteristics, such as shape and dimension. Common typologies of this radiant element are: wire, aperture, microstrip, reflector, and arrays. Each antenna has some different characteristics of radiation pattern and design parameters.

As shown in Fig. 2.8, the radiation fields of the antenna can be divided into three regions [38]:

- *Reactive Near Field Region* is defined as “that region of the field immediately surrounding the antenna wherein the reactive field

predominates.” For most antennas, the outer boundary of this region is given as:

$$R_1 < 0.62 \sqrt{\frac{D^3}{\lambda}} \quad (2.1)$$

where R_1 is the distance from the antenna, λ is the wavelength and D is the largest dimension of the antenna.

- *The radiating near-field (Fresnel) region* is defined as “that region of the field of an antenna between the reactive near-field region and the far-field region wherein radiation fields predominate and wherein the angular field distribution is dependent upon the distance from the antenna”. The region where this region exists, is given by:

$$0.62 \sqrt{\frac{D^3}{\lambda}} < R_2 < \frac{2D^2}{\lambda} \quad (2.2)$$

- *The far-field (Fraunhofer) region* is defined as "that region of the field of an antenna where the angular field distribution is essentially independent of the distance from the antenna". The region where this region exists, is given by:

$$R \geq \frac{2D^2}{\lambda} \quad (2.3)$$

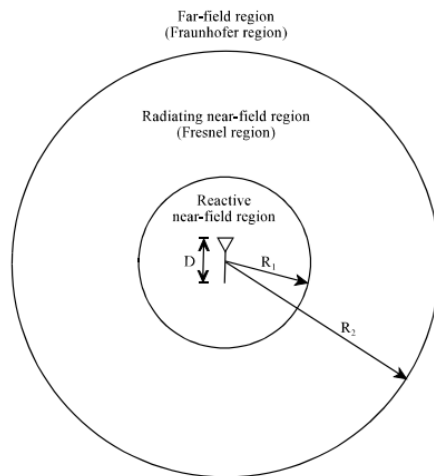


Fig. 2.8 Antenna Field Regions

Dipole Antenna

The dipole antenna is the simplest radiating and receiving element, consisting essentially of two symmetrical wires laying on a straight line. If the antenna is made from a single metal branch, it can be defined a monopole that can be directly connected to a coaxial line. It is well known that the basic characteristics of an antenna used for receiving RF signals, such as the gain, the directivity or the impedance, are identical to those calculated when this element is used to radiate an electro-magnetic field, which is the most common approach. For this reason, we will refer to a transmitting antenna in the following.

In a dipole antenna, the electric field lines of force are detached from the antenna to form free-space waves[39]. Fig. 2.9(a) depicts the lines of force generated between the arms of a small center-fed dipole in the first quarter of the period. At this point, the charge has reached its maximum value (assuming a sinusoidal time variation) and the lines have traveled outwardly a radial distance $\lambda/4$.

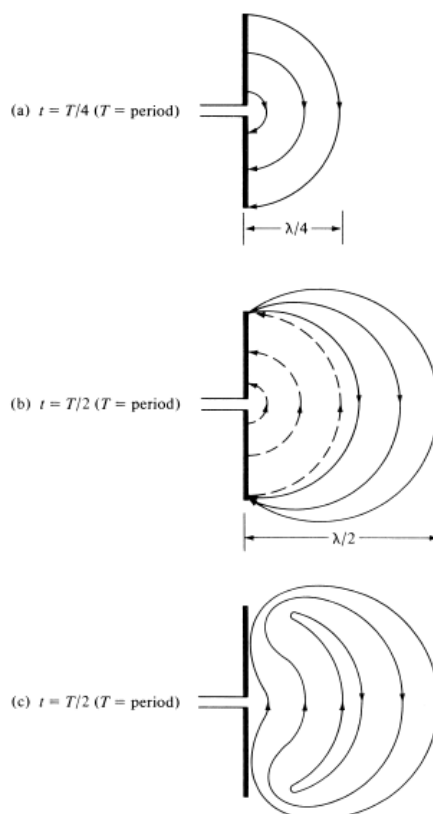


Fig. 2.9 Formation and detachment of electric field lines for a dipole

Assuming that the number of lines formed is three, in the next quarter of the period, the original three lines travel an additional $\lambda/4$ (a total of $\lambda/2$ from the initial point) and the charge density on the conductors begins to decrease. The reason for this decrease, at the end of the first half of the period, is due to opposite charges that have neutralized the conductor charges. There are three lines of force created by the opposite charges and they travel at a distance of $\lambda/4$ during the second quarter of the first half, they are shown dashed in Fig. 2.9(b). The end result is that there are three lines of force pointing upwards in the first $\lambda/4$ distance and the same number of lines pointing downwards in the second $\lambda/4$. Since there is no net charge on the antenna, the lines of force must have been forced to detach themselves from the conductors and to unite, forming closed loops. This is depicted in Fig. 2.29(c). In the remaining second half of the period, the same procedure is followed but in the opposite direction. After that, the process is repeated and continues indefinitely, forming electric field patterns.

2.3.2 Rectifier

In RF application, the traditional circuit solution adopted for implementing the rectifier stage is based on the Dickson's topology [40] of the voltage multiplier. In Fig. 2.10, the schematic circuit for this topology of rectifier is shown.

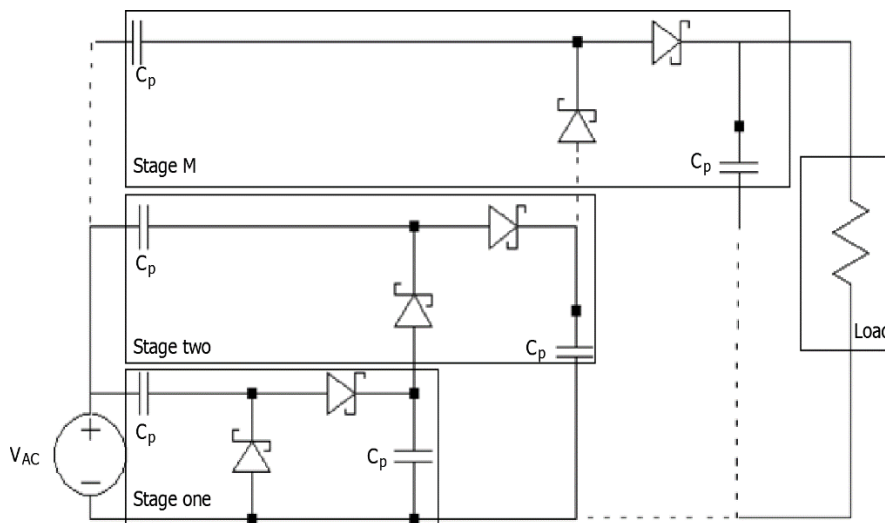


Fig. 2.10 Schematic of a conventional Dickson multi-stage rectifier

Dickson's circuit performance depends substantially on the voltage threshold of the rectifying devices, which reduces the AC-DC conversion efficiency and sets the minimum input voltage to turn on the circuit. The Dickson's output voltage, with $M+1$ pumping devices, can be calculated using the following relation:

$$V_o = M \left(\frac{C}{C + C_p} V_{AC} - \frac{I_o}{f(C + C_p)} - V_{TH} \right) - V_{TH} \quad (2.4)$$

where V_{AC} is the peak-to-peak voltage of the AC input signals, C_p is the coupling capacitor, C is the parasitic capacitance at each pumping node (not shown in Fig. 2.9), I_o is the average current drawn by the output load, f is the operating frequency and V_{TH} is the diode threshold voltage. According to (2.4), the following condition has to be satisfied for a positive voltage to be generated at the output:

$$V_{AC} > \frac{C + C_p}{C} \frac{M + 1}{M} V_{TH} + \frac{I_o}{fC} \quad (2.5)$$

The single stage of the Dickson rectifier is called Voltage Doubler, because the voltage output of this circuit is ideally double compared to the amplitude of the voltage input. As depicted in Fig. 2.11, a Voltage Doubler is formed by a clamper and a single diode rectifier.

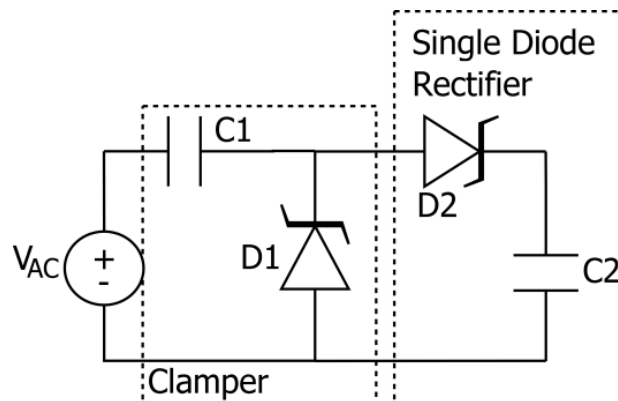


Fig. 2.11 Voltage Doubler

The clamper circuit is a combination of the capacitance $C1$ and the diode $D1$. The function of this circuit is to shift the continuous component of the sinusoidal input voltage, thus setting its lower extreme at an established value.

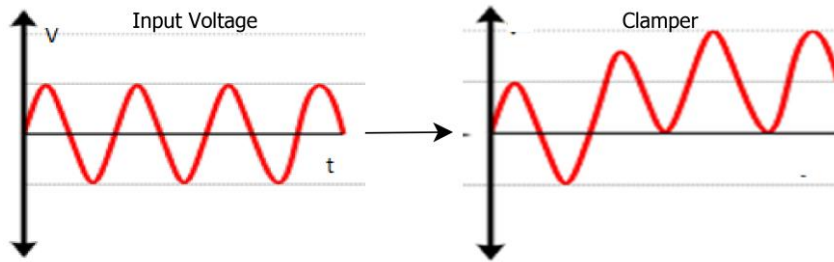


Fig. 2.12 Clamper Effect

As shown in Fig. 2.12, the input waveform has been shifted in order to put the lower extreme in 0V. This result is obtained assuming that the diode is an ideal device. As a consequence, the amplitude of voltage output is always double compared to the amplitude of input voltage (Voltage Doubler). In reality, the amplitude of voltage output is lower because of the diodes parasitic losses.

Subsequently, the second part of the Voltage Doubler is a single diode rectifier made up of the diode D2 and the capacitor C2. This circuit allows the voltage to be converted into a continuous signal.

2.4 Impedance Matching in RF Platform

Antennas provide different input impedance characteristics due to differences in their geometry, frequency band, and input power. In addition, a rectifier, which converts the AC signal received by the antenna into DC, can have different complex input impedances, depending on its design, fabrication technology and working conditions. As a result, the problem of impedance matching occurs between antenna and rectifier. Here it is necessary to maximize the amount of energy transferred to the load. Correct impedance match between the antenna and the electronics is of paramount importance in RF energy harvesters. In order to obtain the maximum power transfer, the configuration and the component values of the matching network Z_{in} must be determined. Although Z_{in} is not constant during the link time, several authors propose the matching to a Z_{in} for the longest range as this fulfills all the power requirements. Kazanc et al. [41] use a method that

optimize the conjugate matching between an antenna with inductive reactive impedance and an integrated circuit with capacitive reactive impedance. Obtaining an antenna with the desired conjugate impedance eliminates the need for an impedance matching network. However, impedance matching can be performed using several other methods including a stub, an inductively coupled loop or nested slot [42]. However, these methods bring further costs and overall increment in system size.

2.4.1 Modified Friis's Equation

In free-space the power received from an RF antenna, P_a can be calculated using Friis' free-space equation:

$$P_a = P_t G_r G_t \left(\frac{\lambda}{4\pi d} \right)^2 \quad (2.5)$$

where P_t is the power transmitted by the reader, G_t is the gain of the transmitting antenna, G_r is the gain of the receiving antenna, λ is the wavelength, and d is the distance between the reader and the tag.

For RF energy harvesting systems, the rectifier efficiency and the polarization loss shall be taken into account, reducing the effective power delivered to the load.

In [43] Shibo He et al. proposed a modification of (2.5) that describes the power delivering mechanism to a wireless platform better:

$$P_a = P_t \frac{G_r G_t \eta}{L_p} \left(\frac{\lambda}{4\pi(d + \beta)} \right)^2 \quad (2.6)$$

where L_p is polarization loss, η can be referred to as the rectifier efficiency, and β is a parameter to adjust Friis' free space equation for short distance transmission.

If the threshold power necessary to power up the electronic load is P_{th} , then the read range d can be calculated as (2.4)-(2.5):

$$d = \frac{\lambda}{4\pi} \sqrt{\frac{P_t}{L_p P_{th}} \eta G_r G_t \tau - \beta} \quad (2.6)$$

The factor:

$$\tau = \frac{4R_{load}R_a}{|Z_{load} + Z_a|^2} \leq 1 \quad (2.7)$$

is the power transmission coefficient, which accounts for the impedance mismatch between the antenna ($Z_a = R_a \pm jX_a$) and the electronic load ($Z_{load} = R_{load} \pm jX_{load}$). Both Z_a and Z_{load} are frequency dependent. In addition, the load impedance also depends on the input power.

The antenna is usually matched at the minimum threshold power level necessary for the electronics to power up.

The amount of power P_{load} that can be absorbed by the electronics from the antenna is given by:

$$P_{load} = P_a \tau \quad (2.8)$$

Consequently, to maximize the amount of power transferred to the electronic load, the transmission coefficient must be maximized.

2.4.2 Impedance Matching Network

An impedance matching network can be inserted between the antenna and the electronic circuit in order to provide the maximum power to the load (Fig. 2.13).

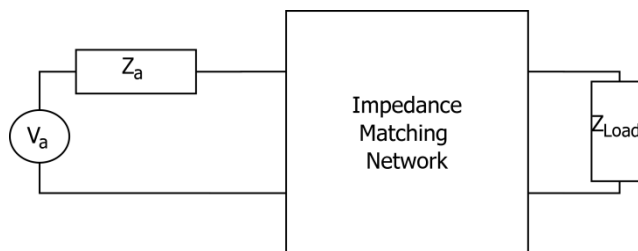


Fig. 2.13 Impedance Matching Network

The usage of inductors and capacitors in series or parallel topology is quite common in an impedance matching network, because these passive elements do not dissipate power and do not add noise to the circuit, while active devices do.

In RF platforms a dual lumped matching networks are commonly used [24]-[25]. This type of network can be realized through two configurations, where the choice depends on the values of Z_a and Z_{Load} .

In the first case, if $R_{Load} > R_a$, the configuration depicted in Fig. 2.14(a) must be chosen.

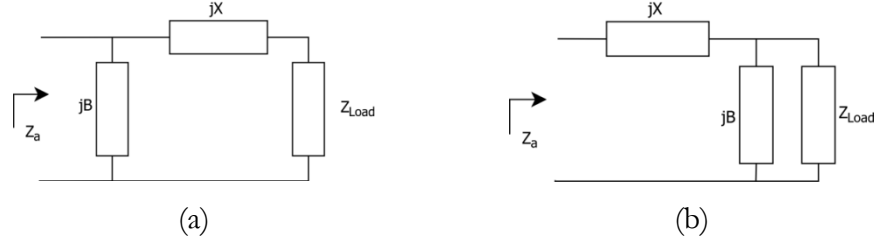


Fig. 2.14 Configurations of dual lumped elements matching network

In this case, the value of Reactance (X) and Susceptance (B) are calculated as following:

$$X = -X_{Load} \pm \sqrt{R_{Load}(R_a - R_{Load}) + \frac{R_{Load}}{R_a} X_a^2} \quad (2.9)$$

$$B = \frac{R_a - R_{Load}}{R_a X_{Load} + R_{Load} X_a + R_a X} \quad (2.10)$$

In the second case, if $R_{Load} < R_a$, the configuration depicted in Fig. 2.14(b) shall be considered .

In this case, the value of Reactance (X) and Susceptance (B) are calculated as follows:


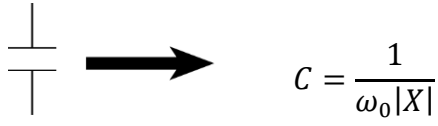
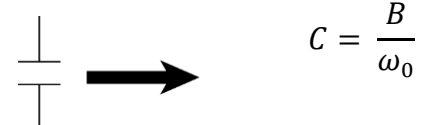
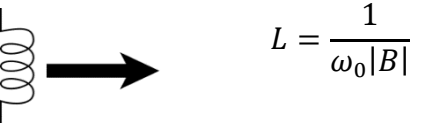
$$X = X_a \pm \sqrt{R_a(R_{Load} - R_a) + \frac{R_a}{R_{Load}} X_{Load}^2} \quad (2.11)$$

$$B = \frac{R_a - R_{Load}}{R_{Load} X_a + R_a X_{Load} + R_{Load} X} \quad (2.12)$$

The choice of which passive component to implement in the network depends on reactance and susceptance values. Considering a RF signal with a

frequency of $f_0 = 2\pi\omega_0$, it is possible to synthesize the reactance (X) and the susceptance (B) using lumped elements, as depicted in Table 2.1.

Table 2.1 Synthesizing Reactance (X) and Susceptance (B) using lumped elements

For Reactance (X)	
If $X > 0$: Use inductor $j\omega_0 L = jX$	If $X < 0$: Use capacitor $\frac{1}{j\omega_0 C} = jX$
	
For Susceptance (B)	
If $B > 0$: Use capacitor $j\omega_0 C = jB$	If $B < 0$: Use inductor $\frac{1}{j\omega_0 C} = jX$
	

2.5 Energy Harvesting Performance

2.5.1 Antenna evaluation

In an energy harvesting circuit, the antenna is the device used to harvest the power captured by the RF signal. In this study, three antenna typologies have been evaluated:

- **$\lambda/2$ Dipole Antenna:** designed to resonate in UHF band. Its length has been calculated as follows:

$$l = \frac{\lambda}{2} = \frac{c}{2f} \approx 17,2cm$$

where $c=300000\text{m/s}$ and $f=868\text{MHz}$. The series resistance of the equivalent resonant circuit is equal to the radiation resistance, which is about 73Ω in air. Dipole antenna has been designed on a PCB substrate.

- **Meander:** a meandering monopole for 868 MHz or 915/920 MHz, and an overall size of 38 x 25 mm (Fig. 2.15).

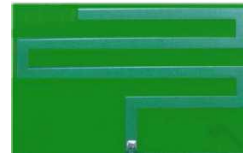


Fig. 2.15 Monopole Meander

A pi-matching network can be used at the feed point to match the antenna at 868 MHz, since the geometry of the ground plane affects the impedance of the antenna. The pi-network can be used to compensate for detuning caused by plastic encapsulation and other objects in close vicinity of the antenna. The impedance of this antenna is approximately adaptable to 50Ω through the correct dimension of the ground plane [44].

- **Miniaturized antenna:** the third antenna topology used is the Mitsubishi AM11DG-ST01[45]. It is a metallic spiral wound on a ceramic material with high dielectric constant, as shown in Fig. 2.16.

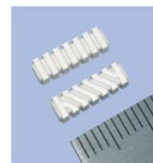


Fig. 2.16 Miniaturized antenna

With an appropriate ground plane, the system can be adapted to 50Ω .

The performances of the antennas have been compared by measuring the DC output voltage of a rectifier that has been connected to the antenna's output.

The systems have been mounted on PCB substrate, as depicted in Fig. 2.17.

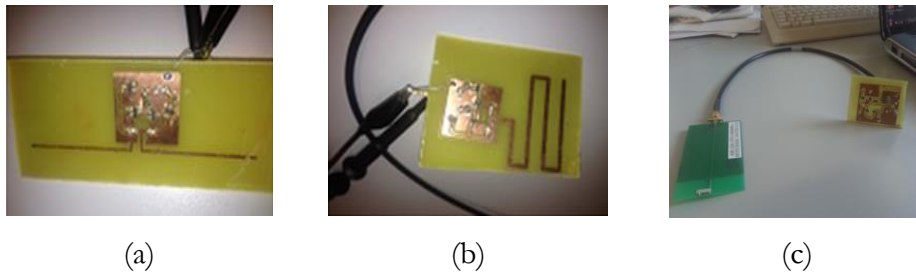


Fig. 2.17 (a) $\lambda/2$ Dipole antenna; (b) Monopole meander antenna; (c) Miniaturized antenna

The input RF signal has been transmitted by a commercial reader (Impinj Speedway Revolution) connected to a patch antenna [46] which sends a signal with 1W of power at 868MHz. Measurements have been carried out using a load resistance of $1M\Omega$. The best polarization has been chosen for each antenna. The measurements have been made at various distances between the antenna and the reader.

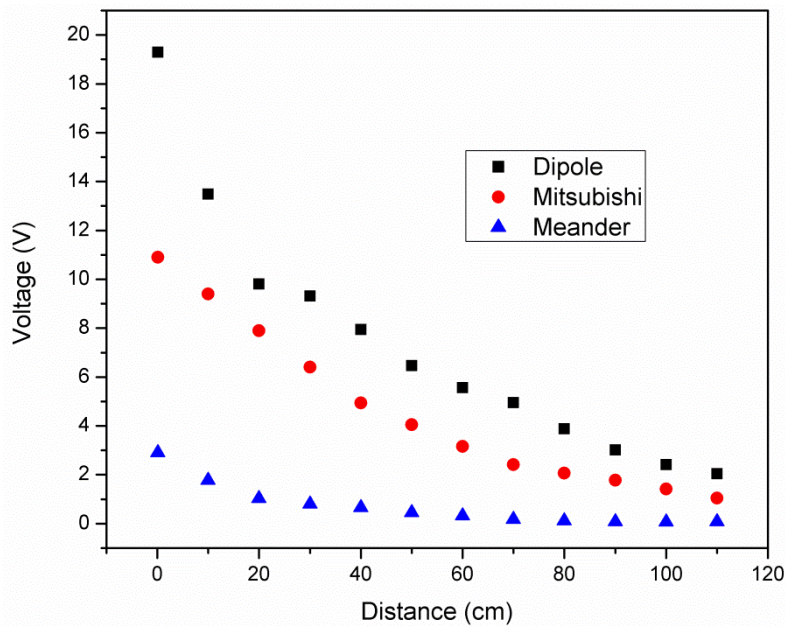


Fig. 2.18 Evaluation of antenna performances, considering the output voltage of a rectifier connected to the antenna's output

As depicted in Fig. 2.18, within the range of interest the maximum output voltage is obtained with the dipole antenna.

Furthermore, (only for dipole antenna) the power at the rectifier input at various distances from the reader has been estimated through a dedicated

integrated circuit (IC), namely the Linear Technology Power Detector LT5505 [47].

In this way, it is possible to estimate the RMS value of the input rectifier power in order to calculate the efficiency of the rectifier successively.

In Fig. 2.19, the input rectifier power at various distance from the reader is shown.

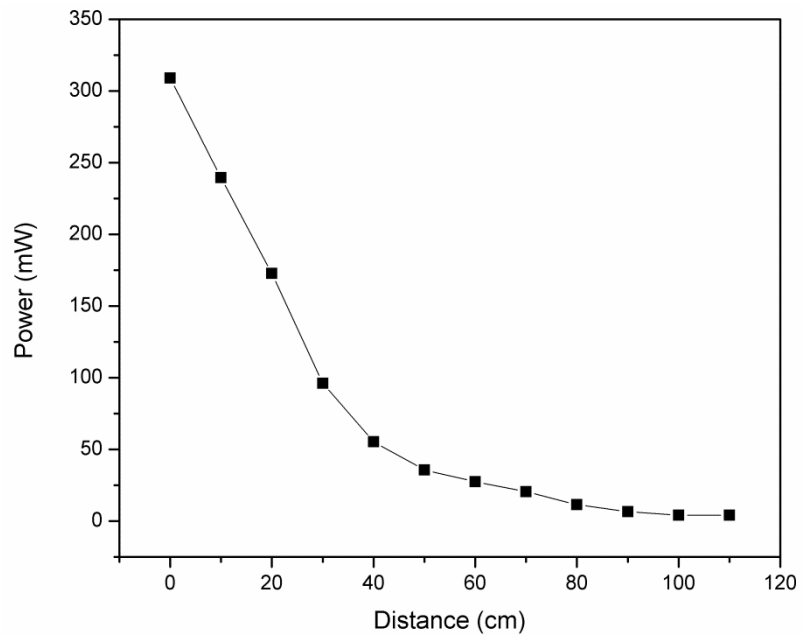


Fig. 2.19 Input power to rectifier, connected at dipole antenna, estimated through a dedicated power detector

2.5.2 Choice of diodes

Low input RF power is one of the fundamental issue of energy harvesting circuit. Generally, the peak voltage of the AC signal obtained from the antenna is much smaller than the diode threshold. For this reason, diodes with lowest possible turn on voltage are preferable. Moreover, since the energy harvesting circuit operates at high frequencies, diodes with a very fast switching time are also needed.

A good compromise is represented by Schottky diodes, that use a metal-semiconductor junction instead of a semiconductor-semiconductor junction. This allows the junction to operate much faster with a forward voltage drop as low as 0.15V.

The diodes efficiency is also affected by another critical parameter as the saturation current. Therefore, diodes with a high saturation current, low junction capacitance and low equivalent series resistance (ESR) should be used. Moreover, diodes with higher saturation current produce higher forward current. However, larger diodes usually have high saturation current with consequently higher junction and substrate capacitance that introduce increased power loss.

In this study, HSMS-2822 [48] and HSMS-2852 [49] Schottky diodes from Avago technologies have been used. The former has the turn on voltage of 340 mV while the latter is at 150 mV, measured at 1mA and 0.1 mA, respectively. Consequently, HSMS-2852 is suitable for low power design (LPD) used in a weak RF environment, while HSMS-2822 is preferred for high power design (HPD) in a strong RF environment.

2.5.3 Two stage Dickson Rectifier

In this work, the first version of the Dickson Rectifier has been realized using a dual stage. It is composed of HSMS2822 diodes and 6.8pF capacitances. The rectifier is connected to a $\lambda/2$ dipole antenna resonating at 868MHz. The whole system is mounted on a FR4 PCB substrate with a dielectric constant of $\epsilon_r=2.2$ and a dielectric thickness of 0.8 mm.

Furthermore, in order to estimate the performance of the rectifier, a commercial reader (Impinj Speedway Revolution) connected to a patch antenna that sends a signal with 1W of power at 868MHz has been used to generate the RF signal.

In addition, the rectifier has been simulated using the ADS software by Agilent. This software incorporates the parasitic parameters of the diodes into simulations.

The circuit has been simulated within a range of incident power from -10 dBm to 20dBm. The signal generator is a power source with an internal impedance of 73Ω to emulate the series resistance of the dipole antenna.

Alternatively, load resistances R_L of $1M\Omega$, $100k\Omega$, $10k\Omega$, $1k\Omega$ values have been used, both in simulations and in experimental characterizations.

In Fig. 2.20, the performances of the two stage Dickson rectifier are depicted.

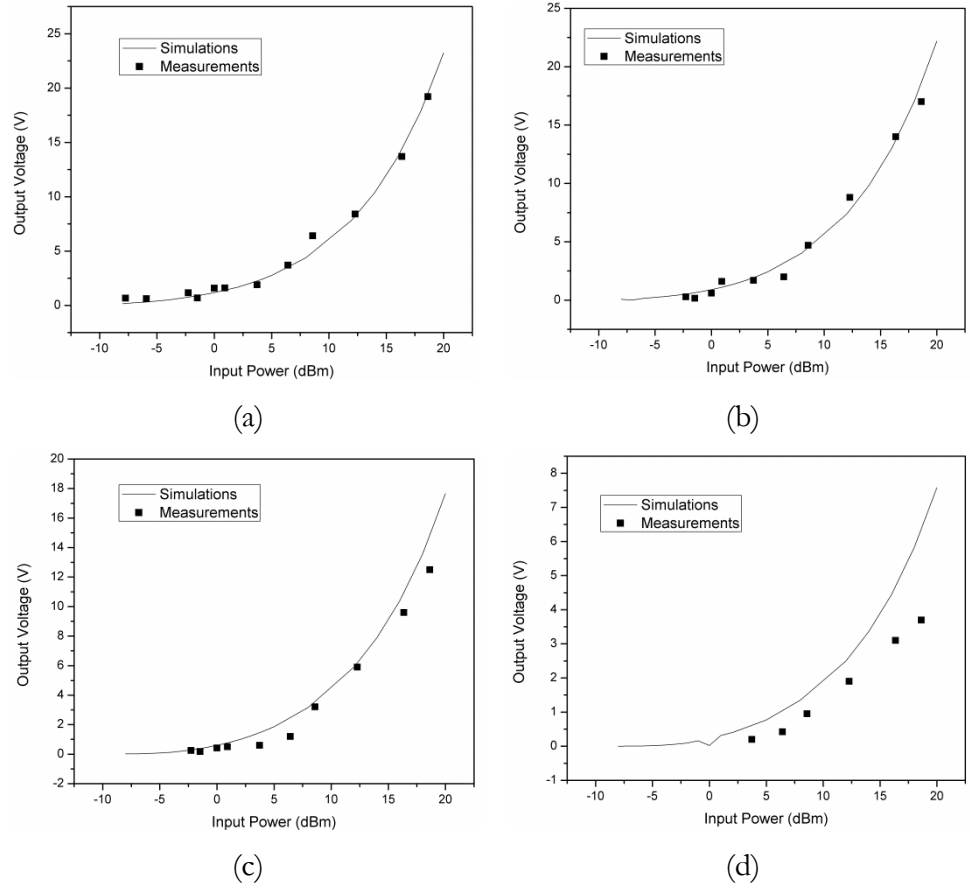


Fig. 2.20 Output voltage of dual the stage Dickson rectifier Vs Input power with $1\text{M}\Omega$ (a), $100\text{k}\Omega$ (b), $10\text{k}\Omega$ (c) and $1\text{k}\Omega$ (d) R_L

The rectified output voltage depends on the resistive load. Moreover, the sensitivity of the rectifier decreases with the reduction of the resistive load value. The sensitivity is defined as the minimum RF input power to power on diodes. The rectifier efficiency η_{rect} can be calculated as follows:

$$\eta_{rect} = \frac{P_{out}}{P_{in}} \quad (2.13)$$

where P_{in} and P_{out} are the input and the output power of the rectifier. The output power depends on the resistive load value and can be calculated as follows:

$$P_{out} = \frac{V_{out}^2}{R_L} \quad (2.14)$$

In Table 2.2 and Table 2.3 the measured and simulated efficiencies of the dual stage Dickson rectifier at various resistive loads and input power values, have been reported.

Table 2.2 Measured efficiency of the dual stage Dickson rectifier

P_{in}/R_L	1M Ω	100K Ω	10K Ω	1K Ω
8dBm	0.35%	2.50%	16%	26%
4dBm	0.23%	0.90%	12%	13%
0dBm	0.15%	0.70%	3.70%	_____
- 4dBm	0.10%	0.20%	0.30%	_____

Table 2.3 Simulated efficiency of the dual stage Dickson rectifier

P_{in}/R_L	1M Ω	100K Ω	10K Ω	1K Ω
8dBm	0.30%	2.50%	16%	30%
4dBm	0.20%	1%	10%	16%
0dBm	0.13%	0.80%	3.50%	2.25%
- 4dBm	0.10%	0.30%	0.50%	0.30%

2.5.4 Five stage Dickson Rectifier

The second version of Dickson Rectifier has been realized using a dual stage. It is composed of HSMS2852 diodes and 6.8pF capacitances. Also in this case, the system is mounted on a FR4 PCB substrate with a dielectric constant of $\epsilon_r=2.2$ and a dielectric thickness of 0.8 mm but the antenna has been omitted because the rectifier has been tested directly using a standard 50 Ω SMA connector. The RF signal has been injected directly, via a signal generator (Rohde & Schwarz signal generator SMA100A) that outputs a 868MHz continuous wave (CW) into the SMA connector. The power level of the signal generator has been iteratively changed in a range from -20dBm to 20dBm. Alternatively, load resistances R_{Load} of 1M Ω , 100k Ω and 10k Ω have been mounted.

In Fig. 2.21, the output voltage of a five stage Dickson rectifier is depicted.

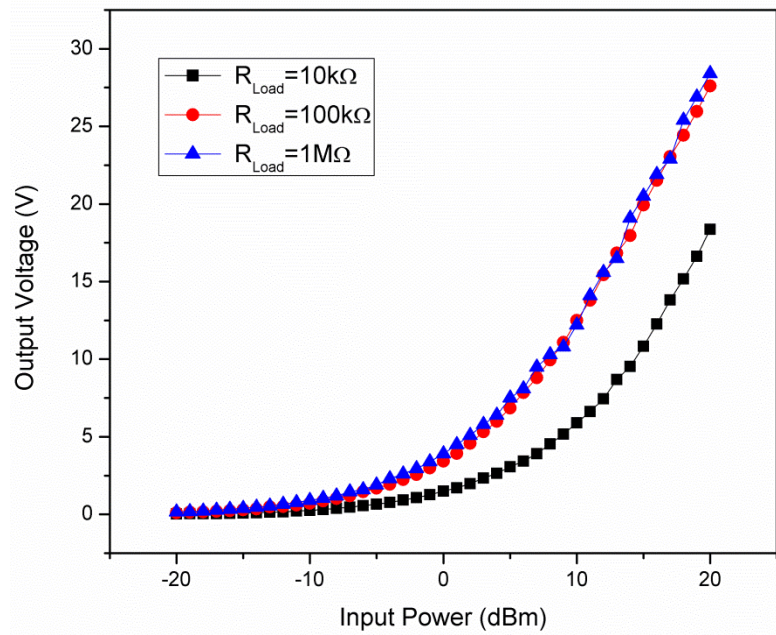


Fig. 2.21 Output voltage of the five stage Dickson rectifier Vs Input power

Also in this case, the rectified output voltage depends on the resistive load value. Moreover, the sensitivity of the rectifier decreases with the decrease of resistive load value.

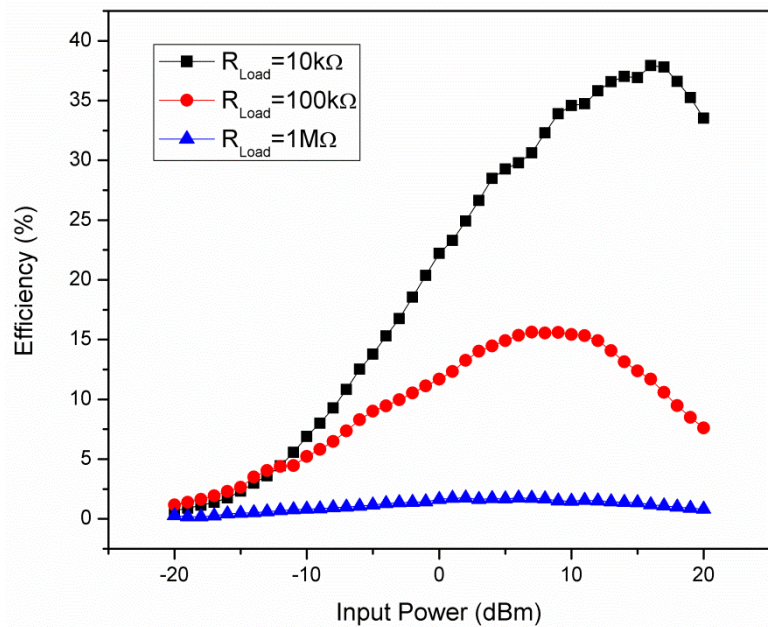


Fig. 2.22 Efficiency of the five stage Dickson rectifier Vs Input power

The efficiency of the rectifier has been calculated through the equation (2.13). In Fig. 2.22, the efficiency of the five stage Dickson rectifier is shown.

With a resistive load of $1\text{k}\Omega$, the circuit presents the higher peak of efficiency but for low input power (lower of 0dBm) the voltage output value of the rectifier is very low (lower of 1.8V). Indeed a minimum threshold of power supply of 1.8V must be guaranteed to supply an electronic circuitry placed at the output, for example a microcontroller. For this reason, for subsequent characterizations a resistive load of $100\text{k}\Omega$ has been used, in order to increase the sensitivity of the system.

2.6 Dynamic Impedance Matching

Since the energy harvesting circuit is made up of non-linear devices as diodes, the circuit itself exhibits non-linearity. This implies that the impedance of the energy harvesting circuit varies with the amount of power received by the antenna [50]. Since the maximum power transfer occurs when the impedance circuit Z_{Load} matches the RF input port, the matching network must follow the input impedance of the circuit that change as a function of input power and load, actually the electronic circuit.

In this study, a dynamic method to reduce the mismatch between Z_a and Z_{Load} for different input powers has been designed.

Assuming the impedance matching network simply made of an inductor and a capacitor connected in a LC topology, only the capacitor value is variable, using a fixed inductor.

A method that, using a finite number of discrete capacitors with different capacitance values, provides an enhanced power transfer in a finite number of input power stages. The control unit that supervises the capacitor switching drains for itself a power that is less than the power surplus obtained using the method.

2.6.1 Conceptual approach

A conceptual approach for a dynamic impedance matching is shown in Fig. 2.23. It comprises an independent control loop that transforms an input impedance Z_{Load} of the system into the desired matched impedance Z_a .

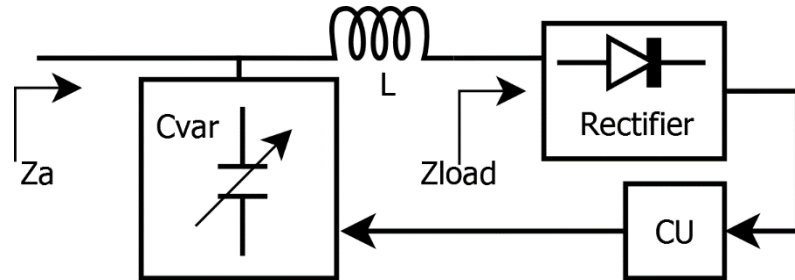


Fig. 2.23 Conceptual approach for dynamic impedance matching

The control of the dynamic impedance matching is assigned, in practice, to a Control Unit (CU) that runs an algorithm. This device estimates the input power of the circuit and then sets the capacitance with the best value in the impedance matching network. For the purpose of this work, we used four values of capacitance in the range 2.2 – 4.7pF that were mounted alternatively. As a further implementation of the system, the capacitors can be alternatively switched by means of a bank of integrated solid-state RF switches, controlled by the matching algorithm.

2.6.2 Algorithm

Self-Matching

At the beginning, the input power is not directly measured but it is estimated by reading the Dickson's output voltage. In fact, from the transfer characteristics of the rectifier it is possible to know the exact value of the input power of the system, and set accordingly the optimum capacitance from a set of discrete capacitor through an RF analog switch.

From measurements made on the Sensor Platform, shown in Fig. 2.24, the relation between the input power and rectifier output has been found.

We implemented equation (2.15) in the CU to calculate the input power. This equation is obtained by the polynomial regression of the inverse relation of Fig. 2.24.

$$P_{in} = 0.066V_{rect}^3 - 1.06V_{rect}^2 + 7.07V_{rect} - 14.83 \quad (2.15)$$

In Fig. 2.25, the fitting of equation (2.15) compared with the experimental measure is shown. The r-square coefficient of the fit curve is 0.994 in the assumed power range (-10 to +5 dBm).

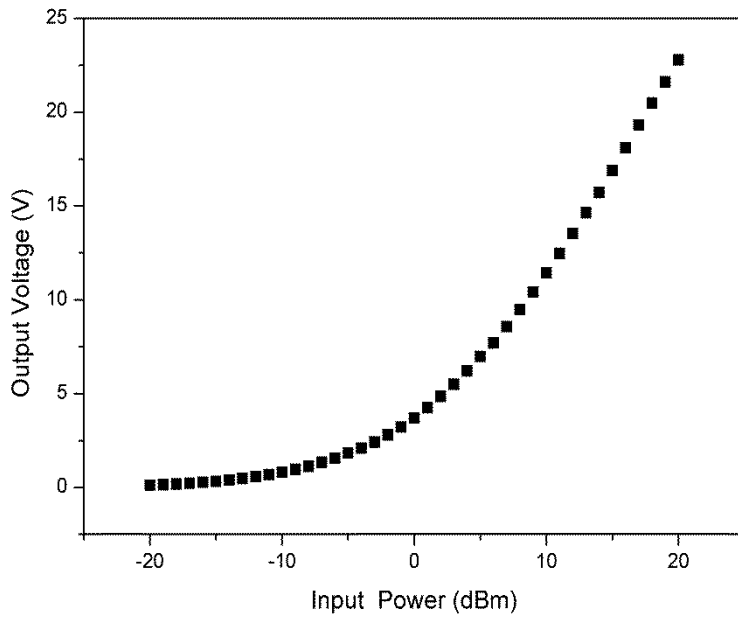


Fig. 2.24 Rectifier output voltage Vs Input power.

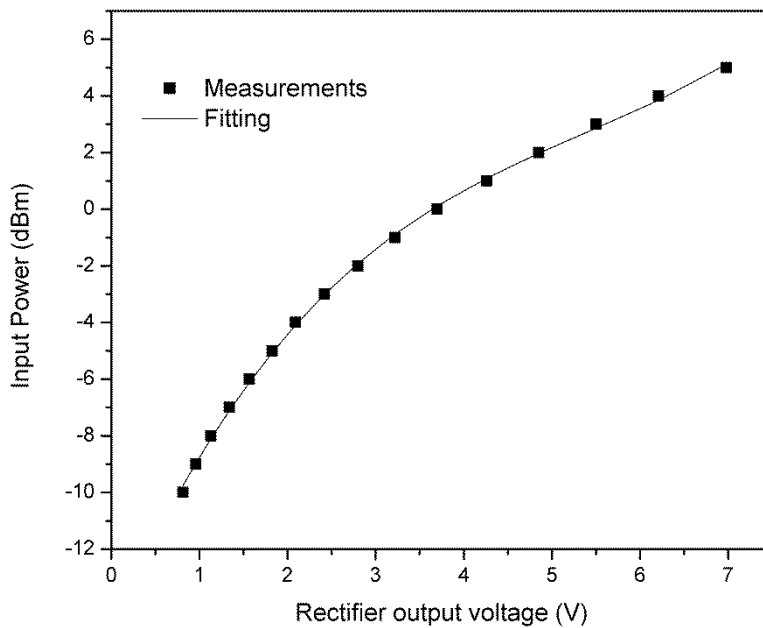


Fig. 2.25: Input power Vs Rectifier output voltage. The experimental data is compared with the fitting curve

P&O

Another approach requires the scan of the capacitor's bank through the RF analog switch, in order to identify the optimal value of capacitance for the impedance matching network at the actual incident power.

Assuming the relative distance from reader to tag fixed for a sufficiently long time, the CU compares the voltage values measured at the rectifier output, selecting the capacitor size that allows the maximum output voltage, which in turn gives the optimal power transfer.

2.6.3 Measurements

Measurements of the input impedance of the RF energy harvesting system have been made. The system has been tested directly using a standard 50 Ω SMA connector without special matching.

The experimental prototype (Fig. 2.26) has been fabricated on a FR4 substrate with a dielectric constant of $\epsilon_r=2.2$ and a dielectric thickness of 0.8 mm, using off-the-shelf discrete components.

A 5-stage Dickson rectifier and a fixed resistive load of 100k Ω have been used.

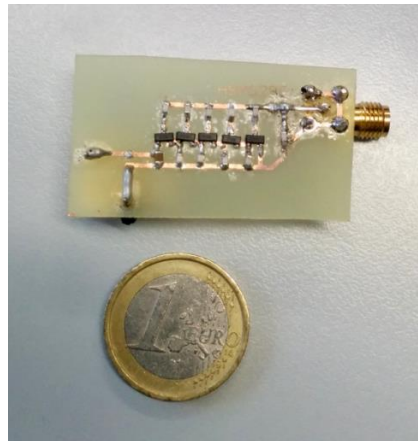


Fig. 2.26 Experimental prototype

Using an Agilent E5071C Network Analyzer calibrated at 868MHz the input impedance at various power levels has been measured, obtaining the results shown in Fig. 2.27. In the calibration phase, also the SMA connector has been taken into account in order to provide accurate results that deals only with the contribution of the electronic circuit.

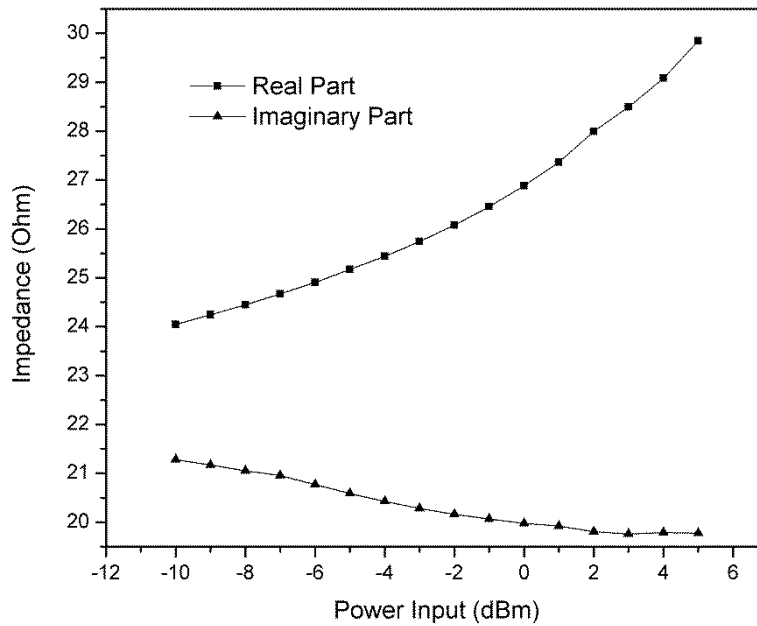


Fig. 2.27 Real and Imaginary part of input impedance of the RF energy harvesting circuit at 868MHz

2.7 Power Management and Digital Section

Since the power harvested by RFID tags is extremely limited, a careful component selection must be made to minimize the current consumption. Recent advances in Xtreme Low Power (XLP) IC manufacturing allow discrete components with less than $1\mu\text{A}$ of current consumption and operation at 1.8V, thus it is now possible to construct working, wirelessly powered RFID tags with discrete components.

2.7.1 Voltage Regulator

Generally, electronic circuits, require a stable power supply voltage value. A constant value of this voltage must be guaranteed also for the load resistance variations.

In energy harvesting circuits, the rectified DC output voltage varies with the load, thus must be fixed at a proper value to supply energy to an electronic circuit (load). For this reason, a fixed output voltage regulator has been added on the platform. In this work, an LDO (Linear Technology

LT3007 [51]) has been employed to regulate and stabilize the rectified DC output voltage. The output voltage of the LT3007 is fixed to 1.8V, with a current consumption of about 1.0 μ A.

2.7.2 Microcontroller

The general purpose computation capabilities of the Sensor Platform are provided by an XLP power microcontroller.

PIC 16LF1503 from Microchip Technology INC [52] fulfills the power and computational requirements of this work thus has been chosen for the platform.

The 14-Pin 8-Bit Microcontroller features a power consumption of few hundred of nA in standby mode, and an operating current of 30 μ A/MHz @ 1.8V.

The MCU can work with a calibrated 16 MHz Internal Oscillator (software selectable frequency range from 16 MHz to 31 kHz), or a 31 kHz Low-Power Internal Oscillator.

An Analog-to-Digital Converter with 10-bit resolution and internal Fixed Voltage References is integrated and has been used for analog measurement acquisition.

In addition, the MCU can communicate with other devices through a digital serial interface (either SPI or I2C).

In the platform, the role of the MCU is to interface other system blocks with the peripherals and to supervise all the operations of the circuit, allowing a duty-cycled functioning.

To the MCU is assigned the control of the dynamic impedance matching routine for the efficiency optimization of the power harvester.

Using the Serial Peripheral Interface (SPI) the microcontroller access the EEPROM memory of the tag for read and write operations. Measurements and data can also be accessed further with a standard EPCglobal Class-1 Gen2 reader directly from the User Memory of the tag.

The firmware implemented into the MCU is able to perform a dynamic adjustment of the time interval between two readings, allowing to control the average power budget of the system.

2.7.3 RFID Front End

An RFID tag, EM4325 [53] from EM Microelectronics (SWATCH group) EPCglobal Class-1 Gen2, was added to the platform to ensure an RF data transmission standard protocol. The IC also supports SPI communication for read/write operations from the microcontroller.

The supply system of the platform powers up the microcontroller and the tag only when data are transferred from the microcontroller to the tag through the SPI Bus. Otherwise, the tag is passively powered by the RFID reader to ensure the data acquisition from a host system.

The EM4325 RFID chip has 3072 bits of user programmable memory, divided into 48 pages of 64 bits each. A further feature of this IC is a temperature sensor embedded on the same die that can be accessed using the SPI protocol, thus allowing the reduction of cost and space on the board for extra components. The integrated temperature sensor supports the temperature range from -40°C to $+60^{\circ}\text{C}$.

In this study, a bidirectional communication channel for remote sensing application has been created using the EM4325 connected to the MCU.

The R/W user memory of the tag can be accessed both from reader and microcontroller to read/write measurement data and to read/write configuration parameters. Furthermore, the updated parameters can be read by the microcontroller to dynamically adjust the time intervals between sensor readings in order to modify the system power budget according to new application conditions. However, hardware improvements have been also investigated to enhance both the energy transfer efficiency and the power consumption during the sensing activities.

2.8 Platform Performance Evaluation

The experimental prototype has been fabricated on a FR4 substrate PCB, using off-the-shelf discrete components and a printed, 17.34cm long, dipole antenna.

Further measurements have been carried out substituting the dipole antenna with a SMA connector and providing an RF signal directly with a Rohde-Schwarz RF signal generator SMA100A, able to generate signals in the range 9kHz – 6GHz with an output power up to 30dbm.

2.8.1 *Dynamic Impedance Matching Evaluation*

To evaluate the performances of the DyIMN method the prototype in Fig. 2.28 has been used. In this case, an SMA connector has been used as input port of the RF signal. The connector is followed by an LC impedance matching network. The inductor is placed in series between the input and the rectifying section while the capacitor is in parallel.

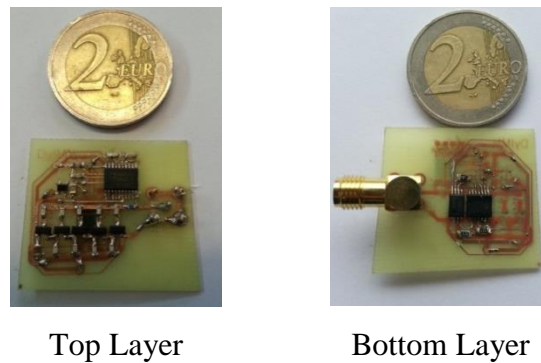


Fig. 2.28 A snapshot of the prototype connected with a SMA connector

According to the measured input impedance, optimal values for the conjugate impedance matching ($L=1\text{nH}$, $C=3.3\text{pF}$) have been calculated to get the 50Ω target impedance (1dBm of Input power). Afterward, considering three sub-ranges of the Impedance Vs Input power characteristic, the best matching capacitors, one for each specific sub-range, have been calculated from the Smith Chart, assuming a fixed value for the series inductor ($L=1\text{nH}$).

Measurements have been carried out with a variable input power, generated with a SMA100A signal generator connected to the system directly to the 50Ω SMA connector. All of the three capacitors were scanned at each input level to look for the best matching.

In Fig. 2.29, the conversion efficiency measured using a static complex conjugated method for the impedance matching and without impedance

matching is shown. In the same figure, the best results obtained by properly switching the capacitor's bank at each power are shown for the DyIMN method. The improvement in efficiency for the input power range from -6 to 1dBm, with a maximum of +12% at -2dBm, is shown.

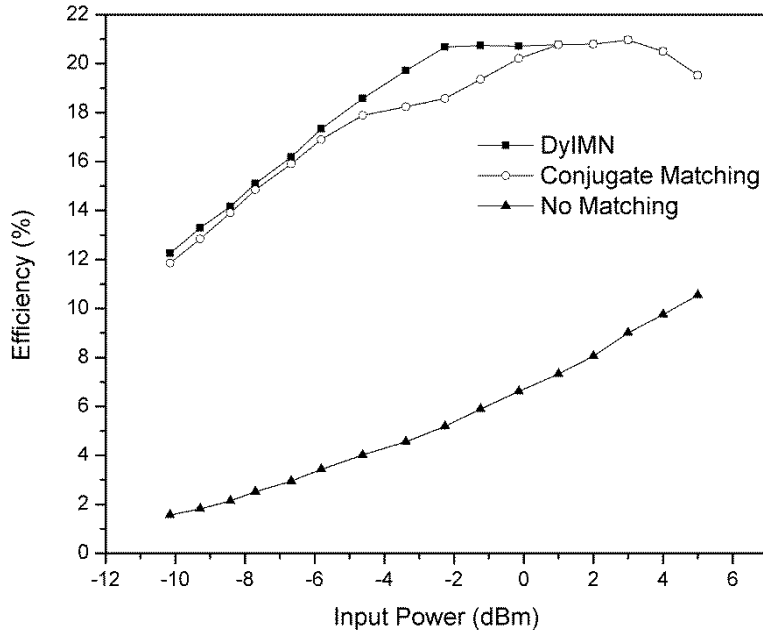


Fig. 2.29 Energy harvesting efficiency of the realized prototype Vs Input Power. The dynamic matching strategy adopted in this study is compared to the static matching and to no matching options, tested on the same circuit

2.8.2 Power Budget

One of the significant challenges of incorporating microcontrollers, sensors, and peripherals into passive RFID technology is the ability to manage the large power consumption of these devices. Indeed the harvester cannot continuously supply power to the Sensor Platform during a single reader query. For this reason, a large capacitor has been added to accumulate energy between multiple EPC queries.

In addition, the firmware of MCU has been implemented to manage the average power consumption, optimizing duty-cycle D that can be calculated as follow:

$$D = \frac{T_{run}}{T_{run} + T_{sleep}} \quad (2.16)$$

Table 2.4 summarizes the power consumption of the platform in the different states of activation of the MCU, together with the minimum duration of each state. The microcontroller self-adjusts the durations enabling the dynamic reduction of the power budget of the system, e.g. increasing the sleep phase duration for slowly varying sensing activities.

Table 2.4 Sensor platform power consumption under the three operation states

	Duration[ms]	Power[uW]
Sleep	≥ 0	0.48
Idle	≥ 1	4.2
Run	≥ 4	360

2.9 Applications

An UHF Impinj Reader has been used in the setup to transmit the RF signal. The model R420 lets establish a standard EPCglobal Class-1 Gen2 communication with the tag, allowing at the same time to supply the RF power to the circuit and to read data. The Impinj software was used to access the user memory of the tag for reading and exporting measurements data and for online parameter updates. The prototype used for this test is depicted in Fig. 2.30.

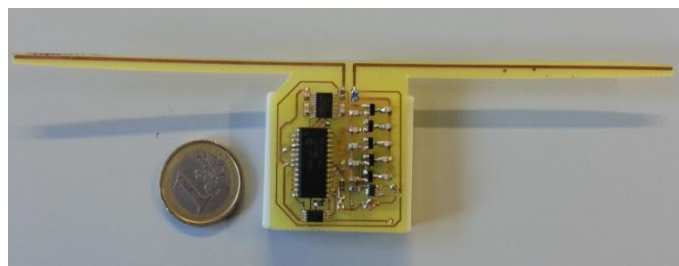


Fig. 2.30 A snapshot of the prototype connected with dipole antenna.

2.9.1 Wireless temperature sensor

As a proof of concept, the platform has been used to perform indoor temperature measurements. The set-up used comprises an UHF Impinji

Reader that acts both as RF power source and receiver of the measured data. Furthermore, a commercial temperature sensor has been used for reference (Magiant Serverflu USB temperature sensor)[54]. The measurements have been carried out in a 24-hour session, placing the platform in a standard office room where an air conditioner was used to modify the temperature. The two sensors performed the monitor of the indoor temperature over the course of a day. A reader antenna was used to interrogate the platform and to collect the sensor data at the host PC.

Results of the measurements are depicted in Fig. 2.31, showing how the performed sensor measurements performed are consistent with the events occurring over a 24-hour observation period and with the measurements of the reference sensor used.

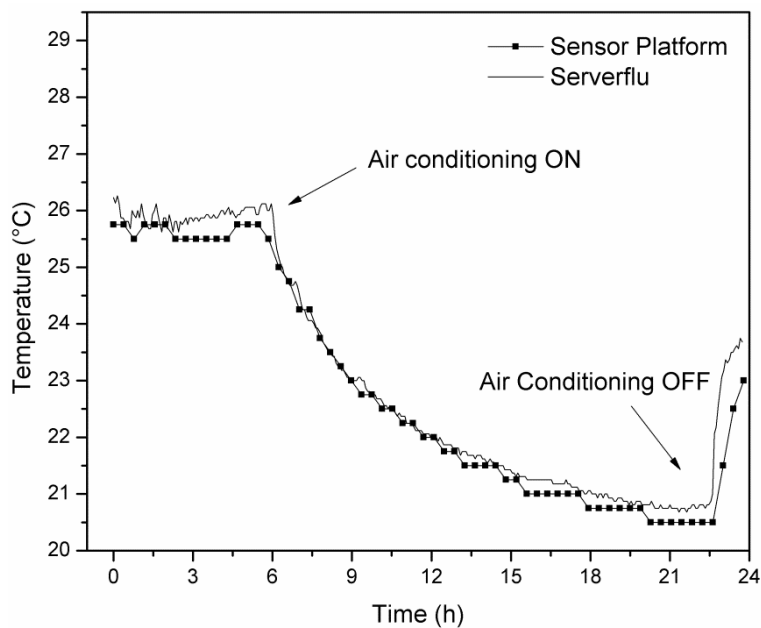


Fig. 2.31 24-hour temperature monitoring performed in an indoor environment

2.9.2 Performance for Long-run Sensing Applications and Wireless Sensors Networks

An efficient energy transfer is of high interest for a reduced recharging time of the embedded capacitor. This represents a fundamental step to enlarge the range of applications usually limited to classic wireless sensor networks, such as data logging or environmental sensing in large spaces.

Challenges related to energy replenishment and data collection should be taken into account to enable an effective deployment of large networks. In particular, the number of mobile readers moving within a sensing network to gather data and transfer energy has been investigated, such that all nodes are kept alive and all data are collected.

In this application, a large RSN (RFID Sensor Network) where N sensor tags are distributed over a two-dimensional region. Assuming that the sensor devices are homogeneous in terms of hardware and sensing activity, and they can be equipped with memory banks that are large enough to contain and process all their sampling records. Each sensor tag should be visited by a mobile reader before running out of the energy stored in its capacitor. To guarantee perpetual network operations, one or multiple mobile readers are deployed to recharge the sensor tags and gather their sensing data. Assuming that the mobile readers stop close enough to each tag (i.e., an average distance of 0.5m) for a time interval sufficient to fully recharge the node and to gather the sensed data (this latter time is usually much smaller than the former). Therefore, the energy requirements of each single device must be defined and then a strategy to determine the number of required mobile readers and to plan their movement tours is proposed.

Energy storage

The amount of energy harvested by the sensor platform from reader RF field can be modeled by considering a modified version of the Friis' free space propagation model as expressed in equation (2.6). Once the received power P_a is determined, the time T_{charge} to fully recharge the capacitor of a sensor tag can be computed with equation:

$$E_{stored} = \frac{1}{2}C(V_{charged}^2 - V_{dd}^2) = P_r T_{charge} \quad (2.17)$$

where, C is the capacitance value of storage element, $V_{charged}$ and V_{dd} are respectively the maximum voltage for the embedded capacitor and the minimum operating voltage of the sensor platform.

Another key factor to analyze is the lifetime T_{Life} of a sensor platform, i.e., the time interval for a device to run out of the energy stored in its capacitor. The lifetime T_{Life} can be estimated as:

$$T_{Life} = \frac{E_{stored}}{P_{run} \cdot D + P_{sleep} \cdot (1 - D)} \quad (2.18)$$

where P_{run} and P_{sleep} are the power consumptions respectively in active and sleep mode.

Reader Deployment Strategy

In order to determine the minimum number of required mobile readers, the cost (in terms of time) of the tour visiting all sensor tags is a required parameter. Finding the shortest length tour is a well-known NP-hard problem, the so-called Traveling Salesman Problem (TSP). The resolution of the resulting TSP problem can be obtained implementing a genetic algorithm [55]. The time to complete a single tour is given by the sum of two contributions: (i) the travel time T_T , and (ii) the time required to recharge all nodes T_R . The first term is given by the tour length L_T divided by the mobile reader movement speed v , which is assumed equal for all readers: $T_T = L_T/v$. The second term T_R can be computed accounting for the time needed to fully recharge a single node T_{charge} defined in the previous section, and the number N of nodes deployed in the scenario: $T_R = T_{charge} \cdot N$.

In large RSNs the time of a single tour could become too high to meet the recharging requirements of all RFID sensor tags. Accounting for the energy constraints of the tag, we identify the maximum time interval T_{Visit} between two consecutive visits of a reader as the sum of T_{Life} and T_{charge} . If multiple mobile readers are required, then they shall move along the same tour, but with different timings. Based on this strategy, the minimum number of required mobile readers R can be determined as follows:

$$R \geq \frac{T_T + T_R}{T_{Visit}} \quad (2.19)$$

In Fig. 2.32 a sample scenario of this solution is depicted.

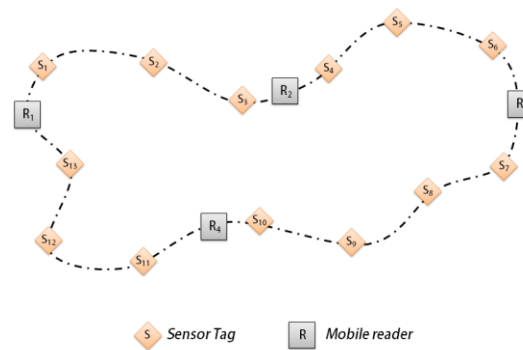


Fig. 2.32 A sample scenario of the network model

Performance evaluation

In this study, the performances of the proposed tag comparing it to the performance of the WISP 4.1DL tag [25] in long-run application scenarios have been evaluated. The first merit figure is the harvested power, as this has an important impact on estimating the recharging time of the sensing tag. In Fig. 2.33, the experimental values varying the distance between the reader's antenna and the tag between 0.2m and 1.5m have been plotted. The plotted results refer to a tag being powered by an UHF Impinj reader, whose parameters are reported in Table 2.5.

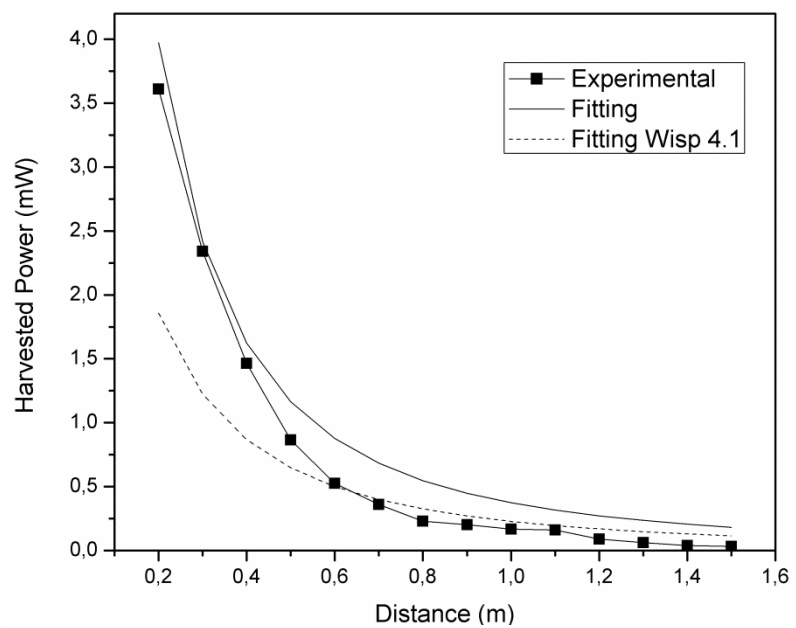


Fig. 2.33 Harvested power varying the distance between the reader's antenna and the tag

In this case, a value of 0.23 for the factor η that takes into account the rectifier efficiency in (2.6) has been obtained. This value has been achieved by the curve fitting of the measured value of output power. To assess the performance of the considered tag for the network model described previously, a simulative analysis has been conducted by using the Matlab tool. Main simulation parameters and settings are listed in Table 2.5.

Table 2.5 Main parameters used in simulation

	Parameter	Value
Mobile reader	Transmission Power	1W
	Movement Speed	0.5 m/s
	Recharging distance to tag	0.5 m
	Source antenna gain	5.5 dBi
	Frequency	868 MHz
Sensor tag	Rectifier efficiency η	0.23
	Parameter for Friis' free space equation at short distance β	0.154
	Reception antenna gain	2 dBi
	Polarization loss	3 dB
	Capacitor	1 mF
	Minimum operating voltage	1.8 V
	Maximum voltage recharger	5.5 V
	Power in active mode	360 μ W
	Power in sleep mode	0.5 μ W
	Time in active mode	13 ms
Simulation settings	Simulated area	250 x 250 m
	Node distribution	Random
	Number of tags	[50 – 300]
	Information sampling period \mathcal{S}	[1-30] s

A variable number of sensors N in the range [50-300] has been considered, randomly deployed in a square area of 250m x 250m. A sparse network has been assumed (i.e., the minimum distance between each pair of

nodes is more than 10m) such that mobile reader may visit only a node at a time. In Fig. 2.34 the number of required readers has been reported, considering different scenarios where the sensing period S varies in the range [1-30]s. The reduced recharging time and the lower consuming power both in active and sleep mode of the sensor platform allow for a reduced number of mobile readers in all tested sensing period value S .

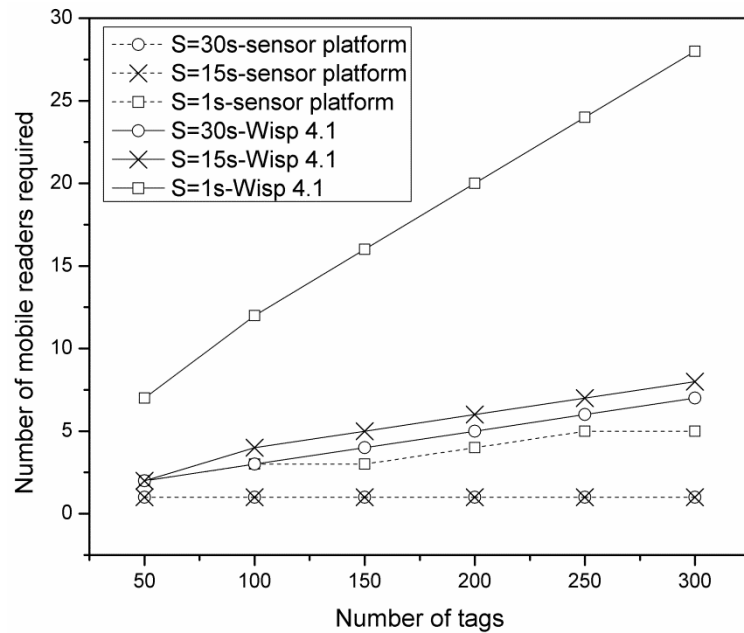


Fig. 2.34 Number of required readers

2.9.3 13.56MHz Platform

According to the architecture of the UHF sensor platform presented in Fig. 2.6, also an HF version has been realized.

The 13.56MHz platform has ISO/IEC 7810 ID-1 card size (85.60×53.98 mm) and is shown in Fig. 2.35. It also includes two antennas. The biggest antenna is used for energy harvesting and is connected to the rectifier/regulator components. The smallest antenna is used for RF data transmission and it is connected to the RF chip tag.

The system has been realized on a flexible 0.4mm FR4 substrate. The RFID tag IC is an M24LR64-R [56] that is a 13.56 MHz NFC/RFID tag with a dual-interface EEPROM. A single stage Dickson rectifier has been implemented. The microcontroller is the same already described on the previous paragraphs.

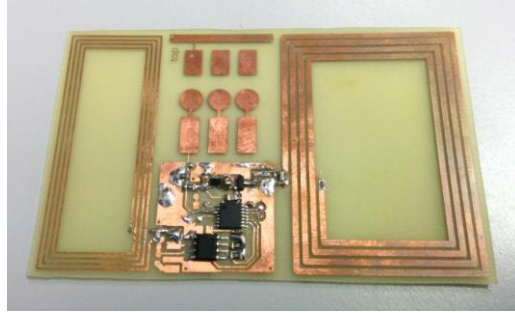


Fig. 2.35 Picture of the 13.56 MHz platform prototype

The M24LR64-R is a 13.56 MHz NFC/RFID tag IC with a dual-interface 64-Kbit EEPROM and a 64-bit block that is used to store a unique identifier (UID). It features an I2C interface and can be operated from a V_{dd} power supply. It is also a contactless memory powered by the received carrier electromagnetic wave. The M24LR64-R follows the ISO 15693 and ISO 18000-3 mode 1 recommendation for radio-frequency power and signal interface.

When the M24LR64-R operates in the RF mode, it is powered by the RFID reader. No battery is then required to access it whether in write or read mode. With its external inductive antenna, the chip draws all of its operating power from the reader's electromagnetic field. The RFID reader plays the same role of the primary of a voltage transformer that powers the secondary (in this case, the inductive antenna). The energy transfer ratio from the reader to the tag chip is similar to the coupling factor of a voltage transformer, and it is function of: the antenna tuning; the distance between the reader and the board; the reader power and dimensions antenna; the M24LR64-R antenna dimension and orientation with regards to the reader antenna.

The amount of energy powering the device is related to the orientation of the board antenna with regards to the RFID reader antenna. The best configuration is obtained when both antennas are parallel and face each other. The read range can drop to zero when the antennas are perpendicular to each other.

The smallest antenna inductance ($L_{antenna}$) designed on the PCB board match the M24LR64-R internal tuning capacitance ($C_{tuning} = 27.5$ pF)

in order to create a circuit resonating at 13.56 MHz. The basic equation of the tuning frequency is:

$$f_{tuning} = \frac{1}{2\pi\sqrt{L_{antenna} \times C_{tuning}}} \quad (2.20)$$

A 13.56 MHz antenna can be designed with different shapes; the square antenna has been chosen for the platform, as depicted in Fig. 2.36.

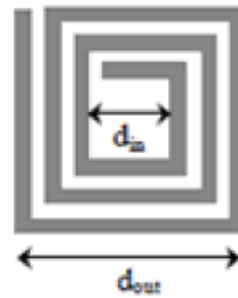


Fig. 2.36 Square coil antenna

The inductance of a such antenna can be calculated with the following equation:

$$L_{antenna} = K1 \times \mu_0 \times N^2 \times \frac{d}{1 + K2 \cdot p} \quad (2.21)$$

where:

- $d = (d_{out} + d_{in})/2$ in millimetres;
- $p = (d_{out} - d_{in}) / (d_{out} + d_{in})$ in millimetres;
- $K1 = 2.34$ and $K2 = 2.75$;
- μ_0 is the vacuum permeability;

The impedance of the realized antenna has been calculated thought a simplified software tool provided by ST Microelectronics.

The smallest antenna on the PCB has been designed to have $L=1.1 \mu\text{H}$, whereas the biggest one have a design value of inductance of $L=1.16 \mu\text{H}$.

The two antennas have been characterized using an impedance analyser Agilent 4395.

Fig. 2.37 shows the impedance of the smallest antenna (tag antenna) as a function of the frequency. It is possible to observe that the antenna inductance match the project value. The resonance frequency is about 100

MHz and it necessary to use an equivalent total capacitance of about 100 pF in order to create a circuit resonating at about 13.56 MHz (Fig. 2.38).

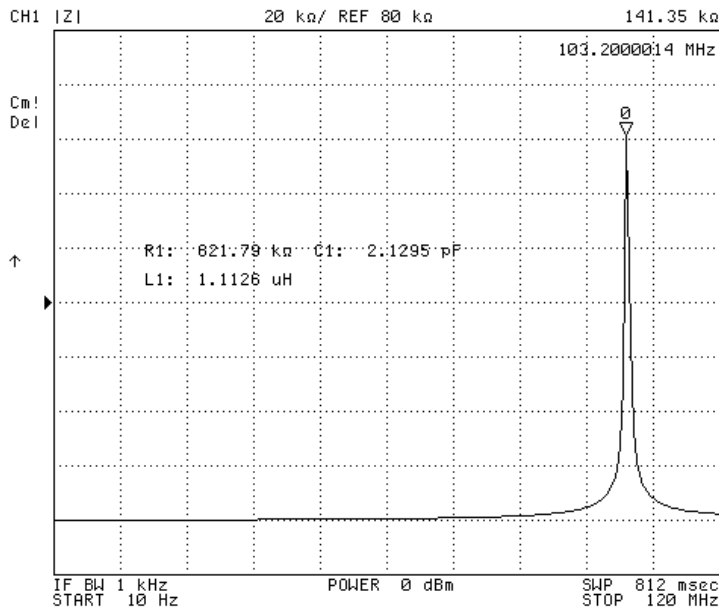


Fig. 2.37 Impedance of the smallest antenna on the PCB board

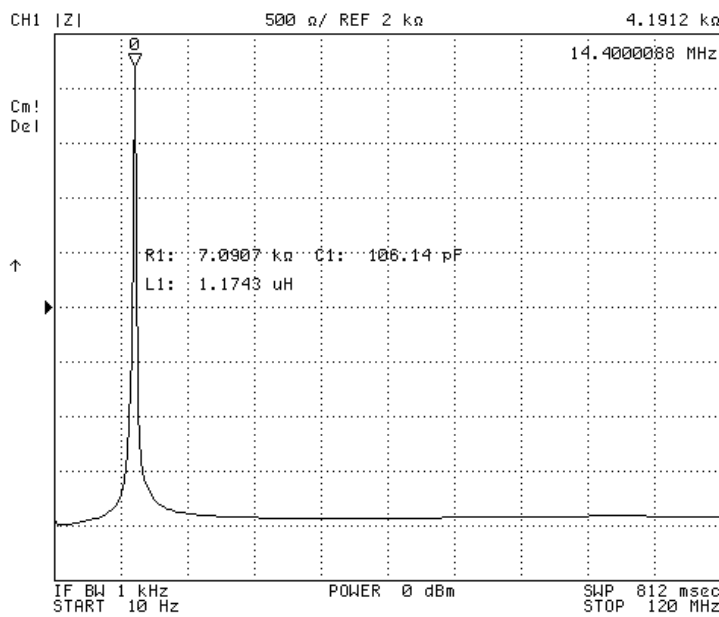


Fig. 2.38 Impedance of the smallest antenna on the PCB board with matching capacitor

Fig. 2.39 shows the impedance of the biggest antenna (harvesting antenna) as a function of the frequency. It is possible to observe that the antenna inductance matches the design specifications and the resonance

frequency is about 100 MHz. It necessary to use an equivalent capacitance of about 100 pF in order to create a circuit resonating at about 13.56 MHz (Fig. 2.40).

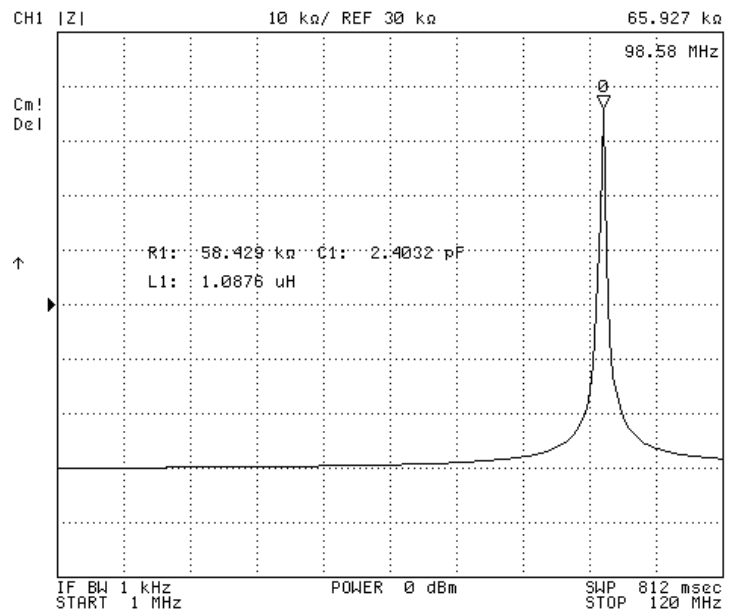


Fig. 2.39 Impedance of the biggest antenna on the PCB board

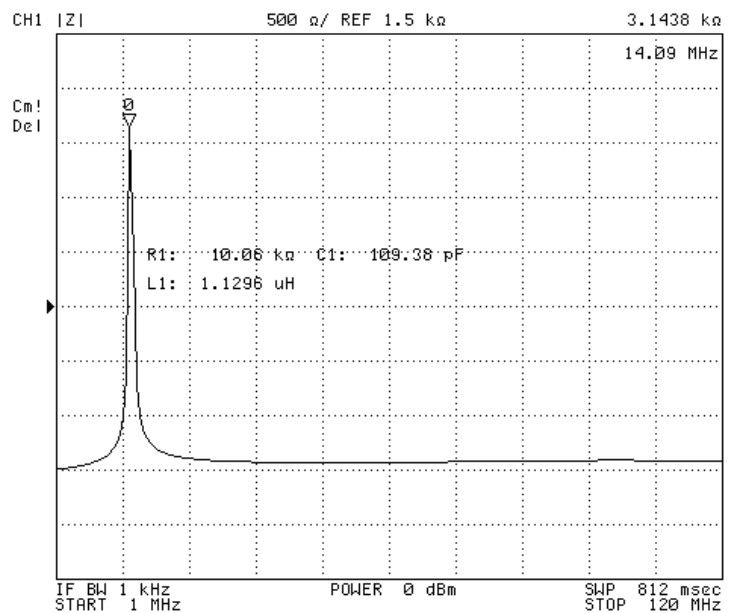


Fig. 2.40 Impedance of the biggest antenna on the PCB board with matching capacitor

Trough experimental measurements, the proposed 13.56MHz sensor platform has been detected at a maximum distance of 20 cm at the standard ISO 15693 reader.

2.10 Remarks

In this chapter, the wireless Sensor Platform realized on an FR4 substrate has been presented.

An improvement in efficiency for input powers above -7dBm, with a maximum gain of +12% at -2dBm has been obtained using the strategy of the DyIMN based on a switched capacitors routine governed by the MCU.

The firmware also performs a dynamic adjustment of the time intervals between two readings, allowing to control the average power budget of the system.

The platform has been used to perform temperature measurements over a 24-hour observation period in an indoor environment to demonstrate the feasibility of the platform in a typical application scenario.

Furthermore, the feasibility of using the sensor platform for long-run applications has been evaluated. Based on the sensor platform features, a network model where one or multiple readers travel across the network to recharge the devices and gather their sensed data has been proposed. The proposed solution based on the presented sensor platform has then been validated by comparing the results with respect to state-of-art devices via both experimental and simulation results. The results showed the important improvements that can be obtained.

In addition, a sensor platform working at 13.56MHz has been realized, featuring communication with a HF standard reader at a maximum distance of 20cm.

3 CMOS Wireless Sensors ICs

In this chapter a new advanced wireless sensor in 0.35 μ m CMOS technology, specifically designed for the monitoring of High concentration photovoltaics (HCPV) modules, is presented. The microchip was designed to be placed aside each solar cell in a module, to monitor its temperature and illumination state. In particular, the temperature sensor is based on the temperature dependence of the bipolar transistors characteristics available in CMOS technology, while the illumination sensor is designed as a simple photodiode that consists of a p-n junction. An integrated 2.4 GHz transmitter with an On-Chip-Antenna (OCA) - made on the top metal layer of the same die - sends the collected data wirelessly to a base station allowing a complete diagnostic of the module performances over the years. On-Off Keying (OOK) modulation is used to send the sensors data.

3.1 Introduction

The developed sensors platform, described in chapter 2, is based on a RFID technology and realized with commercial off-the-self discrete components.

The convenience of these systems is the absence of a power sources and consequently absence of maintenance. Moreover, the systems present an optimal versatility with a high precision.

However, it is possible to identify several limitations. For example, the dimensions make the circuit a macroscopic object (few square centimeters), or the need to be interrogated to trigger the transmission of sensor

information, for the reason that the energy necessary for the operation is collected from the electromagnetic field produced by the reader. Furthermore, using discrete components, the cost of the finished product is increased and welding and machining of the PCB are required. To overcome these issues, we tried to achieve a compact, economical and sufficiently accurate system as a fully integrated system in CMOS technology.

The objective is to attain a wireless sensor that integrates the transducer, the oscillator and the circuitry needed to operate it, all within the same chip.

Specifically the system has been designed for the monitoring of High concentration photovoltaics (HCPV) cells. The microchip can be placed aside each solar cell in a module, to monitor its temperature and illumination state, powered by the cell itself.

The proposed approach is useful for the online control of the efficiency of solar cells in harsh environments and even for the evaluation of parameter degradation of the cells due to harmful influences.

3.2 HCPV Monitoring

High concentration photovoltaics (HCPV) is a well know technology which presents several advantages compared to standard photovoltaics. In particular, HCPV allows the use of the necessary semiconductor area to be cut dramatically. Consequently, this is a fine outcome in the case of high efficiency solar cells made of expensive band gap tailored, binary or ternary semiconductors for example, or based on complex stacked multi-cells designed to optimize the use of the solar spectrum.

In HCPV systems, small solar cells, sometimes just a few square millimeters in area, are required to convert a solar radiation into electricity that could be as strong as thousands of suns, depending on the concentration degree offered by the optical system.

Needless to say, HCPV cells have to withstand working conditions that are often close to their absolute maximum ratings, especially in terms of temperature and current density.

In addition, the system efficiency might be highly dependent on mechanical issues, affecting for example the optical alignment between cells and concentrators.

As a result, a constant monitoring of the cell key parameters might help prolong their life and optimize the conversion efficiency, with valuable economical returns.

Automatic data acquisition systems are currently used for both monitoring of the system performances and control of its operation. The information obtained can be used to evaluate efficiency during long periods and to optimize future systems in terms of performance and reliability. In [57] and [58] a virtual instrumentation has been used to measure a wide variety of signals with a good accuracy. Nevertheless, the data transfer is carried out using a data acquisition board and does not utilize wireless communication.

A wireless solutions has been proposed by [59] and [60]. [59] realizes a computer-based wireless data acquisition system for monitoring meteorological data. The sensors data are processed by a microcontroller and interfaced to a PC using a wireless unit. A system allowing for a single panel monitoring is proposed in [60]. In addition, the circuit is equipped with a suitable energy harvesting supply stage relying on supercapacitors, which makes the whole system self-powered.

In this study, we present a full custom microchip, including several sensors, specifically designed to monitor HCPV cells. The microchip was designed to be placed aside each solar cell in a module, to monitor its temperature and irradiation state.

3.2.1 System architecture

The proposed system provides a sensing circuit and a transmission section which allows for transmitting OOK modulated sensing information. This is achieved through an integrated dipole antenna which is found directly on the sensor chip surface. The architecture of the proposed microchip is

shown in Fig. 3.1. The system includes an analog section, formed by a “proportional to absolute temperature” (PTAT) sensor which guarantees an optimal linearity, and a irradiation sensor realized with and integrated solar cell. Analog sensors output has to be converted to digital data for further processing and wireless transmission. For this reason a digital section has been implemented and a PISO register has been designed to serialized this signals. The output of this section is used to modulate an LC oscillator that transmits the information through a dipole OCA.

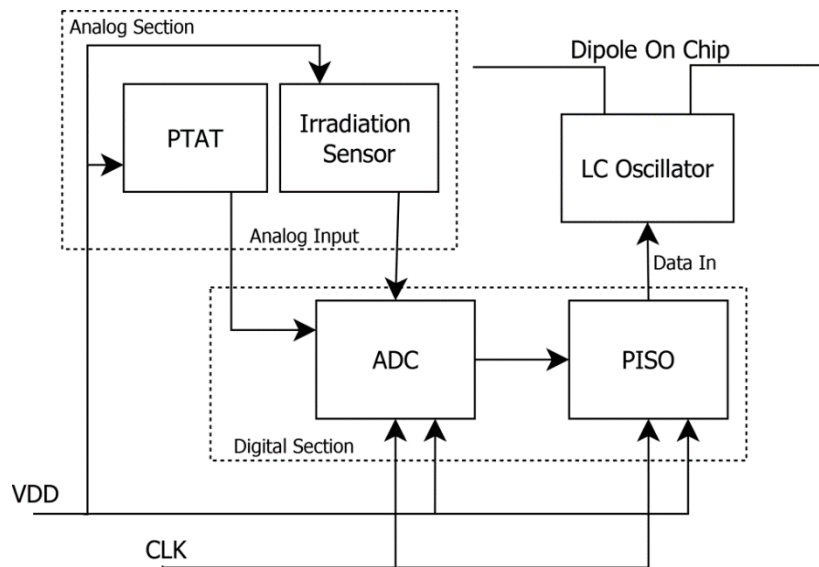


Fig. 3.1 Wireless HCPV sensor architecture

3.3 Integrated sensors

Over the last years, the demand for sensors has grown rapidly. This is due to the need of monitoring several kinds of physical parameters in applications where a system must interact with its environment.

Furthermore, integrating traditional sensors onto a chip requires additional fabrication steps and materials. An integrated sensor can be made in a standard high volume VLSI process and consequently; the production costs can be minimized. An embedded temperature sensor combined with RFID circuitry enables a single-chip solution for commercial smart sensors. Complementary metal-oxide semiconductor (CMOS) sensors are strong

candidates for the integration in a wireless system, essentially because they consume little power. Moreover, a CMOS process represents a well-established, reliable and high performing technology that allows the full integration of both conditioning signal circuitry and transmission section. As a result, the system's power consumption, cost, and size are reduced.

Temperature sensor are very often integrated devices because an increasing number of applications require accurate intra-chip temperature control strategies to avoid, for example, frequency drift of RF oscillators, computational errors due to self-heating or to reduce the overall power consumption of complex systems [61].

The integrated CMOS temperature sensor fits low cost, high performance, and low power consumption perfectly.

Several temperature sensors topologies have been proposed in CMOS technology. Most of the systems, reported in literature, exploit a PTAT (proportional-to-absolute temperature) scheme, realized by mean of bipolar transistors[62]-[37][63].

CMOS technology is also compatible to implement photodiodes realized by a simple p-n junction that can be used for image sensors, light sensors, and in high speed optical communications.

CMOS image sensors are finding their way into an increasing number of applications in areas such as video communication, industrial inspection, security applications, space applications, automotive applications, biometrics, etc.[64]. The major reason for the interest is related to miniaturized and cost effective imaging systems. CMOS-based image sensors offer the potential opportunity to integrate a significant amount of VLSI electronics on-chip and reduce component and packaging costs.

Data transmission speed in electronic systems can be enhanced by utilizing an optical transmission technique. The optical transmission has been studied in board-to-board and chip-to-chip data transmission. For this reason a high speed and high responsivity photodiode is necessary[65].

Throughout this study, integrated photodiodes are used as light sensors to monitor the power level of solar irradiation.

3.3.1 Integrated Temperature Sensor

Diode temperature sensor

Semiconductor junction properties can be used to produce a current or voltage signal proportional to the temperature.

The simplest semiconductor sensor realization consists of a diode (Fig. 3.2).

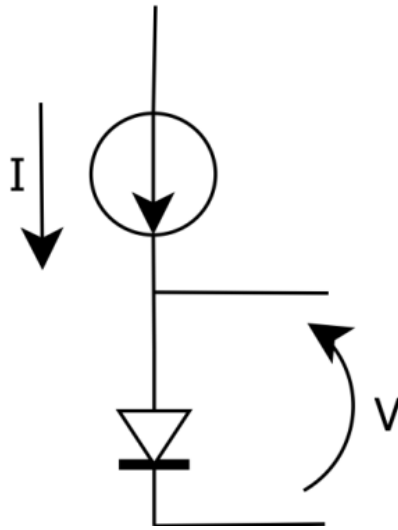


Fig. 3.2 Current driven diode

In a forward biased diode, the voltage between anode and cathode is a function of the junction temperature as indicated by the following relationship:

$$I = I_s e^{\frac{V}{nV_T}} = I_s e^{\frac{qV}{nKT}} \quad (3.1)$$

where:

- I_s is the reverse bias saturation current (of a magnitude $10^{-6} \div 10^{-9}$ A); it is a constant value that depends on diode parameters and temperature;
- n is an empiric constant that depends on the semiconductor used ($n=2$ for Si, $n=1$ for Ge);
- V_T is the thermal voltage (25mV at a temperature of 27°C);
- k is the Boltzmann's constant ($1.38 \cdot 10^{-23}$ J/K);
- q is electron charge ;
- T is the temperature [K].

Inverting 3.1 the following is obtained:

$$V = \frac{nkT}{q} \ln\left(\frac{I}{I_s}\right) \quad (3.2)$$

From the derivative of (3.2) with respect to the temperature T , the following equation is found:

$$\frac{dV}{dT} = \frac{V}{T} - \frac{nkT}{q} \cdot \frac{d}{dT}(\ln I_s) \quad (3.3)$$

Consequently, to a diode voltage variation with temperature, corresponds a logarithmic variation of the saturation diode current. The reverse bias saturation current I_s that depends on diode parameters and temperature and can be expressed as:

$$I_s = KT^m \cdot e^{-\frac{E_{g0}}{nkT}} \quad (3.4)$$

where E_{g0} is the energy gap of the material (1.21 eV for silicon), K is a material constant independent from temperature and m is equal to 1.5 for silicon.

Substituting the (3.4) into (3.2), the relation between voltage and temperature becomes:

$$V = \frac{E_{g0}}{q} - \frac{kT}{q} (\ln K - \ln T) \quad (3.5)$$

A linear dependence of voltage from temperature, is shown in (3.5), in a junction where a constant current.

The device sensitivity is:

$$S = \frac{dV}{dT} = -\frac{k}{q} (\ln K - \ln I) \quad (3.6)$$

that for a silicon diode supplied with a 1 mA current, is equal to -2 mV/°C.

The temperature dependence off the diode saturation current represents a major problem of this simple configuration. For this reason, two diodes can be used very close each other on the same chip, in order to have very similar (ideally, the same) characteristics, as shown in Fig. 3.3.

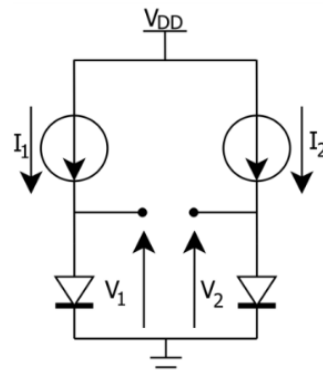


Fig. 3.3 Scheme of absolute temperature sensor with matched diode

If two fixed currents, with a stable temperature behavior, flow through the diodes the respective junction voltages are:

$$V_1 = \frac{kT}{q} \ln\left(\frac{I_1}{I_s}\right) \quad V_2 = \frac{kT}{q} \ln\left(\frac{I_2}{I_s}\right) \quad (3.7)$$

If the saturation current is identical for the diodes, by measuring the difference $V_1 - V_2$ it is possible to obtain the temperature as:

$$V_1 - V_2 = \frac{kT}{q} \ln\left(\frac{I_1}{I_2}\right) \quad (3.8)$$

where, in this case, the voltage given by the difference between $V_1 - V_2$ exhibits a positive temperature coefficient, called PTAT (Proportional To Absolute Temperature) voltage.

BJT temperature sensor

The base-emitter voltage of a bipolar transistor, V_{BE} , is temperature-dependent including a relationship similar to that of a forward biased diode. In practice, a thermodiode can be simply obtained by short-circuiting the base to the collector of the transistor: In this way, the only active junction is that formed between the base and emitter regions. If two bipolar transistors operate at unequal current densities, then the difference between their base-emitter voltages is directly proportional to absolute temperature[66].

Considering the circuit depicted in Fig. 3.4: if two identical transistors ($I_{S1} = I_{S2}$) are biased at collector currents of nI_0 and I_0 , and their base currents are negligible, then the difference between their base-emitter voltages has the following relationship:

$$\Delta V_{BE} = V_{BE1} - V_{BE2} = V_t \ln \frac{nI_o}{I_{s1}} - V_t \ln \frac{I_o}{I_{s2}} = V_t \ln n = \frac{kT}{q} \ln n \quad (3.9)$$

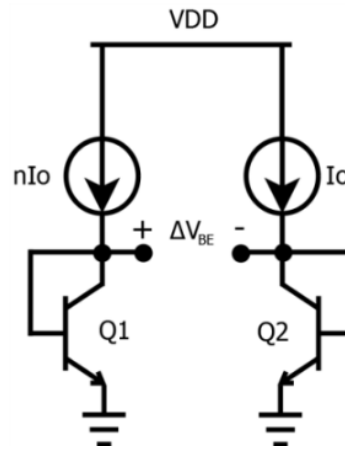


Fig. 3.4 BJT biased a different current

The V_{BE} difference exhibit a positive temperature coefficient $kT/q \ln n$ which depends only on the collector currents ratio, theoretically removing all the geometrical and process variations related to the device manufacturing.

3.3.2 Integrated light sensor

Typically, a photocurrent is generated when an incident light produces electro-hole pairs in a photodiode. This current is enhanced when reverse bias is applied at the two sides of a photodiode, because the electro-hole pairs are separated more effectively. The photocurrent is made up of two contributions:

1. the diffusion current due to an imbalance of carrier concentration outside of the depletion region; indeed the electric field outside of the depletion region can be assumed as zero, meaning that the drift current only happens within the depletion region;
2. the drift current due to the separation of electron-hole pairs within the electric field of the depletion region due to the of low-level injection regime, meaning that the variation of majority carrier concentration can be neglected

Before going into detail on how a CMOS photodiode model is developed, certain parameters must be considered. The function $G(x, \lambda)$ represents the excess minority carrier generation rate, the number of excess

minority carrier produced within each unit volume $I/(cm^3x sec)$. The depth from the illuminated surface, where the electrical contact is also placed is represented by x , while λ stands for the wavelength of the incident light. This mathematical function describes that the excess minority carrier generation rate is a function of the incident wavelength and the depth of distance from the incident light contact surface. The excess minority carrier generation rate $G(x, \lambda)$ decays exponentially moving from the surface to the bottom contact as shown below :

$$G(x, \lambda) = \varphi(x)\alpha e^{-(\alpha x)} \quad (3.11)$$

The parameter of $\varphi(x)$ is a photon flux, and x is the distance from the incident surface. If $\varphi(0)$ represents the photon flux at the top surface, $\varphi(0)$ and $\varphi(x)$ can be expressed as follows:

$$\varphi(0) = \frac{P_{in}}{h\nu} (1 - R) \quad (3.12)$$

$$\varphi(x) = \varphi(0)e^{-(\alpha x)} \quad (3.13)$$

where R is a reflection rate, h is the Planck constant ($6,626 \times 10^{-34} J \cdot s$), P_{in} is the power of incident light, ν is the frequency of incident light, and α is the absorption coefficient of the photo-receiving material. The absorption coefficient is an inverse of the absorption length that indicates the length where the photon flux decays to $1/e$ its starting value. For silicon material, the relationship between the absorption length and light wavelength is shown in Fig. 3.5 [67].

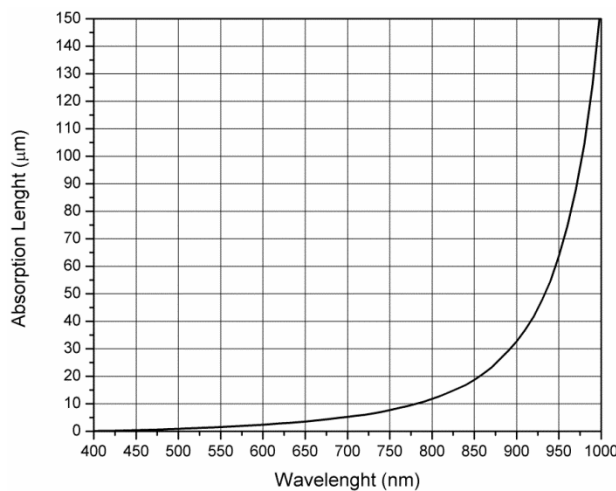


Fig. 3.5 Relationship between absorption length and wavelengths

The basic structure of the proposed CMOS photodiode is shown in Fig. 3.6. Assuming that the electric field only exists within the depletion region, the drift current then could only be generated within the depletion region. Indeed, by integrating the carrier generation rate along the depletion region, one gets the number of all carriers. Each carrier is then multiplied by its electron charge to obtain the intensity of the drift current within the depletion region, as shown below:

$$J_{drift} = -q \int_{x_n}^{x_d} G(x, \lambda) dx \quad (3.14)$$

Next the diffusion current, produced by the density imbalance outside of the depletion region is derived. As the photocurrent is produced by the minority carriers, its behavior could be studied at the equilibrium state. The equilibrium equation, in an N-type semiconductor where the minority carrier is hole, is the following:

$$D_p \frac{d^2(p_n(x) - p_{n0})}{dx^2} - \frac{p_n(x) - p_{n0}}{\tau_p} + G(\lambda, x) = 0 \quad (3.15)$$

where p_{n0} represents the density of the minority carrier (hole) at the equilibrium state; p_n is all the minority carrier concentration after light incidence; D_p is the hole's diffusion coefficient and τ_p is lifetime of the hole.

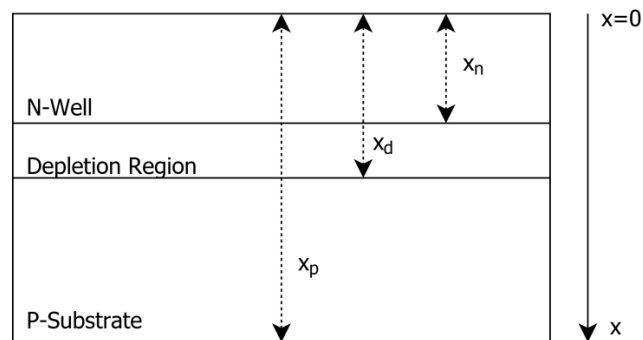


Fig. 3.6 Cross section of photodiode

The boundary conditions must be included to derive the particular solution, after that general solution has been obtained. The first set of boundary conditions is at the surface area where $x = 0$:

$$D_p \times \frac{\partial(p_n(x) - p_{n0})}{\partial x} = [-(p_n(x) - p_{n0}) \times S_p]_{x=0} \quad (3.16)$$

The S_p is the surface recombination velocity of the hole at the semiconductor's surface area. The second set of boundary conditions would be on the edges of the depletion region of $x = x_n$. Assuming the low-level injection, the boundary condition is represented by the following:

$$p_n(x_n) = p_{n0} e^{\left(\frac{-qV_{bias}}{kT}\right)} \quad (3.17)$$

V_{bias} is the reverse-bias voltage added at the two sides of the photodiode, k as the Boltzmann constant, and T is the absolute temperature. Through this set of boundary conditions it is possible to achieve the particular solution of $p_n(x)$. In addition to this, when the relation below is included it would allow the calculation of current density generated in an N-type semiconductor:

$$J_n = qD_p(\partial p_n / \partial x)_{x=x_n} \quad (3.18)$$

Similarly, the current density in a P-type semiconductor could be derived through the following equations:

$$D_n \frac{d^2(n_p(x) - n_{p0})}{dx^2} - \frac{n_p(x) - n_{p0}}{\tau_n} + G(\lambda, x) = 0 \quad (3.19)$$

$$D_n \times \frac{\partial(n_p(x) - n_{p0})}{\partial x} = [-(n_p(x) - n_{p0}) \times S_n]_{x=x_n} \quad (3.20)$$

$$n_p(x_d) = n_{p0} e^{\left(\frac{-qV_{bias}}{kT}\right)} \quad (3.21)$$

The current density in P-type semiconductor can be expressed as follows:

$$J_p = -qD_n(\partial n_p / \partial x)_{x=x_d} \quad (3.22)$$

Finally, the dark current must be considered. The dark current depends on many factors such as temperature, doping density, bias voltage and defects introduced in the manufacture process. To quantify the dark current generated by the biased voltage and carry densities, the incident light is set to 0. The following equation derives the total current density, where J_{dark} is the dark current:

$$J_{tot} = J_{drift} + J_n + J_p - J_{dark} \quad (3.23)$$

3.3.3 Analog Front End

Differential Amplifier

In a differential amplifier the output signal is equal to the amplified difference of the two input signals. In many analog circuits, differential amplifier is considered as one of the most important building blocks. This circuit is formed by a differential pair as shown in Fig. 3.7.

Assuming that M1 and M2 are exactly the same and both operate in saturation region, the drain current of each device can be expressed as follows:

$$I_{d1,2} = K(v_{gs1,2} - V_T)^2 \quad (3.24)$$

where:

$$K = \frac{1}{2} \mu_n C_{ox} (W/L) \quad (3.25)$$

μ_n is the free electrons mobility, C_{ox} is the gate capacitance per unit area, W and L are the channel width and length respectively of M1 and M2.

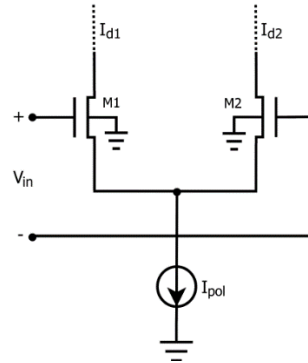


Fig. 3.7 Differential pair Amplifier

The equation (3.24) can be rewritten as:

$$v_{gs1,2} = V_T + \sqrt{\frac{I_{d1,2}}{K}} \quad (3.26)$$

The differential input could be expressed as:

$$v_{in} = v_{gs1} - v_{gs2} \quad (3.27)$$

From the difference between I_{d1} and I_{d2} and substituting (3.27), the following equation is obtained:

$$\sqrt{I_{d1}} - \sqrt{I_{d2}} = \sqrt{K} v_{in} \quad (3.28)$$

The current generator I_{pol} imposes the constraint:

$$I_{d1} + I_{d2} = I_{pol} \quad (3.29)$$

The equations (3.28) and (3.29) form a system of two equations in two unknowns, thus the drain current of each MOS transistor is obtained as:

$$I_{d1} = \frac{I_{pol}}{2} + \sqrt{2KI_{pol}} \left(\frac{v_{in}}{2}\right) \sqrt{1 - \frac{(v_{in}/2)^2}{(I_{pol}/2K)}} \quad (3.30)$$

$$I_{d2} = \frac{I_{pol}}{2} - \sqrt{2KI_{pol}} \left(\frac{v_{in}}{2}\right) \sqrt{1 - \frac{(v_{in}/2)^2}{(I_{pol}/2K)}} \quad (3.31)$$

The plot of each drain current of the differential pair is illustrated in Fig. 3.8.

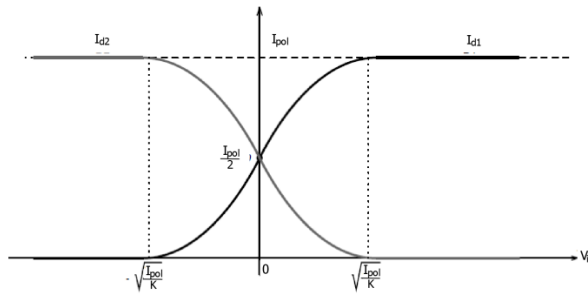


Fig. 3.8 Differential pair drain currents versus differential input voltage

If $-\sqrt{I_{pol}/K} \leq v_{in} \leq \sqrt{I_{pol}/K}$ both transistors conduct, but outside this range one of the two transistors, M1 or M2, turns off and the entire tail current I_{pol} slides on the other transistor.

Fig. 3.9 shows a CMOS differential amplifier with an active load; the load has been implemented by a PMOS current mirror. In this circuit, (M1, M2) and also (M3, M4) are mutually identical and thus the tail current I_{pol} is equally divided between M1 (M3) and M2 (M4) in the absence of differential input voltage. Due to the circuit symmetry, the DC voltage level at the drain of M1 and M2 is the same and is equal to:

$$V_{out} = V_{DD} - |V_{Tp}| - \sqrt{\frac{I_{pol}}{K_p}} \quad (3.32)$$

where $K_p = \frac{1}{2} \mu_p C_{ox} \left(\frac{W}{L}\right)_{3,4}$, μ_p is the hole carriers mobility and $\left(\frac{W}{L}\right)_{3,4}$ is the size of M3, M4.

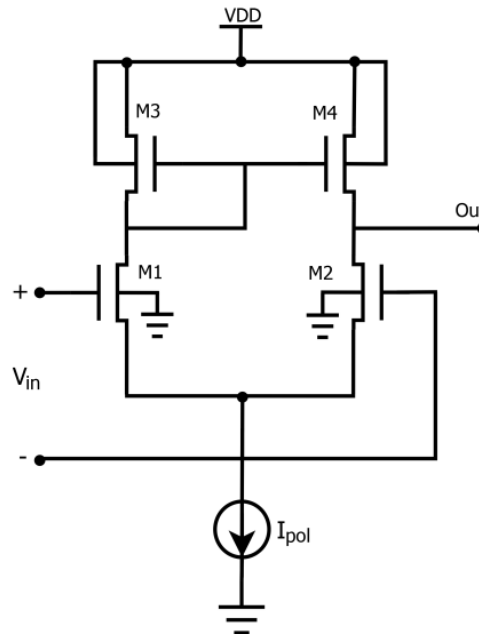


Fig. 3.9 CMOS differential amplifier with PMOS active load

Transimpedance Amplifier (TIA)

A transimpedance amplifier is an inverting amplifier that accepts an input signal in the form of a current from a high impedance signal source, such as a photodiode or a semiconductor based detector for radiation particles, and converts it into an output voltage. In this configuration (as shown in Fig. 3.10), the amplifier itself is acting as the current-to-voltage converter, with the output voltage gain set by the feedback resistor (R_{fed}).

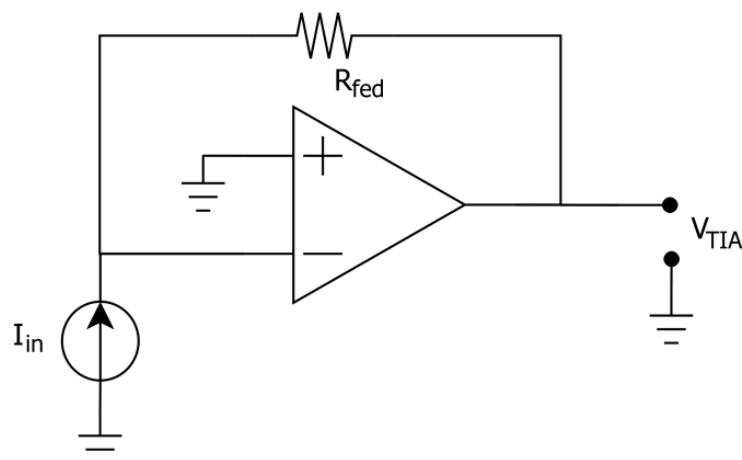


Fig. 3.10 Transimpedance amplifier configuration

3.4 AMS CMOS 0.35 μm Analog Sensors

The sensors realized in this work, have been designed in Austria MicroSystems (AMS) 0.35 μm CMOS technology, with four metal layers and two poly layers on p-type substrate [68]. Fig. 3.11 shows the cross-section of the wafer.

The p-type substrate has a thickness of 300 μm and a resistivity of 20 $\Omega\cdot\text{cm}$. The minimum MOS channel length for this technology is 0.35 μm . The gate oxide has a typical thickness of 7.6 nm. The metal layers have different thicknesses: 650nm for Metal 1, Metal 2 and Metal 3, about 1000nm to the Metal 4. This implies different values of sheet resistance and maximum current density. In particular, in the first three metal layer it can be flows a maximum current density of 1mA/ μm , while the Metal 4 can withstand up to 1.6mA/ μm . The metal layers are isolated from each other by an oxide layer of about 1 μm . The top metal level is insulated with two insulation layers, each one having a thickness of about 1 μm .

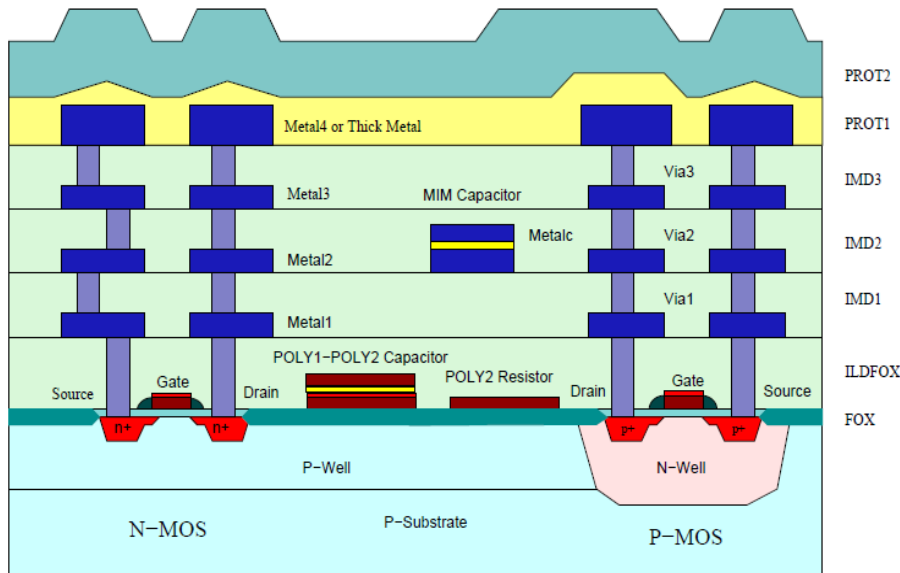


Fig. 3.11 Wafer section for AMS 0.35 μm CMOS Technology

3.4.1 AMS CMOS 0.35 μm Temperature Sensor

The proposed solution for the design of the CMOS temperature sensor is based on the proportion between temperature and voltage in PTAT configuration. This relationship is due to the difference between two base-emitter voltages under different bias current densities. The reason for choosing this configuration is the possibility to exploit bipolar transistor properties to build a temperature sensor in CMOS technology.

The sensitivity, the signal level and the linearity of the sensor have been specially tuned in order to simplify the further Analog-to-Digital conversion (ADC).

The sensor has been designed in such a way to have a linear dependence of voltage vs. temperature for a wide temperature range (from room temperature to 100 $^{\circ}\text{C}$).

The analog temperature sensor consists of two building blocks: a PTAT voltage generator and a differential amplifier.

In this study, to obtain a proportional output signal with respect to absolute temperature, two junctions with different intensity currents have been realized. As show in Fig. 3.12, a MOS current mirror has been realized to bias the PTAT.

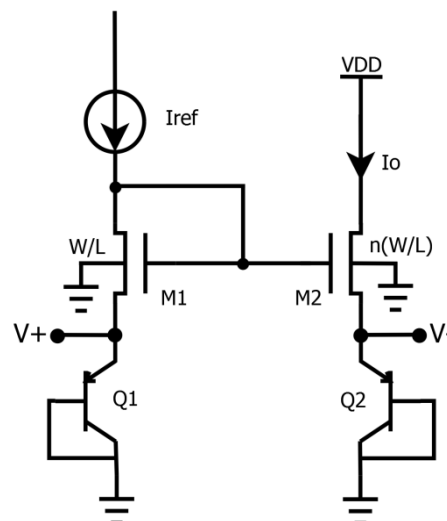


Fig. 3.12 PTAT with MOS mirror current

The transistors work in saturation region; if the channel length modulation is neglected [66], the circuit is governed by the following equation:

$$I_{ref} = nI_o \quad (3.10)$$

where I_{ref} is the reference current of the mirror, I_o is the current of the second branch of the mirror and n is the ratio among the currents. The MOS have been sized as shown in Table 3.1. In this way the ratio of currents, n , is equal to 10.

Table 3.1 Dimensions of current mirror transistors

	M1	M2
W	1 μ m	10 μ m
L	1 μ m	1 μ m

The reference current I_{ref} has been generated through an integrated bias current generator (BBIAS, available in the standard cell library of the used technology) that delivers a constant current of 11.5 μ A [69]. This bias current generator has the following characteristics:

- Small Area 0.019mm²;
- Size x=112 μ m y=172 μ m;
- Supply Voltage 3.0 to 3.6V;
- Temperature Range -40 to 125°C;
- Power Down Mode
- High Current Stability over Supply Voltage Range.

Note that, since the source supplies current to each diode-connected device, I_{ref} and I_o are relatively independent of V_{dd} .

To evaluate the performances of the designed temperature sensor, simulations have been made in Cadence. In Fig. 3.13 the emitter voltages of transistors $Q1$ and $Q2$ at various temperatures, are shown. These voltages have a negative sensitivity with respect to the temperature variations.

Through these results, it is possible to calculate the proportional voltage at the absolute temperature:

$$V_{PTAT}(T) = V_+ - V_- \quad (3.11)$$

In Fig. 3.14 is depicted the differential output of the PTAT in a temperature range from 0 to 100°C.

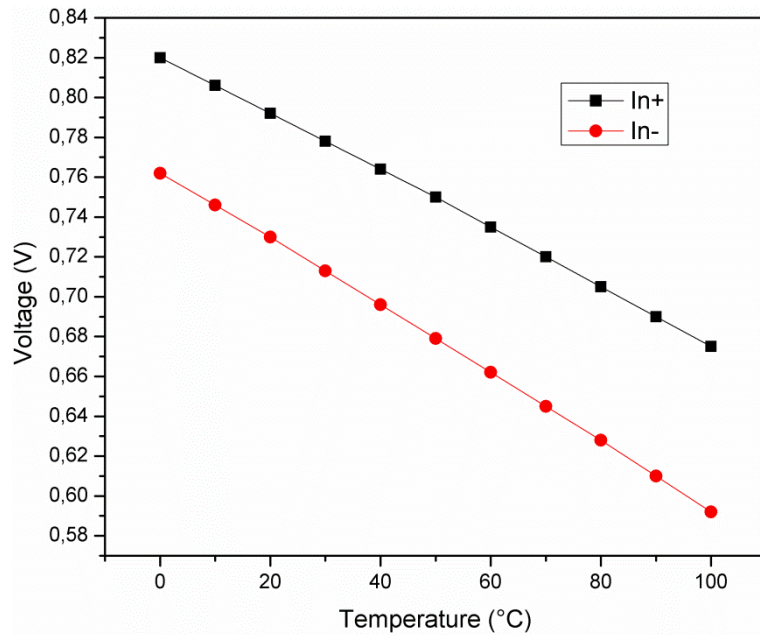


Fig. 3.13 Emitter voltage of transistors Q1 and Q2 at various temperature

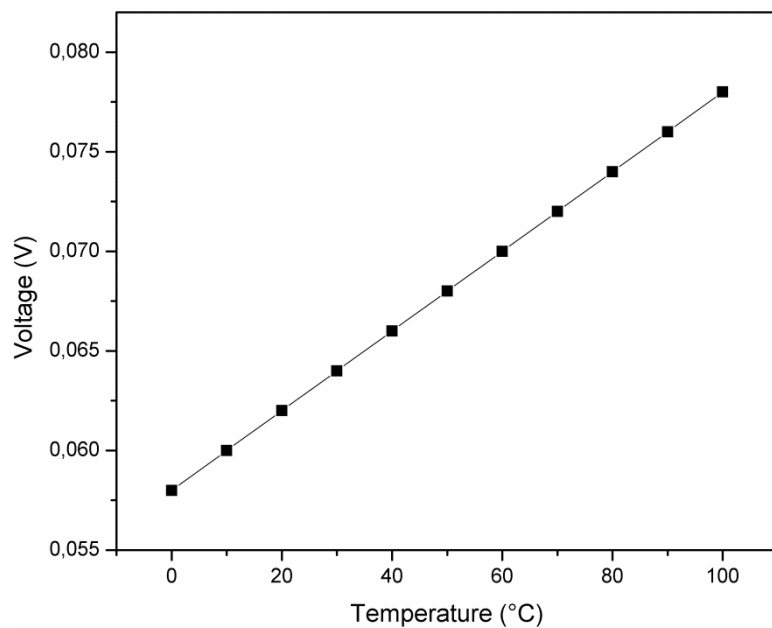


Fig. 3.14 Differential output of the PTAT in a temperature range from 0 to 100°C

The sensitivity of the sensor has been calculated as follow:

$$S_{PTAT} = \frac{\Delta V_{PTAT}(T)}{\Delta T} = \frac{0.78 - 0.58}{100} = 2 \text{ mV}/^{\circ}\text{C}$$

The output signal level of the PTAT is about few hundreds of mV, therefore an amplifier stage has been carefully tuned to get a linear dependence and to obtain reasonable voltage level that can be either read with a simple setup of using it as analog input for an ADC. Being the PTAT output differential, the topology requested for the amplifier is differential as well. Considering the circuit depicted in Fig. 3.15, the amplifier is composed of differential couple M5 and M6, with M3, M4 connected as active load.

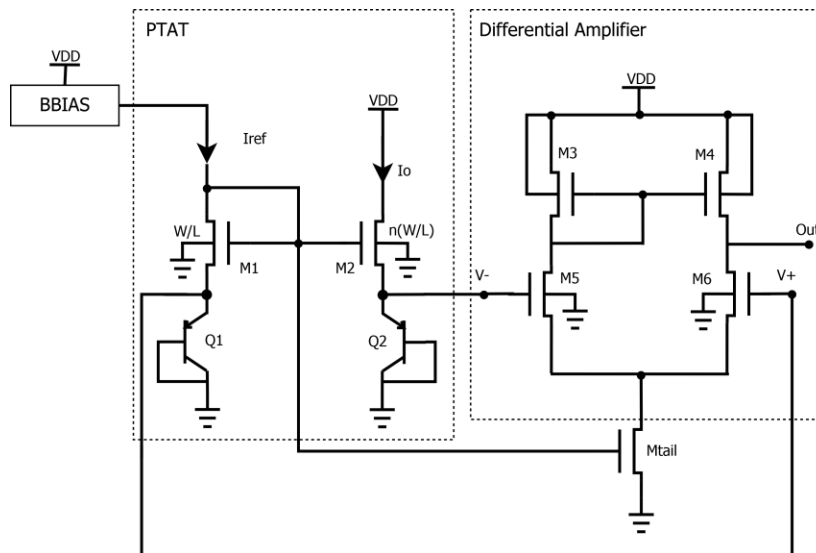


Fig. 3.15 Architecture of the integrated PTAT with differential amplifier.

The MOSFET's that formed the amplifier have been sized as follows in Table 3.2

Table 3.2 Transistor dimensions of differential amplifier

	M3	M4	M5	M6
W	7 μm	7 μm	10 μm	10 μm
L	1 μm	1 μm	1 μm	0,35 μm

In Fig. 3.16 is shown the characteristic of the PTAT with amplification.

Both signals, with and without amplification, show a linear dependence of the temperature variations. The amplified signal clearly presents a higher sensitivity calculated as:

$$S_{PTAT} = \frac{\Delta V_{PTAT}(T)}{\Delta T} = \frac{2.03 - 0.51}{80} = 19 \text{ mV}/^{\circ}\text{C}$$

In addition the PTAT with differential amplifier present a saturation over 90 $^{\circ}\text{C}$.

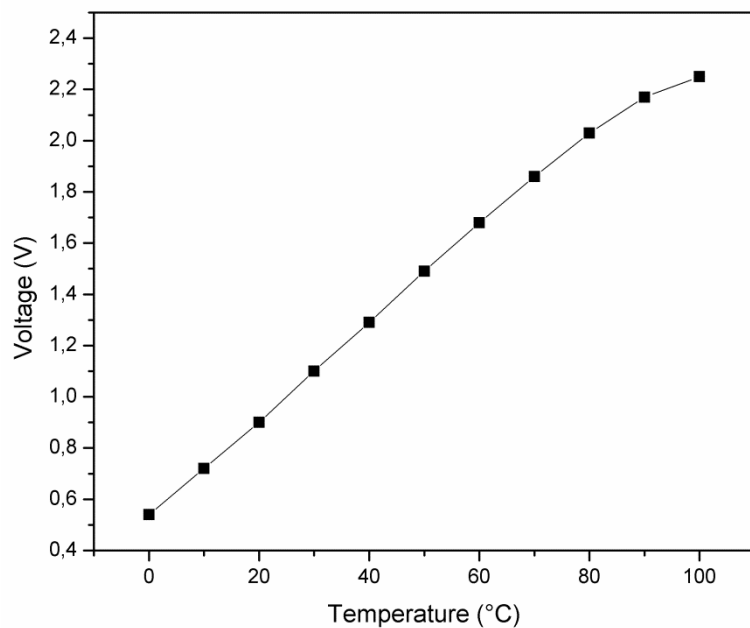


Fig. 3.16 Simulated characteristic of the PTAT Vs temperature

3.4.2 AMS CMOS 0.35 μm Light Sensor

The proposed solution for the design of the CMOS light sensor is based on a simple p-n junction formed by a P-type substrate and N-type well. This structure could be represented as a micro solar cell that produces current when it is irradiated with incident light on its active surface. The first metal layer (metal one) has been used to build fingers to collect the photocurrent and as anode contact for the micro cell as well. The structure of the light sensor is shown in Fig. 3.17.

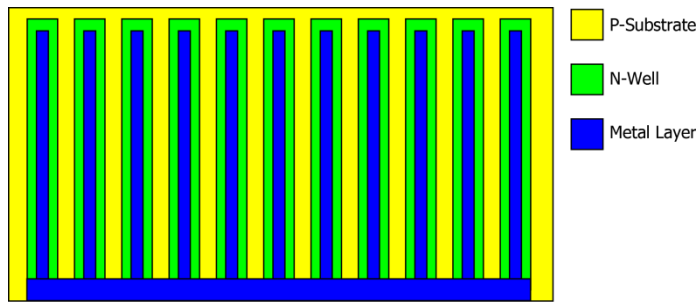


Fig. 3.17 Structure of realized micro solar cell (top view)

In order to convert the current signal, generated by an integrated solar cell, into a voltage signal, it is necessary to use a transimpedance amplifier.

In this study, the transimpedance amplifier has been designed according to the schematic depicted in Fig. 3.10. An integrated operational amplifier (OP_LIN, available in the standard cell library of the used technology)[70] has been used and a resistance of $100\text{k}\Omega$ has been used as R_{fed} .

Integrated solar cell has been sized to generate a photocurrent in a specific range, in such a way that the amplifier works in the linear region of its characteristic.

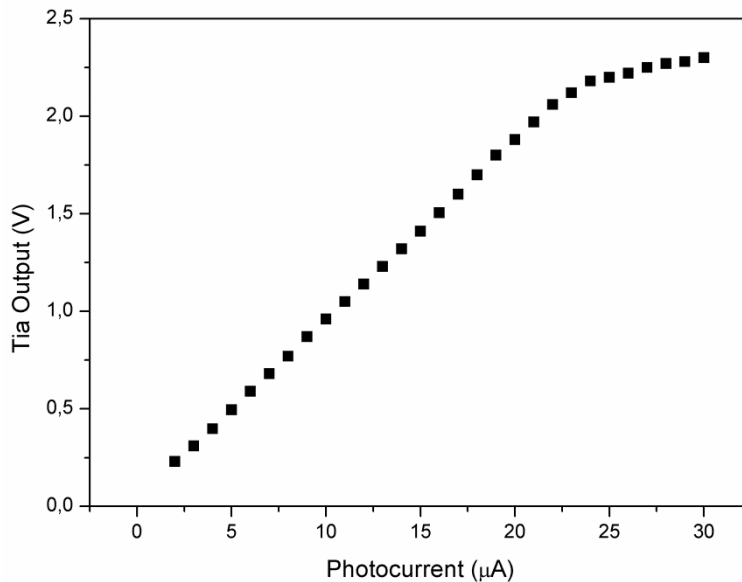


Fig. 3.18 Simulated Characteristic of the Transimpedance Amplifier vs photocurrent

This range of current has been obtained from Cadence simulation. As shown in Fig. 3.18, linear region has been estimated with an input current

range of $2\text{-}22\mu\text{A}$. For this reason, the integrated solar cell has the following dimensions:

$$(300 \times 200)\mu\text{m}^2$$

The sensitivity, the signal level and the linearity of the sensor have been carefully studied in order to simplify the further Analog-to-Digital conversion (ADC) as in the case of the temperature sensor.

3.5 Digital Section

The voltage signals obtained from the temperature and light measurements have to be digitalized and serialized to modulate the RF section. In Fig. 3.19 the full design of the digital block is shown. An analog digital converter (ADC) has been used to convert the analog signals coming from the sensors; a shift register has been realized, in PISO topology, to serialize the parallel output from the ADC; a Load signal must be generated to activate the PISO from the Clk signal, for this reason a Load generator has been implemented.

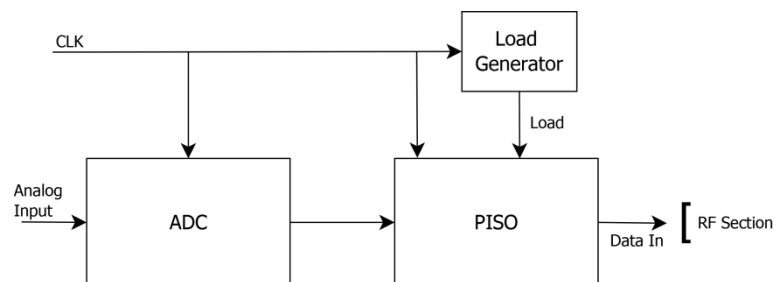


Fig. 3.19 Block diagram of Digital Section

3.5.1 Analog-to-digital conversion

An 8-bit ADC converts the analog input voltage signals in 256 quantization levels. In this thesis, an integrated ADC (ADC8 available in the standard cell library of the AMS technology) has been used [71]. It is an 8-bit successive approximation analog to digital converter. The architecture is based on two resistor dividers. It is composed of a comparator, a shift register (SAR8) and a digital-to-analog converter (DAC8). The analog input signal is

taken from the comparator that is interfaced with a shift register (SAR8); the latter communicates with a digital to analog converter (DAC8) whose output is sent to the comparator. The system is based on a feedback and, consequently, the conversion will be completed when the input reference of the comparator and the output of the DAC have the same value. At the end of the conversion, digitalized data are provided in the bus DATA in parallel, so that the data have to be serialized.

The conversion is carried out over 9 clock cycles of the master clock. The conversion range is given by positive reference voltage (VRP) and negative reference voltage (VRN), as shown in Table 3.3, where $1LSB = (VRP - VRN)/256$.

Table 3.3 Code Table

Output Code	Input Voltage
0000 0000	VRN ... 1LSB
0000 0001	1LSB ... 2LSB
0000 0010	2LSB ... 3LSB
...	...
1111 1111	255LSB ... VRP

3.5.2 Parallel Input Serial Output

To serialize the parallel output, that comes from ADC, an 8-bits PISO shift register has been implemented. It has been realized with the implementation of a VHDL code. The Cadence tool Encounter has been used to synthesize the hardware description language to standard cells. As shown in Fig. 3.19, the input signals are: clock and load, reset and parallel-inputs that are the output of the ADC. Moreover, the first bit of the serial output is the least significant bit of the parallel inputs.

3.5.3 Load generation

The load input signal is used as a start signal for the PISO after the AD conversion. A digital circuit has been designed to obtain the synchronization of the blocks.. The load circuit was designed to generate an output signal each

50 clock cycles with a fixed period of 1 clock cycle (Fig. 3.20). The architecture of the block is similar to that of the frequency divider.

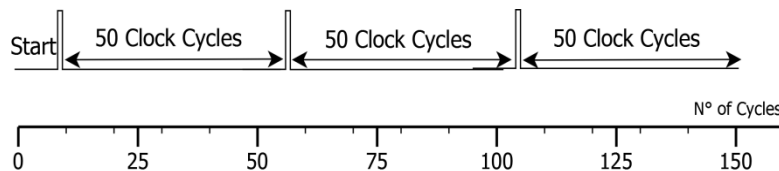


Fig. 3.20 Timing diagram of the start signal generation

3.6 RF Section

In this section, a directly OOK modulated oscillator-based transmitter is proposed, as depicted in Fig. 3.21. The transmitter topology exploits a cross-coupled complementary LC oscillator whose differential output is buffered on an integrated dipole antenna. The common source differential amplifier is directly coupled to the former circuit. A start-up circuit allows the duty-cycling of the transmitter and the implementation of the OOK modulation by alternatively powering the circuit on and off.

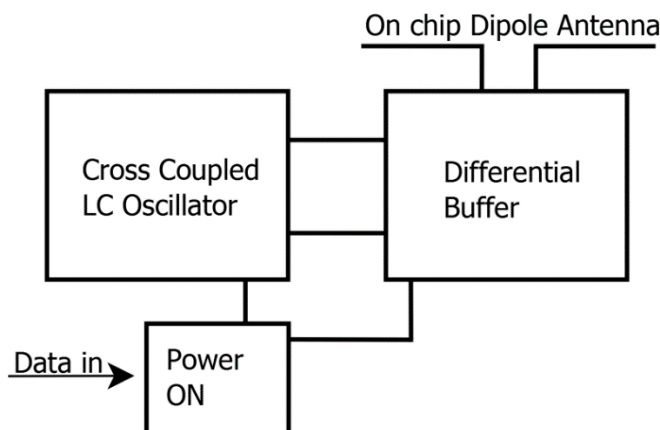


Fig. 3.21 Block diagram of the LC cross coupled transmitter topology

3.6.1 LC Cross-Coupled Oscillator design

LC cross-coupled oscillators are suitable circuits to be used in radio frequency systems. These kinds of oscillators offer high frequency stability over temperature, voltage and process variations and low phase noise. When

comparing LC cross-coupled oscillators use few active devices respect to the common oscillator topologies. These characteristics allow the use of these oscillator architectures in gigahertz applications.

In this oscillator topology the oscillation frequency is set by an inductors and capacitors (LC) network.

The simplest configuration of LC-cross coupled oscillator is obtained with a pair of NMOS arranged so that the drain of each device is connected to the gate of the other ('cross-coupled') and to a terminal of the resonant LC network [72], as shown in Fig. 3.22.

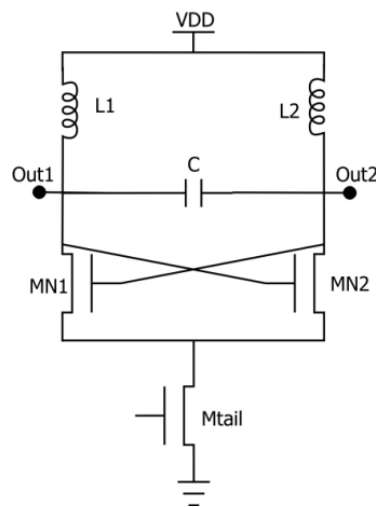


Fig. 3.22 Schematic of the ‘cross-coupled’ LC MOS oscillator

A negative impedance, equal to $-2/g_m$ to the drain terminal which compensates the losses of resonant network (R_{tank}), as depicted in Fig. 3.23, is determined by the cross-coupled structure.

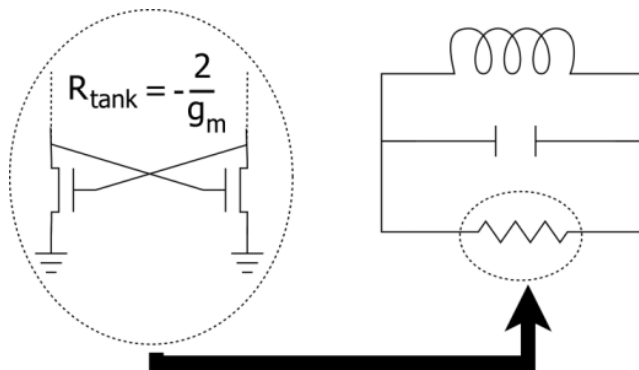


Fig. 3.23 LC Equivalent circuit

Generally, the series resistance of an inductor with an inductance L is given by:

$$R = \frac{2\pi fL}{Q} \quad (3.11)$$

where f is the resonance frequency and Q is the quality factor of the inductance.

In order to activate the oscillations is mandatory to have:

$$\frac{1}{g_m} \geq R \quad \text{with} \quad g_m = \frac{I_D}{V_{gs} - V_T} \quad (3.12)$$

To ensure that the oscillation starts, the following condition must be guaranteed:

$$\frac{2}{g_m} \geq R \quad (3.13)$$

Hence:

$$I_D = \frac{Q(V_{gs} - V_T)}{2\pi fL} \quad (3.14)$$

The current value I_D and, thus, the MOS sizes determine the value of the oscillator differential output. Out1 and Out2 are out of phase by 180° and are more or less symmetrical, depending on the symmetry of the circuit. In particular, the symmetry of the oscillator provides a low harmonic content.

Using only a pair of NMOS as in the above described configuration, it is possible to provide the differential transconductance (g_m) needed to generate oscillations despite the quality factor of the resonant network is low. To compensate the inductor losses, a negative resistance is necessary, for this reason a pair of PMOS (Fig. 3.24) can be used as active load[73]. The complementary topology allows oscillations to start also for low quality factors (Q_{tank}) of the resonating circuits. In fact in this structure, the inductor shows a poor quality factor Q_L , typically in a range from 4 to a maximum of 20 for enhanced structures [74]-[75].

Faster switch On and Off times reduce the active time of the transmitter and therefore its power consumption. This is obtained by a higher transconductance that is determined by the complementary cross-coupled pairs.

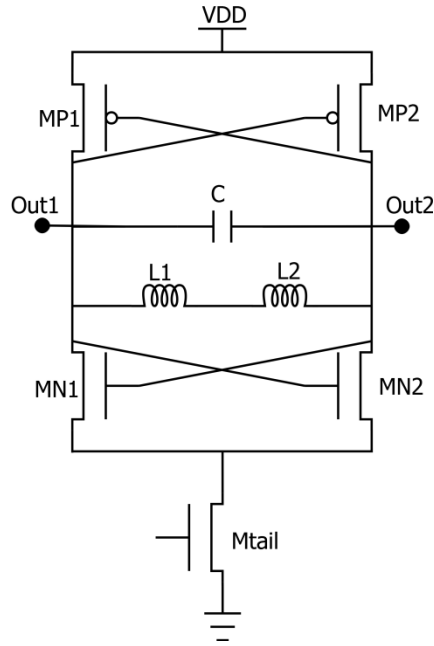


Fig. 3.24 LC cross-coupled oscillator with CMOS technology

Another advantage is the decrease increase of the supported data rate. The settling time t_s is defined as the time needed for the oscillation to reach 90% of its steady-state amplitude as reported in [76]. In a cross-coupled LC oscillator the settling time can be calculated by the following formula:

$$t_s \approx \frac{Q_{tank}}{\omega_0(A_{OL} - 1)} \left[2 \ln \left(\frac{V_0}{v(0)} - 1 \right) + 1.45 \right] \quad (3.15)$$

where ω_0 is the resonant angular frequency, $A_{OL} = \left| \frac{g_m}{2} \right| R_{tank}$ the open loop gain, V_0 the steady-state oscillation amplitude, $v(0)$ the initial condition. Thus, for a certain quality factor of the resonator circuit and for a given initial condition, an increase of the transconductance G_m of the transistors determines the reduction of the settling time of the oscillator. In particular, the overall transconductance G_m of the complementary cross-coupled pairs can be expressed as follows:

$$G_m = \frac{g_{mn} + g_{mp}}{2} \quad (3.16)$$

where g_{mn} and g_{mp} are the transconductances provided by the NMOS and the PMOS devices, respectively. Compared to the negative transconductance $\frac{g_m}{2}$ of a single cross-coupled pair, the G_m is almost doubled.

3.6.2 Power Amplifier

Power amplifiers are used, ideally, to amplify signals without compromising signal integrity, so that the information can be transmitted into the media and recovered by the recipient.

In Fig. 3.25, a simple inverter-based differential amplifier configuration is shown.

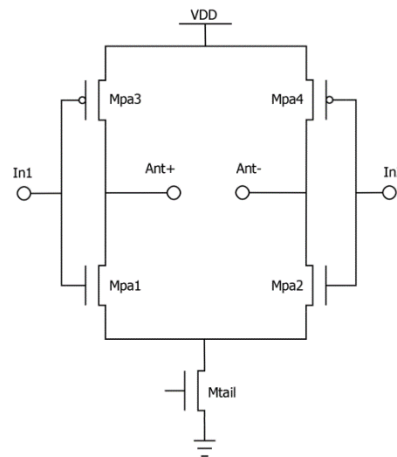


Fig. 3.25 Inverter-based differential amplifier configuration

The circuit works as follows. Let's assume that In2 is at the maximum voltage value, In1 is thus at the minimum one. In this case the Mpa3 PMOS of the first branch of the amplifier is on and feeds a certain current into the positive branch of the antenna (Ant+). On the other branch of the circuit, the Mpa2 NMOS device is on allowing the current that flows through the positive branch of antenna (Ant-) to be steered to ground.

The current flow through the antenna is reversed when In1 turns to a high value and In2 turns to a low value.

3.6.3 Power On

The power-on circuit uses a transmission gate for duty-cycling the transmitter and a PMOS current source to implement the OOK modulation by alternately powering the circuit on and off.

The power-on time of the transmitter limits the maximum data rate of the modulating signal. In this topology, the power-on time is dominated by

the settling time t_s of the oscillator which is proportional to the quality factor of the resonator tank and to the negative resistance of the cross-coupled pairs[76].

3.6.4 On Chip Dipole Antenna

The dipole antenna is the simplest feasible radiating element. It consists fundamentally of two wires appropriately fed by a balanced line. If the antenna is made from a single metal branch, it is defined monopole which can be powered directly from a coaxial line.

Dipole antenna can be implemented inside integrated systems and it is usually printed on silicon substrate with high resistivity in order to reduce the losses. Several investigations have been made in order to make manufacturing antennas directly on the standard substrate compatible with the conventional CMOS processes [77].

Besides the substrate compatibility, the antennas must be realized using the conductor and dielectric layers presented in conventional silicon technologies in such a way to be low cost. Currently, in CMOS technology there are 8-9 metal layers with a thickness ranging between 0.5 to 2 μm . The conductors can be either aluminum or copper. The metal layers are separated by a dielectric layers in SiO_2 with thicknesses ranging between 0.5 to 1 μm [78]. In Fig. 3.26 various structures of dipole antenna are shown, as linear, zigzag, meander and loop antenna, realized on silicon substrate.

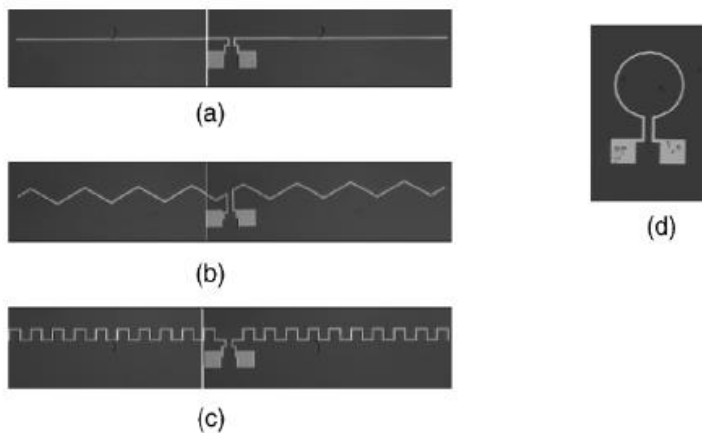


Fig. 3.26 Structures dipole antennas: (a) linear, (b) zigzag, (c) meander, (d) loop AMS CMOS Transmitter [78]

The proposed oscillator has been implemented exclusively with standard transistors provided by the four metal layers AMS CMOS 0.35 μm technology. The complete architecture of the integrated transmitter is shown in Fig. 3.29.

The resonating circuit employs simple square, 4-turns, spiral inductors fabricated in the top aluminum metal layer and a polysilicon capacitor, both provided by the 0.35 μm process. The employed coils exhibit a quality factor of 4.7 at 2.5 GHz. Two 2nH inductors have been exploited for maintaining a balanced differential circuit. Using two series inductors also allows to increase the tank resistance and thus the output voltage swing for a given bias condition. The polysilicon capacitor value has been accurately tuned to obtain a 2.5 GHz oscillation frequency.

Each transistor has a width/length ratio to achieve the needed negative transconductance for sustaining oscillations. Furthermore, the sizes of the cross-coupled pairs, together with the current tail, have been chosen to properly bias the differential power amplifier described in the next section. In **Table 3.4** each transistor dimension is present.

Table 3.4 Transistor dimensions of differential cross coupled LC oscillator

	MP1	MP2	MN1	MN2	Mtail
W	72 μm	72 μm	72 μm	72 μm	100 μm
L	0,35 μm	0,35 μm	0,35 μm	0,35 μm	0,35 μm

To verify the functionality of the oscillator, several simulations have been made using Cadence tool in which the oscillator model takes into account the parasitic parameters of the technology process.

Simulations have shown that the designed LC oscillator has a carrier frequency of 2.4892GHz as shown in Fig. 3.27.

Fig. 3.28 shows the start-up transient of the circuit ($t_{\text{start-up}}$). The oscillator requires 52 ns to settle from power-up.

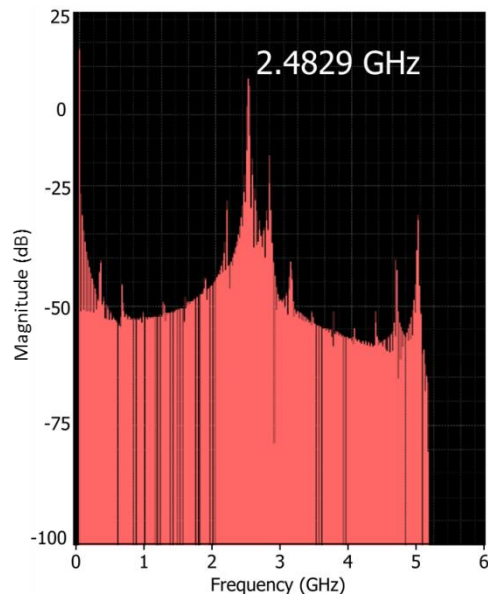


Fig. 3.27 Simulated frequency carrier of the designed LC oscillator

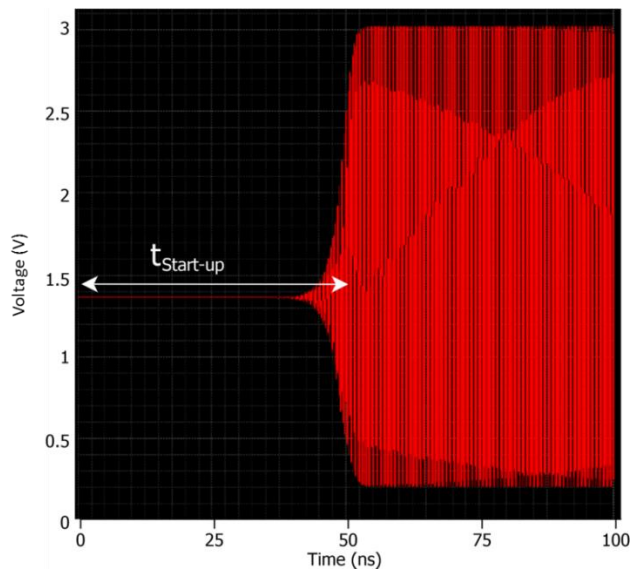


Fig. 3.28 Start-up time transient of the designed LC oscillator

In addition, a simple inverter-based differential amplifier has been implemented to feed the small dipole antenna. The differential pair has been accurately sized for maximizing the power delivered to the directly connected antenna. A width/length ratio of $65 \mu\text{m}/0.35 \mu\text{m}$ has been set for all Mpa transistors.

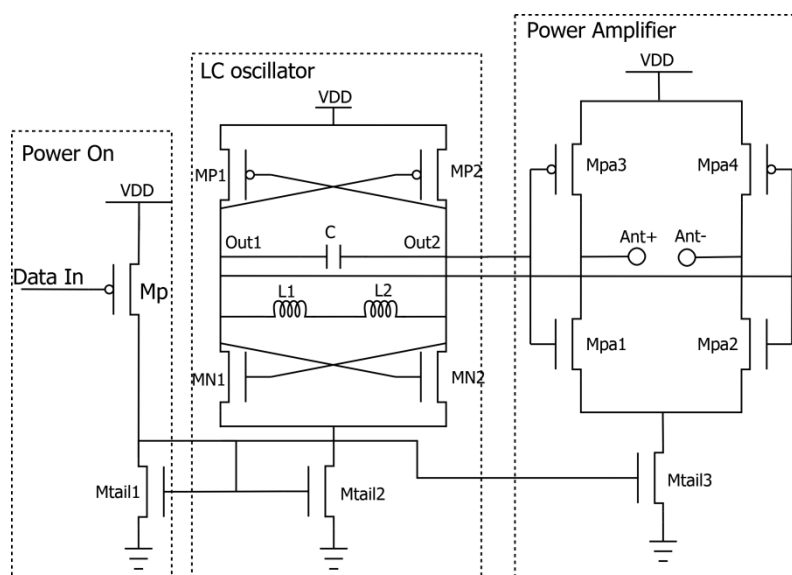


Fig. 3.29 Circuit schematic of the implemented transmitter

The on chip dipole is made above the top aluminum metal layer which has a thickness of $0.925\ \mu\text{m}$. For this antenna topology, the excitation is differential, which allows us to use active devices with differential output, and consequently avoid the common mode that needs a ground contact from the bottom of the chip. The dipole is made up of two arms of $1360\ \mu\text{m}$. The cross section is shown in Fig. 3.30.

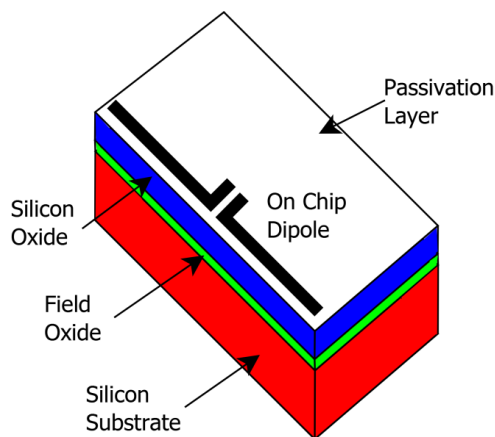


Fig. 3.30 On chip Dipole Cross Section

The substrate has the following characteristics: the electrical permittivity ϵ_r is 11.9 and thickness is $235\ \mu\text{m}$; field oxide layer has a thickness $1\ \mu\text{m}$ with an electrical permittivity of 4; finally the silicon oxide has a thickness of $3\ \mu\text{m}$ and ϵ_r is 4.1. In addition, a transparent passivation layer

with a thickness of $2\ \mu\text{m}$ and a ϵ_r of 7.9 is used to protect the chip from corrosion.

3.7 Experimental results

The experimental characterization of the system has been made both on the complete system and on each block separately. In particular the analog sensors (temperature and light), the digital conversion with the data serialization and finally the RF transmission of the data have been characterized.

A microphotograph of the die is given in Fig. 3.31. The area of the realized chip is $1\text{mm} \times 4\text{mm}$. After fabrication, the test chips were packaged in 44-pin TQFP packages.

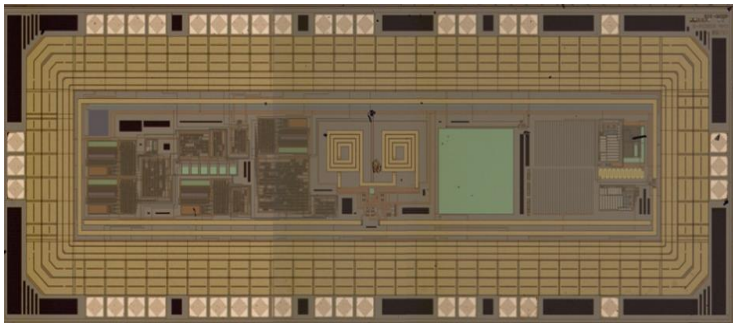


Fig. 3.31 Microphotograph of the realized chip

3.7.1 Temperature Sensor

To investigate the performance of the PTAT, the whole chip has been tested inside a temperature controlled heating chamber, using a standard PT100 as reference system as shown in Fig. 3.32.

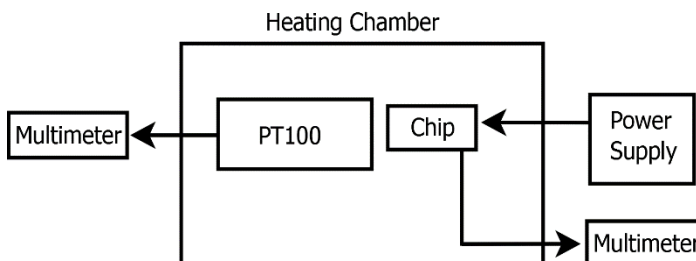


Fig. 3.32 Experimental setup used to characterize the PTAT performances

Both the voltage outputs from the two sensors have been monitored with a multimeter. The first characterization regards the relationship between the output voltage of the sensor and the temperature in the range 20–90°C. The integrated PTAT presents a good linearity (as shown in Fig. 3.33) of its characteristic in the range of interest with a sensitivity of 19.1mV/°C, at the amplifier output. The sensitivity is calculated as follows:

$$S_{PTAT} = \frac{\Delta V_{PTAT}(T)}{\Delta T} = \frac{1,98V - 0,803V}{88,6^{\circ}C - 27^{\circ}C} = 19,1 \frac{mV}{^{\circ}C}$$

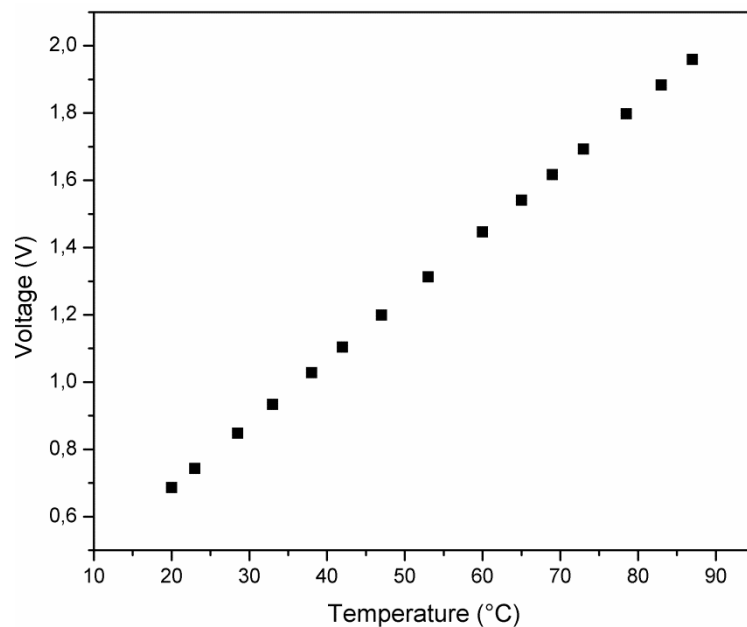


Fig. 3.33 Characteristic of the PTAT sensor

The parameter used to define the rate of linearity is the coefficient of determination (R^2), which establishes the goodness of the linear regression. In this case:

$$R^2 = 0,99962$$

The output voltage vs. temperature has been characterized for different values of supply voltage. As shown in Fig. 3.34 the supply voltage variations produce a translation of the sensor characteristic. However the curves slope remains constant which means almost constant sensitivity.

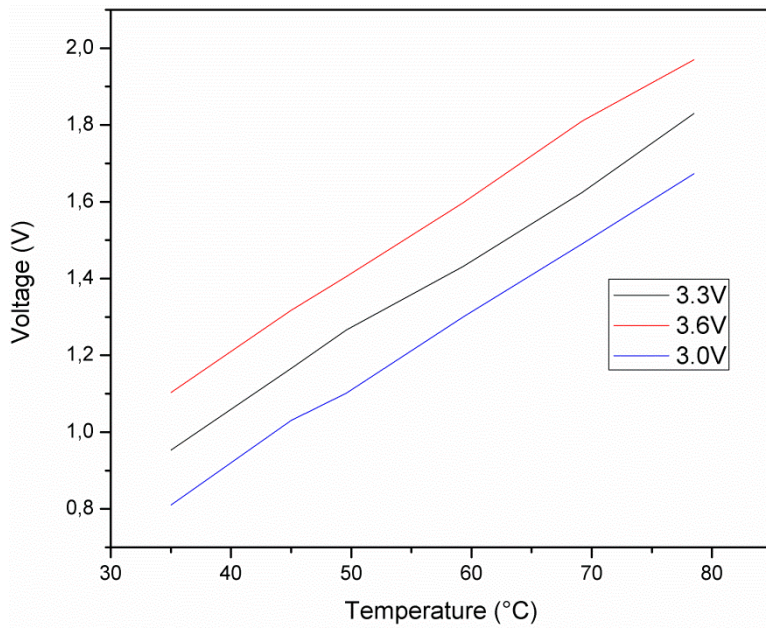


Fig. 3.34 Characteristic of PTAT sensor Vs Supply voltage variations

The measurements are perfectly repeatable, applying both a positive (up) and a negative (down) temperature ramp. Indeed, as shown in Fig. 3.35, the measurements could be repeated faithfully in both directions of operation.

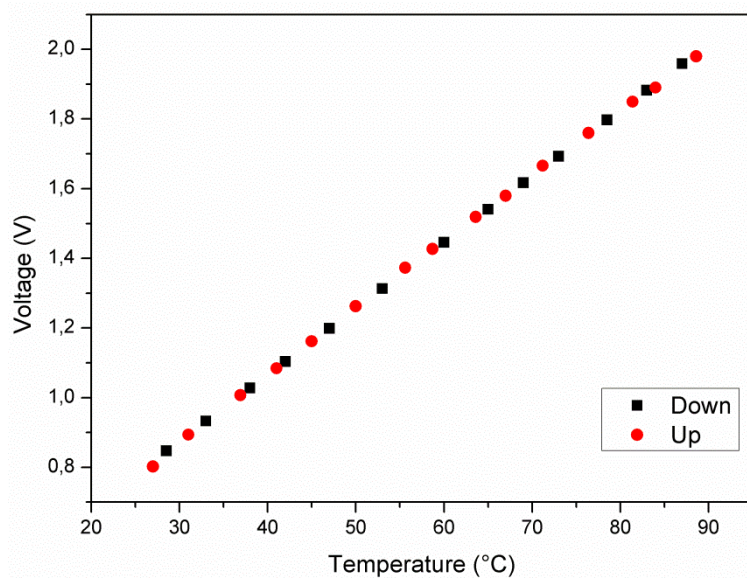


Fig. 3.35 Characteristic of PTAT in both directions of operation

3.7.2 Light sensor

To examine the performance of the light sensor, the whole chip, with a removable package, has been tested exposing the chip itself directly to the sunlight. Near our sensor a solar power detector has been positioned to monitor the value of solar irradiation (R). The photocurrent has been evaluated through a multimeter.

The integrated solar cell presents a good linearity (as shown in Fig. 3.36) of its characteristic in a range of interest (typical sunny day). The sensitivity is calculated as follow:

$$S = \frac{\Delta I_{ph}}{\Delta R} = \frac{24.6 - 2.6}{1160 - 125} = 0.212 \mu A/W/cm^2$$

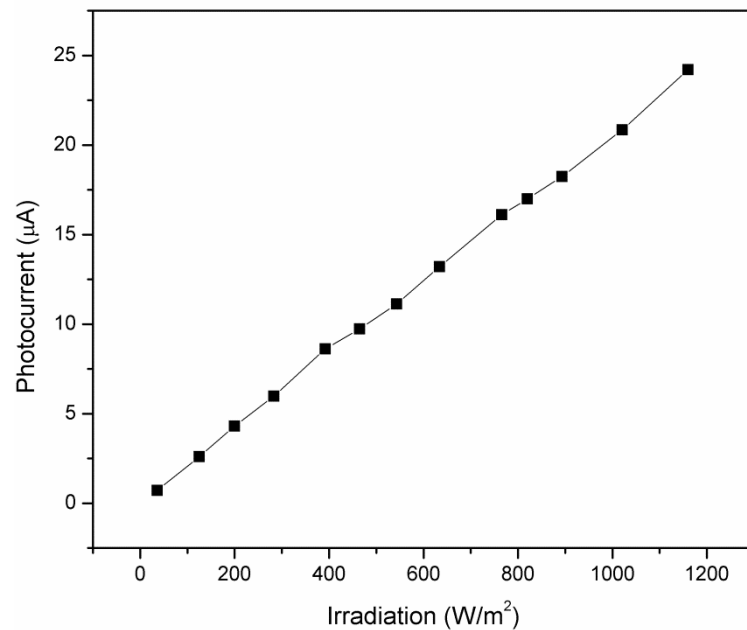


Fig. 3.36 Characteristic of the irradiation sensor under the sun

In this case through a linear regression the following coefficient of determination is calculated:

$$R^2 = 0.99915$$

In agreement with the simulation shown in Fig. 3.18, the range of the photocurrent, generated by the micro solar cell in a typical sunny day, enables the transimpedance amplifier to work in linear region.

In a first time, the transimpedance amplifier has been characterized with an ideal current generator. As shown in Fig. 3.37, the region, where the amplifier works in linear way, ranges between 2 and 22 μ A as demonstrated in simulation environment.

The sensitivity, both in simulation environment and experimental, is calculated as follows:

$$S_{exp} = \frac{\Delta V_{TIA}}{\Delta I_{ph}} = \frac{2.2 - 0.6}{-25 + 5} = 80 \text{ mV}/\mu\text{A}$$

$$S_{sim} = \frac{\Delta V_{TIA}}{\Delta I_{ph}} = \frac{2.2 - 0.5}{-25 + 5} = 85 \text{ mV}/\mu\text{A}$$

In addition, transimpedance amplifier has been characterized at various temperatures in order to detect the variations of the linear region.

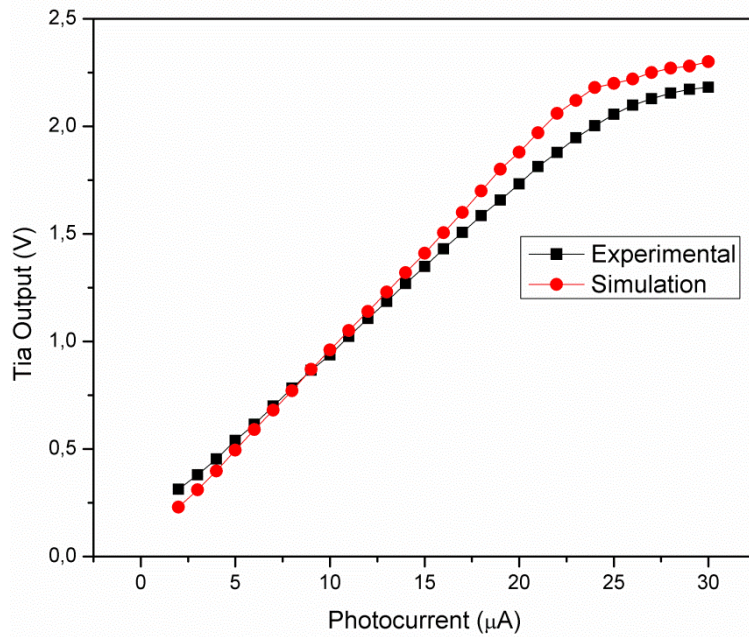


Fig. 3.37 Characteristic of the Transimpedance Amplifier output Vs photocurrent

As depicted in Fig. 3.38, the range of photocurrent where the TIA works in linear region decreases with increasing temperature. However, the functionality of the amplifier is guaranteed also for temperature of 80°C that can be assumed maximum value of temperature of the photovoltaic module in a hot day.

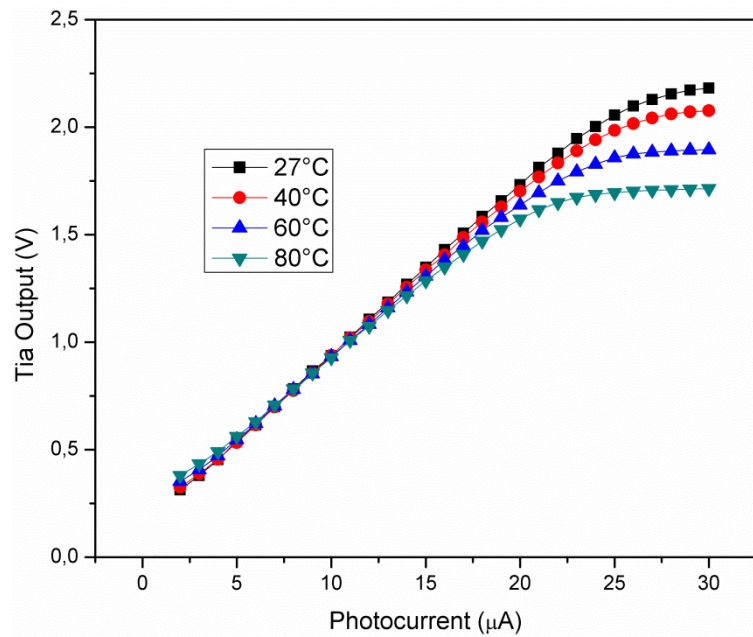


Fig. 3.38 Characteristic of the Transimpedance Amplifier output Vs photocurrent at various temperatures

Finally, the whole system has been characterized in order to calculate the sensitivity. The light sensor presents a good linearity (as shown in Fig. 3.39) of its characteristic in a range of interest (typical sunny day).

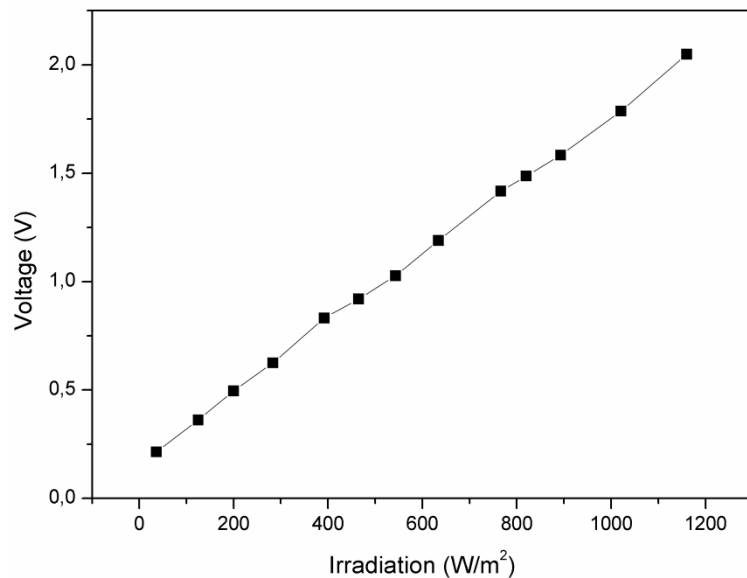


Fig. 3.39 Characteristic of the Transimpedance Amplifier output Vs photocurrent generated by the micro solar cell

The sensitivity is calculated as follow:

$$S_{Cel+Tia} = \frac{\Delta V_{TIA}}{\Delta R} = 16,96 \text{ mV}/W/cm^2$$

3.7.3 RF Transmitter performance

The RF performance of the implemented transmitter has been characterized using a 0.4-3 GHz bandwidth, 5dBi logarithm periodic dipole antenna (model R&S HL040) connected to a R&S FSV signal and spectrum analyzer acting as the receiver.

The experimental measurements have shown a carrier frequency of the complementary cross-coupled LC oscillator based transmitter of about 2.54 GHz as shown in Fig. 3.40.

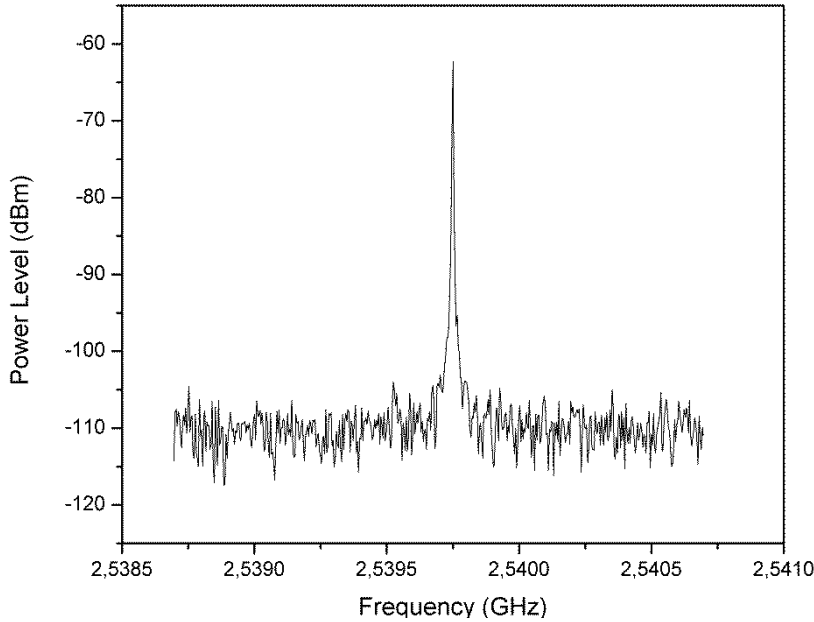


Fig. 3.40 Carrier Frequency of the transmitter

The proposed LC oscillator shows a phase noise of -90dBc/Hz at 1MHz offset from the center frequency as shown in Fig. 3.41. The phase noise is estimated as follow:

$$L(\Delta f)_{dBc} = P_s(dBm) - P_c(dBm) - 10 \log_{10} \left(\frac{RBW}{1Hz} \right) \quad (3.17)$$

where $L(\Delta f)_{dBc}$ is the phase noise, P_s is the power level of the noise in a band of 1Hz to a certain offset frequency from the carrier, P_c is the power level of carrier frequency and RBW is the bandwidth resolution of the spectrum analyzer.

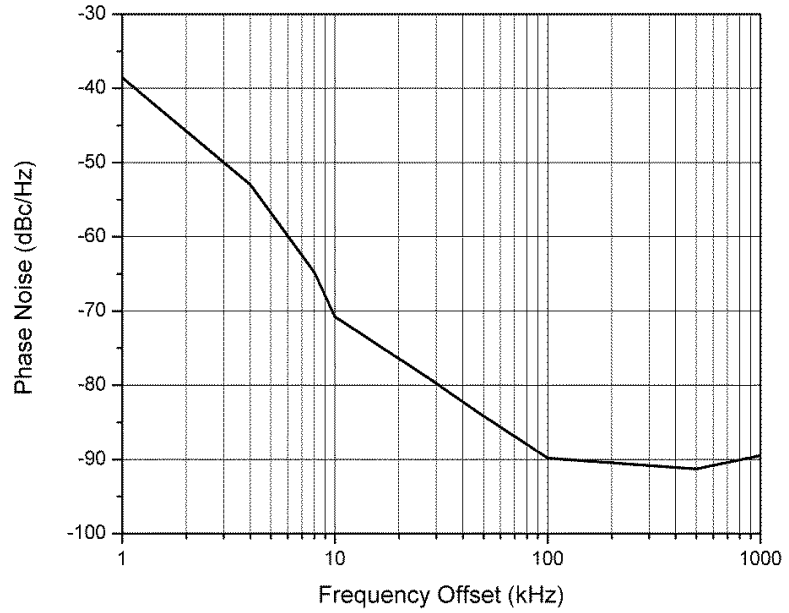


Fig. 3.41 Phase noise of the proposed transmitter

To characterize the performance of the LC oscillator, the widely used FOM [79], is adopted in this work. This parameter is calculated as:

$$FOM(f_0, P_{dc}) = L(\Delta f)_{dBc} - 20 \log_{10} \left(\frac{f_0}{\Delta f} \right) + 10 \log_{10} \left(\frac{P_{dc}}{1mW} \right) \quad (3.18)$$

where $L(\Delta f)_{dBc}$ represents the phase noise in dBc/Hz at an offset frequency Δf from the carrier frequency f_0 (in Hz), and P_{dc} is the DC power dissipation of the LC oscillator in mW. According to this definition the FOM for the proposed oscillator is -140dBc/Hz@1MHz. In Table 3.5 the LC oscillator performances are summarized.

Table 3.5: Performance summary of proposed LC Oscillator

	This work	[79]	[80]	[73]
Topology	LC cross-coupled Oscillator	LC voltage boosting VCO	Voltage-biased LC-VCO	Differential LC Oscillator
Process CMOS	0.35 μ m	0.18 μ m	0.18 μ m	0.25 μ m -epi
Power supply[V]	3.3	0.4	3	1.5
Current [mA]	20.8	1.5	3.2	4
Carrier Frequency[GHz]	2.54	3	1.49	1.8
Phase Noise [dBc/Hz]	-90@1MHz	-120@1MHz	-135	-121@600kHz
FOM [dBc/Hz]	-140@1MHz	-192@1MHz	-188	/

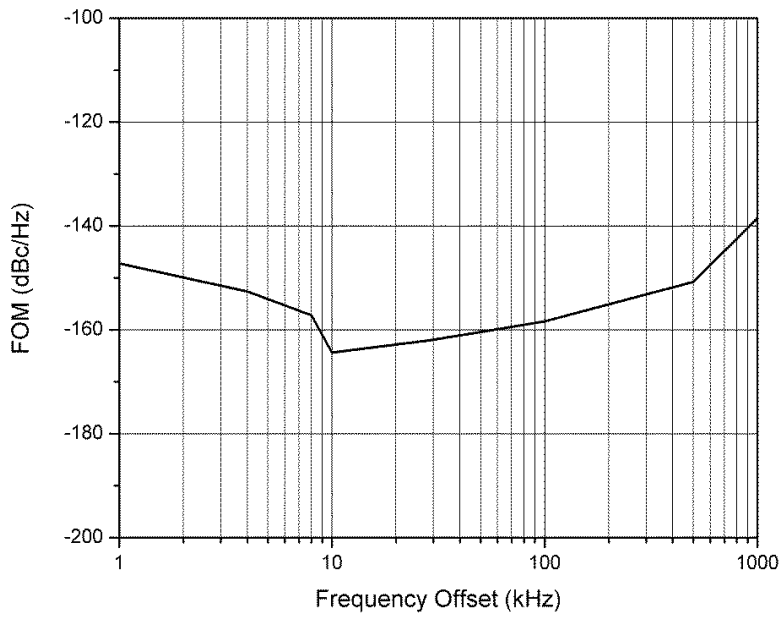


Fig. 3.42 Figure Of Merit of the proposed transmitter

3.7.4 Code Transmission Measurements

The capabilities of the discussed circuits to transmit an OOK modulated packet of data have been tested using a digital code, stored in the device, as the modulating signal. The feasibility of using the implemented system in conjunction with a commercial receiver has been proved employing a hand-held ICOM IC-R20 unit, a 0.15-3300 MHz receiver. Setting the IC-R20 on the AM mode, the demodulated signal has been detected at the audio output of the receiver and plotted on a oscilloscope. Fig. 3.43 shows the recorded digital data.

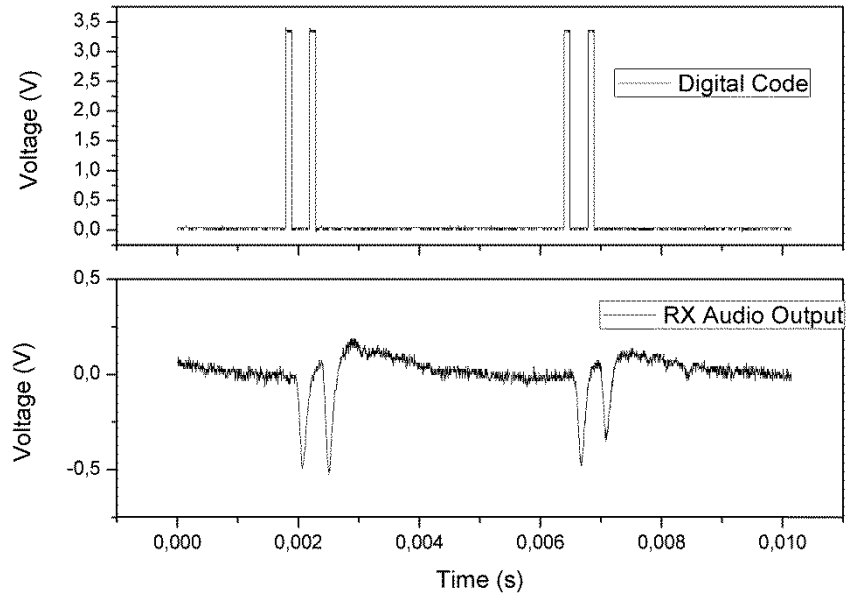


Fig. 3.43 Digital Code and demodulated signal as recorded at the audio output of the radio receiver.

3.7.5 Analysis of whole system

The functionality of the whole system has been tested, also in this case, employing a hand-held ICOM IC-R20 unit. The chip has been supplied with a voltage of 3.3V. An external Clock signal of 3kHz has been used to synchronize the digital section.

To distinguish the digital value a special 32-bit PISO has been implemented. The first and the last 8-bits are used to identify start and the stop of the modulation. In Fig. 3.44 is depicted the entire sequence of bits. Between the first and the last 8-bits, there are the serialized digital values of the light sensor and the PTAT (payload).

01010101 | PTAT Data | Light Sensor Data | 10101010

Fig. 3.44 Serialized output of 32-bit PISO

The chip has been tested with a temperature of 24°C and a irradiation level of 1125W/m². In agreement with the previous characterization of the sensors, the output voltage of the PTAT and light sensor are 0.763V and 1.971 V respectively.

The digital code and the recorded and demodulated signal at the audio output of the radio receiver are depicted in Fig. 3.45.

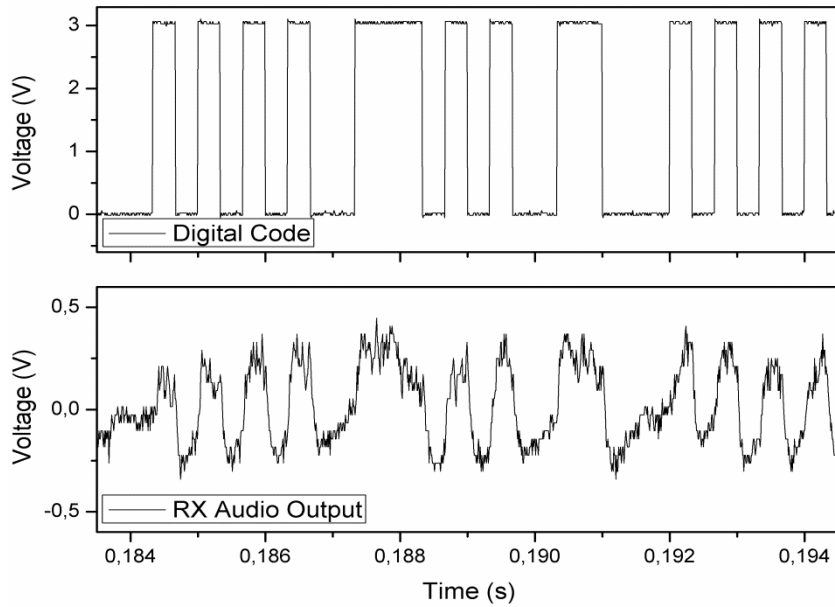


Fig. 3.45 Digital Code and demodulated signal of recorded at the audio output of the receiver. The data correspond at the light sensor and the PTAT

In Table 3.6 a comparison between expected values and experimental results with the associated error have been summarized.

Table 3.6 Summary between expected value and experimental results

Test Condition	Expected Digital Value	Real Digital Value	Analog Voltage	Digitalized Voltage	Conversion Error
24°C	00111011	00111010	0.763V	0.75V	0.6°C
1125W/m ²	10011001	10011000	1.971V	1.96V	7W/m ²

3.8 Remarks

In this chapter, a complete wireless sensor system to monitor HCPV modules with on-chip radiating element has been presented. The chip was realized using a standard 0.35 μm CMOS process.

The temperature sensor exhibits a wide range of linearity with temperature (room temperature to 100°C) by using a PTAT sensing element, with a sensitivity equal to 19.1 mV/°C after amplification stage.

The light sensor presents a sensitivity of 16.96 mV/°C in the range of interest (typical sunny day).

The digital data are transmitted by means of an RF transmitter with integrated dipole antenna, using OOK modulation.

The system radiates an electromagnetic field, provided by an LC cross-coupled oscillator, with oscillation frequency of 2.5 GHz approximately. The measured phase noise is about -90 dBc/1Hz@1MHz.

Conclusions

Conclusions

The aim of this PhD research project was to demonstrate the feasibility of wireless sensors obtained both with a platform implemented using off-the-shelf discrete components and with an all-in-one integrated solution that comprises analog sensors, transducer, an oscillator and the circuitry needed for transmitting the data.

In order to explore RFID applications beyond simple barcode replacement, this thesis argued the need for a reconfigurable, computation and sensor enhanced device, able to be wirelessly powered and interfaced with standard RFID technology. For this reason, a wireless sensors platform has been realized.

In this thesis, the implementation of the major functional blocks of the sensor platform have been described: RF harvester, dynamic impedance matching, digital section, microcontroller and RFID front end.

The tests carried out on the first, credit-card sized, platform showed an improvement in efficiency for RF input powers above -7dBm , with a maximum gain of $+12\%$ at -2dBm using a dynamic impedance matching strategy based on a switched capacitors routine governed by the MCU.

The firmware also performs a dynamic adjustment of the time intervals between two readings, allowing to control the average power budget of the system.

The platform has been used to perform temperature measurements over a 24-hour observation period in an indoor environment to demonstrate the feasibility of the platform in a typical application scenario.

Furthermore, the feasibility of using the sensor platform for long-run applications has been evaluated. Based on the sensor platform features, a

network model where one or multiple readers travel across the network to recharge the devices and gather their sensed data has been tested. The proposed solution based on the presented sensor platform has then been validated by comparing the results with those of state-of-art devices via both experimental and simulation results.

In addition, a 13.56MHz version of the platform has been realized, able to communicate with a standard reader at a maximum distance of 20cm.

In order to overcome the obstacles due to the use of discrete components and the related device dimensions, we moved later toward a compact, cheap and sufficiently accurate system designed as a single integrated circuit (IC).

As an application, a complete wireless sensor system designed to monitor High Concentration PhotoVoltaic modules, with an on-chip radiating element, has been designed and realized using a standard 0.35 μ m CMOS process.

In this solution, a PTAT cell (Proportional To Absolute Temperature) and a light sensor have been implemented as sensing elements, whereas a OOK (On-Off Keying) modulation circuitry allows to perform a very efficient wireless data transmission. The analog voltage provided by the PTAT cell is amplified in order to increase the signal dynamic prior the 8-bits Analog-to-Digital conversion (ADC). A transimpedance amplifier has been used in order to convert the current signal, generated by an integrated light sensor, into a voltage signal.

To pack the digital value before transmission, a special 32-bit PISO has been implemented. The first and the last 8-bits are used to identify start and the stop of the bit stream. Between the first and the last 8-bits, there are the serialized digital values of the light sensor and the PTAT (payload).

Each bit modulates a Radio Frequency (RF) carrier generated by a RF-oscillator. The oscillator can be seen as the RF block generating the carrier, which can be modulated by the data to be transmitted.

The temperature sensor exhibits a wide range of linearity with temperature (room temperature to 100°C) by using a PTAT sensing element, with a sensitivity equal to 19.1 mV/°C after amplification stage.

The light sensor shows a sensitivity of 16.96 mV/°C in the range of interest (typical sunny day).

The transmitter, equipped with an integrated dipole antenna emits an electromagnetic field with an oscillation frequency of 2.5 GHz approximately. The measured phase noise is about -90dBc/1Hz@1MHz.

Future works

Many aspects of the wireless sensor platform have been analyzed in this thesis. However, there are still some aspects that could be improved. For example, the platform could be deposited and assembled on metamaterial substrates with higher dielectric constant. Those materials allow to design more efficient antennas - or even smaller antennas with the same efficiency - if compared to the FR4 substrate used in this work, in order to harvest higher energy from the RF signal.

In addition, further sensors could be inserted to use the system in other applications.

Although in its present configuration the microchip requires an external power supply element (e.g. a micro battery), the implemented schemes might be considered as a building block for the future development of a fully integrated, energetically autonomous, devices.

For example, the Dickson rectifier topology, used in the sensor platform, could be implemented in an integrated version in order to realize an RF energy harvesting system on chip.

In addition, further CMOS compatible sensors could be integrated on the chip, e.g., a stress sensor that could monitor the possible deformation in HCPV modules.

Acknowledgements

I would like to thank Professor Giuseppe Francesco Della Corte, for his scientific guidance and support during these years. I am very grateful to Eng. Massimo Merenda, for his technical advice and collaboration in carrying out this work. I was very pleased to work with him. I thank Eng. Demetrio Iero and Giovanni Pangallo for their contributions to this project.

Finally, I am deeply thankful to my girlfriend Francesca and my family for their support and encouragement over these years.

Corrado Felini

References

- [1] IBM Corporation "An Introduction to Wireless Technology", no. October. 1995.
- [2] M. Vieira, C. Coelho, D. C. ; da Silva Junior, and J. da Mata, "Survey on Wireless Sensor Network Devices," in *Emerging Technologies and Factory Automation*, 2003. Proceedings. ETFA '03. IEEE Conference, 2003, pp. 537 – 544 vol.1.
- [3] L. Mateu, F. Moll, and U. Polit, "Review of Energy Harvesting Techniques and Applications for Microelectronics," in *Proc. SPIE 5837, VLSI Circuits and Systems II*, 2005.
- [4] S. K. Kamarudin, W. R. W. Daud, S. L. Ho, and U. a. Hasran, "Overview on the challenges and developments of micro-direct methanol fuel cells (DMFC)," *J. Power Sources*, vol. 163, no. 2, pp. 743–754, Jan. 2007.
- [5] J. R. Smith, K. P. Fishkin, B. Jiang, A. Mamishev, M. Philipose, A. D. Rea, S. Roy, and K. Sundara-rajana, "RFID-BASED TECHNIQUES FOR HUMAN-ACTIVITY DETECTION," *Commun. ACM*, vol. 48, no. 9, pp. 39–44, 2005.
- [6] A. Saeed, M. Faezipour, M. Nourani, S. Banerjee, G. Lee, G. Gupta, and L. Tamil, "A Scalable Wireless Body Area Network for Bio-Telemetry," *J. Inf. Process. Syst.*, vol. 5, no. 2, pp. 77–86, Jun. 2009.
- [7] H. Ramamurthy, B. S. Prabhu, and R. Gadh, "Wireless Industrial Monitoring and Control using a Smart Sensor Platform," *Sensors Journal*, IEEE, 2007.
- [8] L. R. Garcia, L. Lunadei, P. Barreiro, and J. I. Robla, "A review of wireless sensor technologies and applications in agriculture and food industry: state of the art and current trends," *Sensors (Basel)*, vol. 9, no. 6, pp. 4728–50, Jan. 2009.
- [9] E. Abad, F. Palacio, M. Nuin, a. G. De Zárate, a. Juarros, J. M. Gómez, and S. Marco, "RFID smart tag for traceability and cold chain monitoring of foods: Demonstration in an intercontinental fresh fish logistic chain," *J. Food Eng.*, vol. 93, no. 4, pp. 394–399, Aug. 2009.
- [10] N. Cho, S. Song, S. Kim, S. Kim, and H. Yoo, "A 5.1- μ W UHF RFID Tag Chip integrated with Sensors for Wireless Environmental Monitoring," in *Solid-State Circuits Conference*, 2005. ESSCIRC 2005. Proceedings of the 31st European, 2005, pp. 279–282.
- [11] X. Jiang, J. Polastre, and D. Culler, "Perpetual environmentally powered sensor networks," *IPSN 2005. Fourth Int. Symp. Inf. Process. Sens. Networks.*, pp. 463–468, 2005.
- [12] M. Mi, M. H. Mickle, C. Capelli, and H. Swift, "RF Energy Harvesting with Multiple Antennas in the Same Space," *Antennas Propag. Mag. IEEE*, vol. 47, no. 5, pp. 100–106, 2005.
- [13] J. Lester Hill, "System Architecture for Wireless Sensor Networks", PhD Thesis, Spring 2003.
- [14] M. Danesh, S. Member, and J. R. Long, "Photovoltaic Antennas for Autonomous Wireless Systems," *IEEE Trans. CIRCUITS Syst. EXPRESS BRIEFS*, vol. 58, no. 12, pp. 807–811, 2011.
- [15] V. Leonov, "Thermoelectric Energy Harvesting of Human Body Heat for Wearable Sensors," *IEEE Sens. J.*, vol. 13, no. 6, pp. 2284–2291, Jun. 2013.
- [16] H. Xiao and X. Wang, "A Review of Piezoelectric Vibration Energy Harvesting Techniques," *Int. Rev. Mech. Eng.*, vol. 8, no. 3, pp. 609–620, 2014.
- [17] S. Roundy, P. K. Wright, and J. Rabaey, "A study of low level vibrations as a power source for wireless sensor nodes," *Comput. Commun.*, vol. 26, no. 11, pp. 1131–1144, Jul. 2003.
- [18] M. Piñuela, S. Member, P. D. Mitcheson, and S. Member, "Ambient RF Energy Harvesting in Urban and Semi-Urban Environments," *IEEE Trans. Microw. Theory Tech.*, vol. 61, no. 7, pp. 2715–2726, 2013.

- [19] B. K. Niotaki, A. Collado, A. Georgiadis, S. Kim, and M. M. Tentzeris, "Solar / Electromagnetic Energy Harvesting and Wireless Power Transmission," *Proc. IEEE*, vol. 102, no. 11, pp. 1712–1722, 2014.
- [20] R. Shigeta, T. Sasaki, D. M. Quan, Y. Kawahara, R. Vyas, M. Tentzeris, and T. Asami, "Ambient-RF-energy-harvesting sensor node with capacitor-leakage-aware duty cycle control," *Proc. IEEE Sensors*, pp. 1–4, 2012.
- [21] ITU-R Radio Regulations, Volume 1, [Online]. Available: <http://www.itu.int>.
- [22] M. Merenda, C. Felini, and F. G. Della Corte, "Battery-less smart RFID tag with sensor capabilities," 2012 IEEE Int. Conf. RFID-Technologies Appl., pp. 160–164, Nov. 2012.
- [23] D. De Donno, L. Catarinucci, and L. Tarricone, "An UHF RFID Energy-Harvesting System Enhanced by a DC-DC Charge Pump in Silicon-on-Insulator Technology," *IEEE Microw. Wirel. Components Lett.*, vol. 23, no. 6, pp. 315–317, Jun. 2013.
- [24] D. De Donno, L. Catarinucci, and L. Tarricone, "RAMSES: RFID Augmented Module for Smart Environmental Sensing," *IEEE Trans. Instrum. Meas.*, pp. 1–1, 2014.
- [25] A. P. Sample, S. Member, D. J. Yeager, P. S. Powladge, A. V. Mamishev, S. Member, and J. R. Smith, "Design of an RFID-Based Battery-Free Programmable Sensing Platform," *Instrum. Meas. IEEE Trans. RFID Virtual Journal*, IEEE, vol. 57, no. 11, pp. 2608–2615, 2008.
- [26] J. R. Smith, B. Jiang, S. Roy, and M. Philipose, "ID Modulation: Embedding Sensor Data in an RFID Timeseries," *Inf. Hiding, LNCS*, vol. 3727, pp. 234–246, 2005.
- [27] L. Catarinucci, R. Colella, and L. Tarricone, "A Cost-Effective UHF RFID Tag for Transmission of Generic Sensor Data in Wireless Sensor Networks," *IEEE Trans. Microw. Theory Tech.*, vol. 57, no. 5, pp. 1291–1296, May 2009.
- [28] R. Vyas, S. Member, V. Lakafosis, H. Lee, G. Shaker, L. Yang, G. Orecchini, A. Traille, M. M. Tentzeris, L. Roselli, and S. Member, "Inkjet Printed, Self Powered, Wireless Sensors for Environmental, Gas, and Authentication-Based Sensing," *IEEE Sens. J.*, vol. 11, no. 12, pp. 3139–3152, 2011.
- [29] J. Virtanen, S. Member, L. Ukkonen, T. Björninen, A. Z. Elsherbeni, and L. Sydänheimo, "Inkjet-Printed Humidity Sensor for Passive UHF RFID Systems," *IEEE Trans. Instrum. Meas.*, vol. 60, no. 8, pp. 2768–2777, 2011.
- [30] T. Ussmueller, D. Brenk, J. Essel, J. Heidrich, G. Fischer, and R. Weigel, "A multistandard HF/ UHF-RFID-tag with integrated sensor interface and localization capability," 2012 IEEE Int. Conf. RFID, pp. 66–73, Apr. 2012.
- [31] C. Occhiuzzi, C. Paggi, and G. Marrocco, "Passive RFID Strain-Sensor Based on Meander-Line Antennas," *IEEE Trans. Antennas Propag.*, vol. 59, no. 12, pp. 4836–4840, Dec. 2011.
- [32] H. Nakamoto, D. Yamazaki, T. Yamamoto, H. Kurata, S. Yamada, and K. Mukaida, "A Passive UHF RF Identification CMOS Tag IC," *IEEE J. Solid-State Circuits*, vol. 42, no. 1, pp. 101–110, 2007.
- [33] UHF RFID Gen2 SL900A Sensory Tag IC [Online]. Available: <http://www.ams.com>.
- [34] EasyToLog RFID Tag [Online]. Available: <http://www.caenrfid.it>.
- [35] SensTAG RFID Tag [Online]. Available: <http://www.phaseiv-engr.com>.
- [36] C. Felini, M. Merenda, and F. G. Della Corte, "Dynamic impedance matching network for RF energy harvesting systems," in *RFID Technology and Applications Conference (RFID-TA)*, 2014 IEEE, 2014, pp. 86 – 90.
- [37] William C. Brown, "The history of wireless power transmission," *Solar Energy*, vol. 56, no. 1, pp. 3–21, 1996.
- [38] C. A. Balanis, "Antenna theory: a review," *Proc. IEEE*, vol. 80, no. 1, pp. 7–23, 1992.
- [39] C. A. Balanis, "Antenna theory analysis and design third edition" Wiley, 2005.
- [40] J. F. Dickson, "Circuits Using an Improved Voltage," no. 3, pp. 374–378, 1976.
- [41] O. Kazanc and C. Dehollain, "Impedance-Matched Sensor-Tag Antenna Design Using Genetic Algorithm Optimization," *Medical Information & Communication Technology (ISMICT)*, 2011 5th International Symposium on, pp 61-64, March 2011.

References

- [42] G. Marrocco, "The Art of UHF RFID Antenna Design: Impedance-Matching and Size-Reduction Techniques," *Antennas Propag. Mag. IEEE RFID Virtual Journal*, IEEE, vol. 50, no. 1, pp. 66–79, 2008.
- [43] S. He, J. Chen, F. Jiang, D. K. Y. Yau, G. Xing, and Y. Sun, "Energy provisioning in wireless rechargeable sensor networks," 2011 Proc. IEEE INFOCOM, pp. 2006–2014, Apr. 2011.
- [44] Meader antenna Texas Instruments [Online]. Available: <http://www.ti.com>.
- [45] Mitsubishi antenna [Online]. Available: <http://www.mitsubishi.com>.
- [46] Impinj Speedway Revolution RFID Readers [Online]. Available: <http://www.impinj.com>.
- [47] Power Detector LT5505 [Online]. Available: <http://www.linear.com>.
- [48] Avago Hsms282 Schottky Diodes [Online]. Available: <http://www.avagotech.com>.
- [49] Avago Hsms285 Schottky Diodes [Online]. Available: <http://www.avagotech.com>.
- [50] P. Nintanavongsa, S. Member, U. Muncuk, D. R. Lewis, and K. R. Chowdhury, "Design Optimization and Implementation for RF Energy Harvesting Circuits," *IEEE Emerg. Sel. Top. Circuits Syst. IEEE J. RFID Virtual J.*, vol. 2, no. 1, pp. 24–33, 2012.
- [51] LDO Regulator LT3007 [Online]. Available: <http://www.linear.com>.
- [52] PIC16LF1503 Microchip Technology [Online]. Available: <http://www.microchip.com>.
- [53] RFID Tag EM4325 EM Microelectronics [Online]. Available: <http://www.emmicroelectronic.com>.
- [54] Temperature Sensor Serverflu Magiant [Online]. Available: <http://www.magiant.it>.
- [55] J. Grefenstette, R. Gopal, B. Rosmaita, D. Van Gucht "Genetic algorithms for the traveling salesman problem," in *International Conference on Genetic Algorithms and their Applications*, 1985.
- [56] NFC/RFID tag M24LR64-R [Online]. Available: <http://www.st.com>.
- [57] N. Forero, J. Hernández, and G. Gordillo, "Development of a monitoring system for a PV solar plant," *Energy Convers. Manag.*, vol. 47, pp. 2329–2336, 2006.
- [58] A. Chouder, S. Silvestre, B. Taghezouit, and E. Karatepe, "Monitoring, modelling and simulation of PV systems using LabVIEW," *Sol. Energy*, vol. 91, pp. 337–349, 2013.
- [59] M. Benghanem, "A low cost wireless data acquisition system for weather station monitoring," *Renew. Energy*, vol. 35, no. 4, pp. 862–872, 2010.
- [60] M. Gargiulo, P. Guerriero, S. Daliento, a. Irace, V. d'Alessandro, M. Crisci, a. Smarrelli, and M. Smarrelli, "A novel wireless self-powered microcontroller-based monitoring circuit for photovoltaic panels in grid-connected systems," *SPEEDAM 2010 - Int. Symp. Power Electron. Electr. Drives, Autom. Motion*, pp. 164–168, 2010.
- [61] A. Bakker, J. H. Huijsing, and S. Member, "Micropower CMOS Temperature Sensor with Digital Output," *IEEE J. Solid-State Circuits*, vol. 31, no. 7, pp. 933–937, 1996.
- [62] G. C. M. Meijer, G. Wang, and F. Fruett, "Temperature Sensors and Voltage References Implemented in CMOS Technology," *IEEE Sens. J.*, vol. 1, no. 3, pp. 225–234, 2001.
- [63] M. A. P. Pertijs, G. C. M. Meijer, and J. H. Huijsing, "Precision Temperature Measurement Using CMOS Substrate PNP Transistors," *IEEE Sens. J.*, vol. 4, no. 3, pp. 294–300, 2004.
- [64] E. R. Fossum, "CMOS image sensors: electronic camera-on-a-chip," *IEEE Trans. Electron Devices*, vol. 44, no. 3, pp. 1689–1698, 1997.
- [65] W. Huang, Y. Liu, and Y. Hsin, "A high speed and high responsivity photodiode in standard CMOS technology," *IEEE Photonics Technology Letters* pp. 197–199, 2007.
- [66] B. Razavi, "Design of Analog CMOS Integrated Circuits", McGraw Hill, 2001.
- [67] W.-J. Liu and O. T.-C. ; L.-K. D. ; P.-K. W. ; K.-H. H. ; F.-W. J. Chen, "A CMOS Photodiode Model," in *Workshop on Behavioral Modeling and Simulation*, 2001. *BMAS 2001. Proceedings of the Fifth IEEE International*, 2001, pp. 102–105.
- [68] Austria Microsystems, 0.35 μm CMOS Process Parameters, Datasheet [Online]. Available: <http://www.ams.com>.
- [69] BBIAS, Austria Microsystems, 0.35 μm CMOS, Datasheet [Online]. Available: <http://www.ams.com>.
- [70] AMP_OP, Austria Microsystems, 0.35 μm CMOS, Datasheet , [Online]. Available: <http://www.ams.com>.
- [71] ADC8, Austria Microsystems, 0.35 μm CMOS, Datasheet , [Online]. Available: <http://www.ams.com>.

- [72] J. P. Silver, LC oscillator Tutorial - RF, RFIC & Microwave Theory, Design.
- [73] A. Hajimiri and T. H. Lee, "Design issues in CMOS differential LC oscillators," *IEEE J. Solid-State Circuits*, vol. 34, no. 5, pp. 717–724, May 1999.
- [74] J. Craninckx, S. Member, M. S. J. Steyaert, and S. Member, "A 1.8-GHz Low-Phase-Noise CMOS VCO Using Optimized Hollow Spiral Inductors," vol. 32, no. 5, pp. 736–744, 1997.
- [75] G. Haobijam and R. Paily, "Quality factor enhancement of CMOS inductor with pyramidal winding of metal turns," *Proc. 14th Int. Work. Phys. Semicond. Devices, IWPSD*, pp. 729–732, 2007.
- [76] D. Barras, F. Ellinger, H. Jäckel, and W. Hirt, "Low-power ultra-wideband wavelets generator with fast start-up circuit," *IEEE Trans. Microw. Theory Tech.*, vol. 54, no. 5, pp. 2138–2145, 2006.
- [77] V. Karam, P. H. R. Popplewell, A. Shamitn, J. Rogers, and C. Plett, "A 6.3 GHz BFSK transmitter with on-chip antenna for self-powered medical sensor applications," *Dig. Pap. - IEEE Radio Freq. Integr. Circuits Symp.*, pp. 101–104, 2007.
- [78] K. O. Kenneth, K. Kim, B. a. Floyd, J. L. Mehta, H. Yoon, C. M. Hung, D. Bravo, T. O. Dickson, X. Guo, R. Li, N. Trichy, J. Caserta, W. R. Bomstad, J. Branch, D. J. Yang, J. Bohorquez, E. Seok, L. Gao, A. Sugavanam, J. J. Lin, J. Chen, and J. E. Brewer, "On-chip antennas in silicon ICs and their application," *IEEE Trans. Electron Devices*, vol. 52, no. 7, pp. 1312–1323, 2005.
- [79] F. Yu, "A Low-Voltage and Low-Power 3-GHz CMOS LC VCO for S-Band Wireless Applications," *Wirel. Pers. Commun.*, vol. 78, no. 2, pp. 905–914, May 2014.
- [80] H. X. Wang, W. Zhang, Yanyan Y. Liu, and L. Zhang, "A LOW PHASE NOISE LC-VCO FOR PHASE-LOCKED FREQUENCY SYNTHESIZERS," *Microw. Opt. Technol. Lett.*, vol. 56, no. 6, pp. 1486–1492, 2014.